Creation of Peptide-based Oligomers and Tailored Surfaces as Piezoelectric Biomaterials

by

Haley Marie Grimm

B.S. Chemistry, Denison University, 2014

Submitted to the Graduate Faculty of

the Kenneth P. Dietrich School of Arts and Sciences in partial fulfillment

of the requirements for the degree of

Doctor of Philosophy

University of Pittsburgh

2019

UNIVERSITY OF PITTSBURGH

DIETRICH SCHOOL OF ARTS AND SCIENCES

This dissertation was presented

by

Haley Marie Grimm

It was defended on

September 26, 2019

and approved by

Geoffrey Hutchison, Associate Professor, Department of Chemistry

Paul Floreancig, Professor, Department of Chemistry

Nurit Ashkenasy, Professor, Department of Materials Engineering, Ben-Gurion University of the Negev

Thesis Advisor: W. Seth Horne, Associate Professor, Department of Chemistry

Creation of Peptide-based Oligomers and Tailored Surfaces as Piezoelectric Biomaterials

Haley Marie Grimm, PhD

University of Pittsburgh, 2019

Peptides and proteins are advantageous as biomaterials due to their biocompatibility and flexible nature. A growing understanding of sequence/structure relationships and the conception of unnatural foldamers, scaffolds that can mimic folds similar to those found in nature, has opened doors to new architectures and materials properties. These scaffolds have shown promise as biosensors and bioelectronics. Hindering such work, however, is the fact that the surface environment can have profound effects on the predictability of folding behavior. This can result in a loss of stability or activity when a sequence of interest is tethered to an inorganic substrate. This dissertation details my work towards understanding how biomolecule folding is affected by surface properties and how molecular and surface properties combine to affect the inherent electromechanical nature of peptides and foldamers.

Chapter 2 explores the molecular origins of the piezoelectric response (the mechanical deformation arising from an electrical input) of peptide and peptoid self-assembled monolayers (SAMs). A series of designed molecules, where side chain and backbone composition was varied to alter the folding propensity, was used to test the hypothesis that backbone conformation influences electromechanical response. The piezo response of polar monolayers arising from the self-assembly of these molecules on a substrate was quantified by piezoelectric force microscopy. I conclude that backbone rigidity is an important determinant in peptide electromechanical response.

Chapter 3 aims to expand our understanding of the influence surface attachment has on peptide and protein conformation. A series of synthetic peptides were incorporated onto tailored-composition alkanethiol SAMs on gold surfaces via copper-catalyzed azide alkyne cycloaddition. The resulting surfaces were examined via polarization modulated infrared reflection absorption spectroscopy (PM-IRRAS) to assess peptide conformational preferences in response to changing surface properties. While surface density and polarity did not significantly alter peptide conformation for these systems, a more complex system, the bacterial alkaline phosphatase (BAP) enzyme, was affected. Upon incorporation onto our synthetic surfaces, the enzymatic activity of BAP was influenced by the surface context, showing a sharp decrease in activity when attached to a hydrophobic substrate.

Table of Contents

vii

List of Tables

List of Figures

Preface

I didn't plan on a career in science, going to graduate school, or getting a PhD from a young age. A sixteen-year old version of myself would have claimed she wanted to be dancer, performing with a big company on big stages. Though I'd always loved going to school and learning new things, I'd never considered pursuing science until I encountered some great teachers in high school and college who encouraged me to explore this interest. I have many people to thank that have helped me throughout my academic journey and personal growth.

First, I'd like to thank my graduate advisor, W. Seth Horne. His guidance, direction, and support over the last five years has been invaluable. Working with Seth has taught me to truly "think like a scientist." He holds all of his students' work to a high standard and has pushed my critical thinking to new levels. Although I may never understand how one person can possess so much knowledge about so many different topics, I hope at least a small piece of that has rubbed off on me. I would also like to thank my committee members; Geoffrey Hutchison for his outstanding guidance and support during my collaborative project with his lab, Paul Floreancig for his continued interest in my research as well as PLU endeavors, and Nurit Ashkenasy for her helpful conversations during her visits to Pittsburgh and agreeing to be on my committee even if it wasn't convenient. Other teachers and advisors I'd like to thank are Joseph Reczek who gave me my first research experience in his lab as an undergraduate and encouraged me to pursue a PhD and Bill Smith who taught my senior AP Chemistry class and first noticed my aptitude for the subject.

It's been wonderful to share my time in graduate school with co-workers, friends, and talented scientists, Shilpa Rao, Jackie Santhouse, Chino Cabalteja, and Shelby Schettler. Whether

we are discussing confounding data, ruminating on how to fix a broken instrument, or going to grab coffee, growing as scientists and people with this group has been a blast. A few past lab members I'd like to thank also come to mind: Kaylyn Oshaben, for teaching me peptide synthesis and providing tips on surviving graduate school during my first semester, and Kelly George, for her friendship and leaving me "to-do lists" that pushed me to network and meet others in the Pittsburgh science community.

On the personal side, I also have many people to acknowledge. First and foremost, my parents, Bruce and Janice Grimm, who have provided endless love and support since the beginning. I've been very fortunate to have them just 30 minutes down the road which meant going home quite often for home-cooked food and lots of leftovers, attending Steelers' games with Dad on crisp fall days (or sometimes below-freezing winter days!), and having loving hugs available whenever the stresses of graduate school or life began to build up. My parents have always been champions of education for my sister and I. They attended every single school and extra-curricular event we took part in (which was A LOT! of events) and saved up tirelessly so we could attend a good college. I will never forget how happy my Mom was the day of my college graduation as she told me pridefully through tears "an education and the knowledge you've gained with it is something no one can ever take away from you. I'm so proud of you."

My younger sister, Heather Grimm, is now pursuing her own PhD and having that in common over the last year has been wonderful. I hope to provide her with the support she needs over the coming years just as she has for me. My best friends, Miaja Stitcher, Liesje Steenkiste, and Monica Edgerton, always remind me they are just a "phone call or quick airplane ride" away. I'm thankful for their humor and positivity every day.

Lastly, I want to give a special thanks to Soumitra Mokashi Punekar. Words can't really describe the impact he has had on my life, so instead I'll thank him for a few tangible things. I want to thank him for his patience and insights when looking at a scribbled drawing for a possible figure or listening to my concerns about a frustrating experiment. I also want to thank him for introducing me to Maple Cat (the cutest stress relief on the planet), many delicious new Indian food recipes, and Quentin Tarantino movies (even if I continuously complain that they are too violent). I love you and I'm excited for our future in Chicago!

1.0 Introduction

Peptides and proteins have become increasingly important players in the field of materials and surface science. Biomacromolecules are often touted for advantages over inorganic counterparts such as biocompatibility, biodegradability, and flexibility. These advantages translate to potential uses of biomaterials in implantable and wearable devices, biomedicine, bioelectronics, and biosensing. The macroscopic materials properties of natural peptides and proteins have been studied for decades, beginning with collagen and spider silk.[1] Since then, design efforts, informed by an increasingly sophisticated understanding of sequence/structure relationships, have led to materials with unprecedented properties, such as reversible adhesives[2], self-assembling nanoparticles[3], and stimuli responsive hydrogels.[4]

Peptides and proteins are attractive for their capacity to self-assemble and vast potential sequence space; the structural diversity possible in peptides and related oligomers has been expanded greatly through advances in solid phase synthesis and heterologous expression with non-canonical amino acids.[5-6] Thus, peptides and proteins can be readily modified by the introduction of a wide variety of amide bond forming monomers, expanding upon the twenty canonical amino acids. Such efforts are complemented by an expanding toolbox of chemoselective reactions capable of site-specifically functionalizing side chains or termini.[7] Finally, peptides are also attractive in materials contexts because of the high polarity of the peptide bond (3.6 D per residue). When a helical conformation is adopted, these dipoles align, creating a macrodipole favoring directional electron transfer.[8-9]

Peptides, proteins, and their synthetically modified derivatives have been explored as materials through a variety of lenses. Taking advantage of known sequence/structure relationships,

'smart materials,' which are reversibly responsive to environmental conditions, have been developed by creating highly-designed supramolecular assemblies.[1] Photo-responsive materials are one example that has gained traction due to the non-invasive nature of optical triggers and the high degree of spatial and temporal control.[10] Biosensors and drug-delivery vehicles are just a few examples of practical applications these materials have found thus far.[10] Taking cues from nature, protein-based biomaterial research has also bridged into the field of data and information storage.[11] Biomaterial-based memory has been developed by utilizing electron transfer mechanisms perfected through evolution.[11] On the small peptide front, sequences with antimicrobial properties have been explored as antifouling and antimicrobial coatings. Antimicrobial peptides have been shown to prevent the formation of biofilms, a shared concern across fields such as medical devices, food processing, and water filtration.[12-17] Coatings of these peptides can kill pathogens adhered to a surface through outer membrane disruption.[15]

Coiled-coil peptides are a compelling example of how a comprehensive understanding of peptide design principles can translate to the creation of modular and tailored assemblies. The rules governing the folding, oligomerization states, and arrangement of coiled-coil peptides, a common folding motif found in nature, have been studied extensively. Coiled-coils are defined as two or more α-helical peptides that self-assemble, typically, in a left-handed twisted superstructure through the tight packing of hydrophobic side chains along the interacting face. These structures have a heptad sequence repeat unit denoted as (***abcdefg***)$_n$, where ***n*** is the number of repeat units (**Figure 1A**). Residues at the ***a*** and ***d*** heptad positions, located in the interfacial region, are typically hydrophobic. The ***e*** and ***g*** positions are typically polar, charged amino acids which can create stabilizing electrostatic interactions if complementary charged pairs are placed on a neighboring helix in the bundle. The exact residue chosen for each of these positions in the heptad specify the

size of the helical bundle, or oligomerization state, as well as topology (parallel versus antiparallel helical arrangements) and thermodynamic stability.
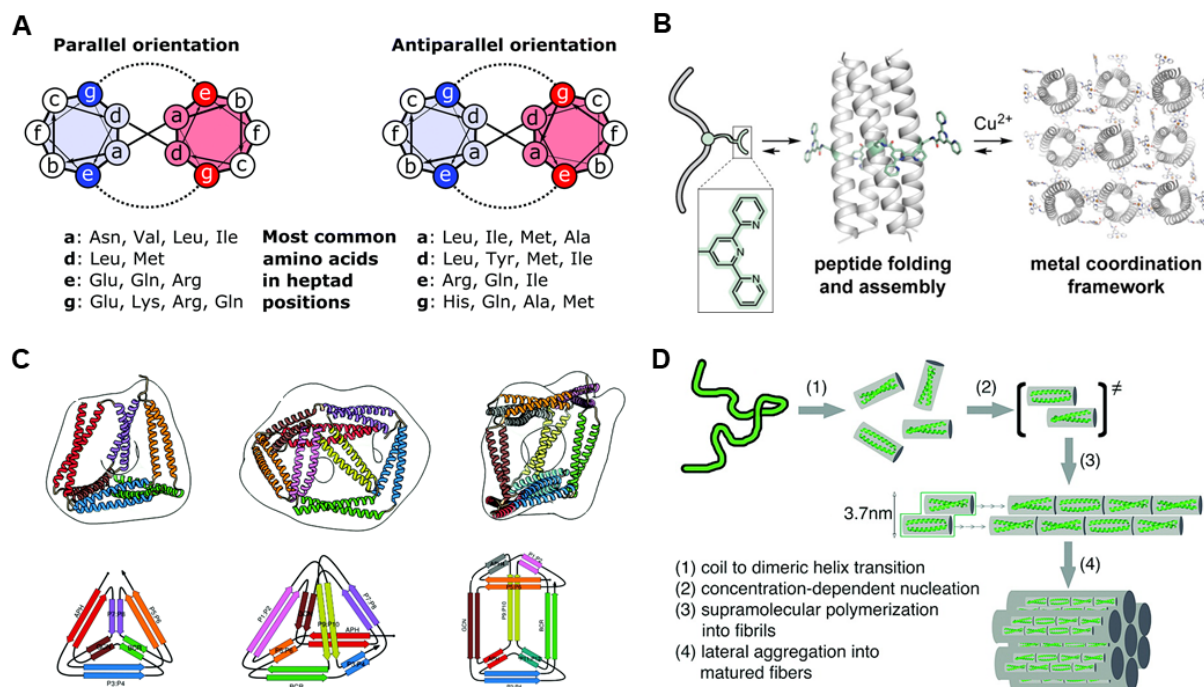
Figure 1. Overview of coiled-coil structures highlighting how the manipulation of sequence affects the structures that can be formed. (A) Helical wheel representation for two possible coiled-coil orientations and the most common residues at each position. Image adapted with permission from ref. 18. Copyright 2018 Royal Society of Chemistry. (B) Metal-coordinated polymers, nets, and frameworks based on a coiled-coil structure. Image adapted with permission from ref. 19. Copyright 2017 American Chemical Society. (C) Coiled-coil origami, 3D structures obtained from SAXS analysis (top) and the representative design schemes for each (bottom). Image adapted with permission from ref. 18. Copyright 2018 Royal Society of Chemistry. (D) Scheme for the self-assembly of coiled-coil dimers into nanofiber materials. Image adapted with permission from ref. 20. Copyright 2008 American Chemical Society.

One of the first biomaterials based on coiled-coils was reported by the Woolfson lab; their designed peptide fibers assembled through "sticky ends" incorporated through *e* and *g* heptad positions occupied by oppositely charged residues at the N and C-termini.[21] This work opened the door for new materials such as pH responsive coiled-coil nanofibers[20], nanotubes[22], or even more

complex, 3D structures such as self-assembling cages[23] and metal-coordinated nets and frameworks (**Figure 1**).[19] The designable platform that coiled-coils provide has allowed the field of protein-based origami (CCPOs) to flourish; currently, 3D cages in a variety of geometric shapes, such as tetrahedrons, square pyramids and triangular prisms, with a range of cavity sizes have been designed and realized.[18] These coiled-coil biomaterials show promise for drug delivery systems and many biological applications.[24]

The utilization of sequence/structure relationships for the creation of materials extends far beyond naturally occurring building blocks; bio-inspired "foldamer" scaffolds have also been investigated as biomaterial components. The term "foldamer," coined by Gellman, refers to polymers that fold into specific compact conformations, which are often used in the study and mimicry of biopolymers such as proteins.[25] In the biomaterials realm, foldamers have many similar advantages to peptides and proteins, however, foldamers also have the capability to form structures or achieve functions different from those found in nature (**Figure 2**). For instance, anion recognition sensors using halogen and hydrogen bonding foldamers were developed through self-assembly on gold electrodes.[26] 2D molecular patterning has been achieved on surfaces by alternating oligoamide turn inducers and long alkane spacers.[27] Modifications to solid surface electronic properties were induced by small alterations to the backbone composition of non-canonical dipeptides.[28] Finally, foldamers based on amphiphilic oligo(*meta*-phenylene ethynylene) exhibit reversible, light-induced helix-coil transitions and show promise as delivery vehicles or dynamic receptors.[29]
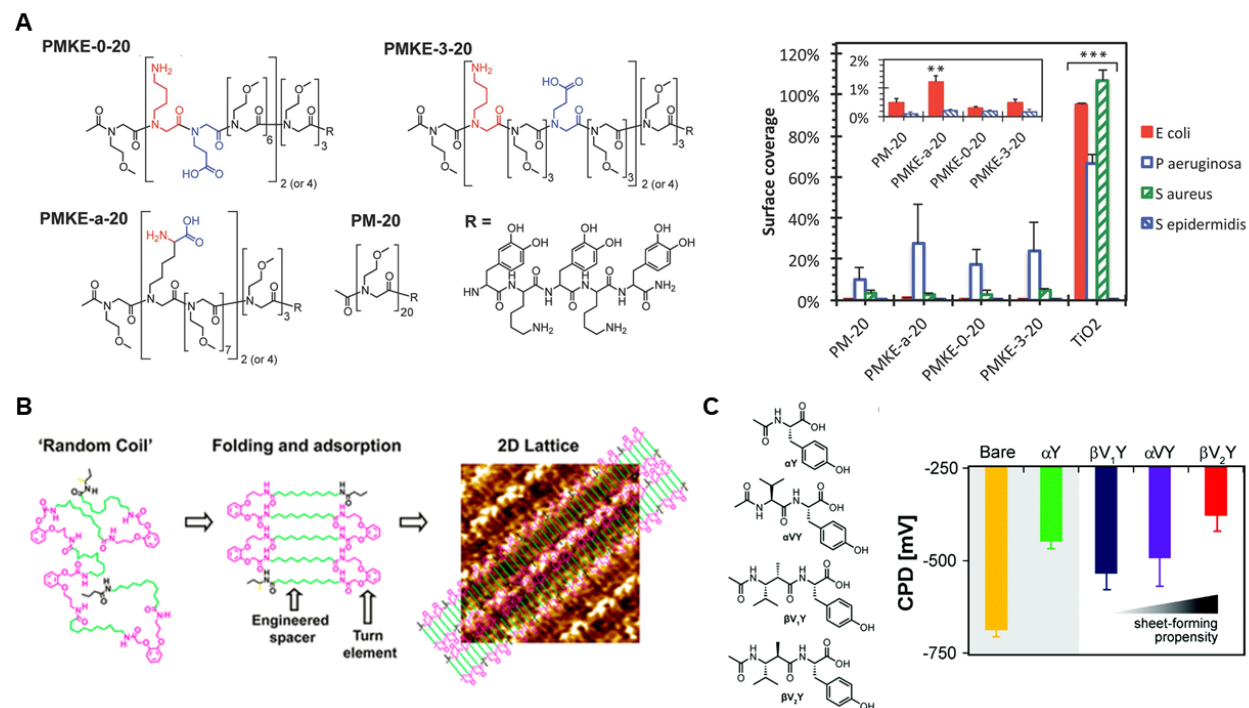
Figure 2. Examples of foldamer-based materials. (A) Peptoid-based antifouling polymer brushes that prevent cell attachment to biointerfaces. Image adapted with permission from ref. 30. Copyright 2015 American Chemical Society. (B) 2D lattices formed from alternating turn elements and alkane spacers. Image adapted with permission from ref. 27. Copyright 2012 American Chemical Society. (C) Semiconducting solid surfaces functionalized with non-canonical dipeptides resulted in changes to surface electronic properties. Image adapted with permission from ref. 28. Copyright 2017 Royal Society of Chemistry.

One particular class of peptidomimetic polymers, known as peptoids, have gained popularity as supra- and macromolecular biomaterials due to their modular synthetic route and tailored folding capabilities.[31] Peptoids differ from peptides in the placement of their side chains, which are attached to the amide nitrogen rather than the C_α resulting in a tertiary amide backbone and the elimination of backbone hydrogen-bonding (**Figure 3A**). Synthesis of peptoids is achieved via a solid phase submonomer approach first introduced by Zuckerman and later translated into a modern microwave solid phase synthesis protocol by Blackwell (**Figure 3B**).[32,33] This approach involves coupling bromoacetic acid onto a polymer resin and subsequent S_N2-type displacement

of the halide with the desired primary amine, many of which are commercially available.[34] The Zuckerman group has created an assortment of peptoid architectures including water-soluble nanosheets[35] and monodisperse superhelices (**Figure 3**).[36] Peptoid polymers have been studied in a variety of contexts including controlling the nucleation and growth of inorganic crystals,[37] studying electron transfer through incorporation of porphyrins to a peptoid helix,[38] mimicry of materials such as collagen[39] and poly(ethyleneoxide) ((PEO)-based) mattertials,[40] and creation of 1D metal-organic frameworks.[41] Zwitterionic peptoid polymers have also been explored as antifouling polymer brushes to prevent non-specific protein adsorption and cell attachment to biointerfaces.[30]
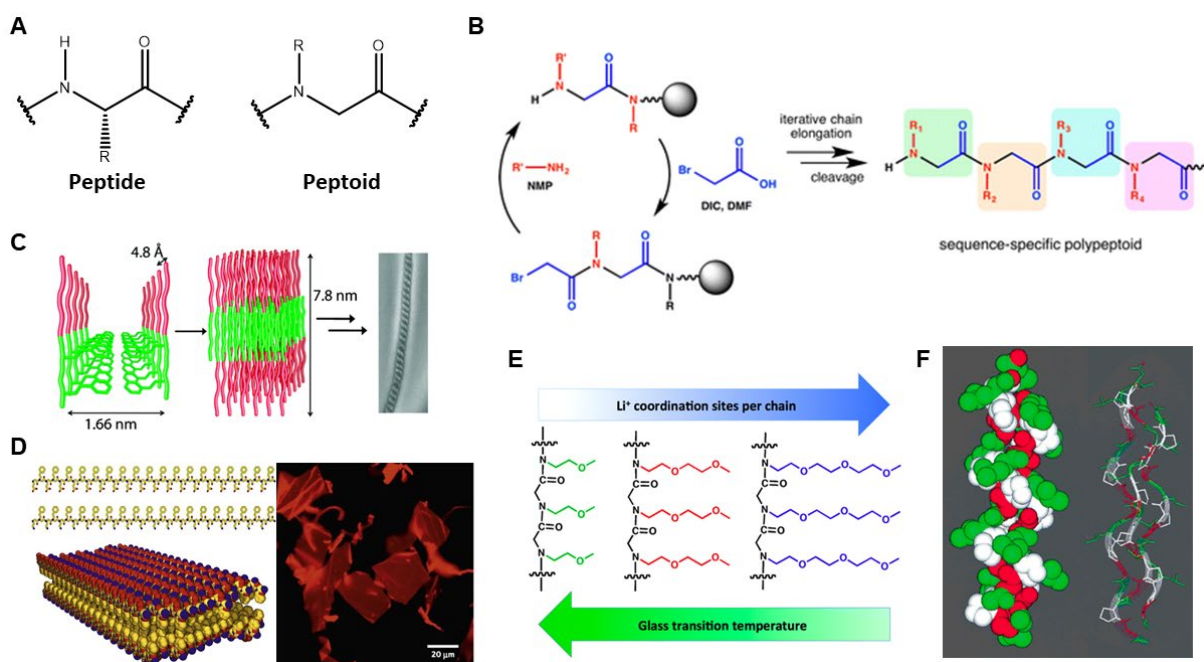
Figure 3. The structure, synthesis, and some materials developed with peptoid foldamers. (A) Comparison of peptide and peptoid backbone structure. (B) Submonomer synthesis approach commonly used to build peptoid oligomers. Image adapted with permission from ref. 31. Copyright 2013 American Chemical Society. (C) Superhelices formed from peptoid amphilies. Image adapted with permission from ref. 36. Copyright 2010 American Chemical Society. (D) Free-floating ultrathin 2D nano-sheets formed from peptoid amphiphiles through aromatic interactions and electrostatic recognition. Image adapted with permission from ref. 35. Copyright 2010

Nature Publishing Group. (E) PEO-mimetic peptoid homopolymers with lithium salts studied as new polymer electrolytes. Image adapted with permission from ref. 40. Copyright 2012 American Chemical Society. (F) A peptoid collagen mimetic. Image adapted with permission from ref. 39. Copyright 1998 Wiley.

1.1 Biomolecule Surface Chemistry

For many of the designed biomaterials described above to be realized, the desired biomolecule must be deposited onto a surface. Peptides and proteins can be attached noncovalently onto surfaces, such as mica or graphite, or covalently onto functionalized metal surfaces. Covalent functionalization methods tend to be more robust and reproducible.[42] A number of biorthogonal strategies have been developed for the covalent functionalization of peptides to surfaces including oxime linkages[43], thiol-ene reactions[44], copper-mediated click reactions[45], His-Tag adsorption[46], and surface aldehyde functionalization.[47] However, the most popular method is self-assembly on gold though Au-S bonds. The creation of self-assembled monolayers (SAMs) of peptides draws on the vast literature surrounding the formation of alkanethiol SAMs on gold substrates.[48-51] Alkanethiol SAMs are formed by simply dipping the substrate into a solution of the desired alkanethiol(s). The mechanism of formation is thought to consist of a fast nucleation at the surface, followed by slow growth, chain rearrangement, and coalescence of vacancy islands, ultimately creating a well-ordered, densely packed two-dimensional surface.[9] Hydrophobic, van der Waals interactions drive the ordered packing of these monolayers.
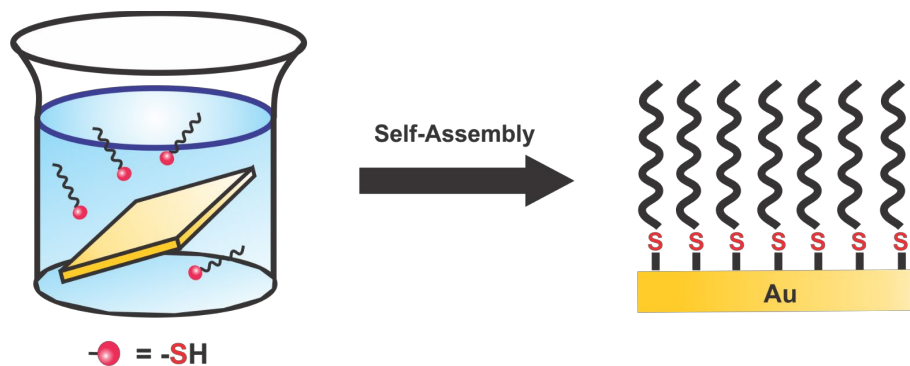
Figure 4. Self-assembly scheme for short, helical peptides onto a gold surface. Similar to alkanethiol SAMs, densely packed and well-ordered peptide SAMs are formed when a gold surface is dipped into a peptide solution.

Short, hydrophobic peptides have been shown to form densely packed SAMs, similar to alkanethiol SAMs (**Figure 4**).[52] Peptide SAMs are formed in a similar manner, this time relying on the interchain interactions among nearby oligomers. Peptides are readily incorporated into self-assembled monolayers on gold through functionalization of the peptide with a thiol group, disulfide group, or utilizing the naturally occurring cysteine side-chain.[9] Foldamer SAMs have also been investigated. The Huc lab constructed single monolayers of helical oligo-quinolinecarboxamide foldamers on gold substrates and observed efficient vertical charge transport.[53] Gellman and Abbott explored SAMs formed by β-peptides, which may have advantages such as increased proteolytic stability compared to α-peptides.[54] Polarization modulated infrared reflection absorption spectroscopy (PM-IRRAS) studies revealed the effect of β-peptide sequence on SAM internal order, wherein the globally amphiphilic peptide produced highly organized SAMs.[54] Non-globally amphiphilic β-peptide SAMs revealed a higher degree of disorder (**Figure 5**).
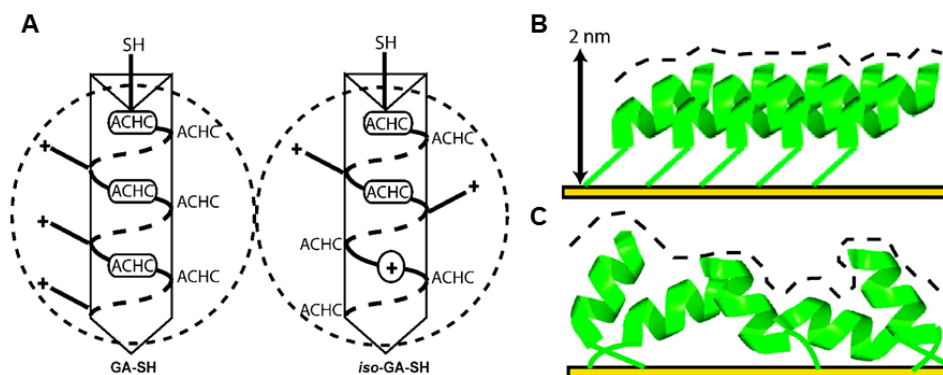
Figure 5. (A) Design for a globally amphiphilic β-peptide (GA-SH) and its isomer (*iso*-GA-SH), which has an even distribution of hydrophilic side chains. (B) A respresentation of the SAM packing of GA-SH and (C) *iso*-GA-SH as determined by PM-IRRAS. Image adapted with permission from ref. 54. Copyright 2007 American Chemical Society.

Creation of peptide SAMs is a particularly useful strategy for the construction of bioelectronic devices because the attachment of the peptide to a surface provides a mechanism to control the direction and magnitude of the molecular dipole relative to the surface. The directional electron transfer through an α-helical peptide can be controlled by the orientation of the molecular dipole, which was demonstrated by attaching an α-peptide to a surface via the N and C terminus, respectively, effectively switching the direction of the molecular dipole with respect to the gold substrate.[55] Similarly, helical peptides carrying a redox active ferrocene moiety were used to show that the electron transfer rate is dependent on the helix dipole direction relative to the surface.[56] Devices created by the Ashkenasy lab used artificial coiled-coil peptides in parallel or antiparallel configurations that were self-assembled into monolayers with a pre-determined dipole orientation.[57] The direction and magnitude of the molecular dipole effectively modulated the gold work function (**Figure 6**), again highlighting the advantages of merging designed peptides and SAMs to create functional materials.[57] Recently, research from the Waldeck lab and others has emphasized the important role of chirality for the electronic properties of helical peptide SAMs.[58]

The spin filtering of electrons by α-helical peptide SAMs on gold was demonstrated and explained through the chiral-induced spin selectivity (CISS) effect, which has implications for charge transport and displacement in monolayers with chiral symmetry.[58]
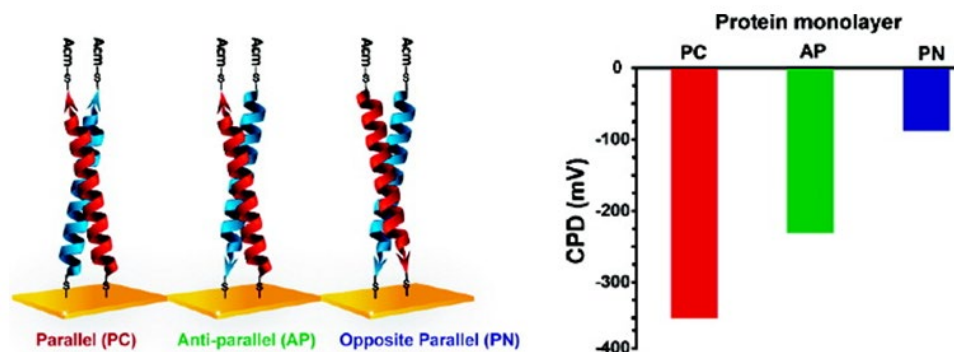
Figure 6. Coiled-coil based SAMs designed to have different dipole orientations relative to the surface can be used to modulate the gold work function. Image adapted with permission from ref. 57. Copyright 2010 American Chemical Society.

1.2 Peptidic and Bio-inspired Piezoelectrics

A particularly interesting class of bioelectronics are piezoelectric materials, which are materials that exhibit an "electromechanical" response. For such materials, an electrical impulse is coupled to a mechanical action. Piezoelectric materials have a wide range of applications including self-powered sensors, micro-electro-mechanical systems (MEMS), and energy harvesting devices.[59] Inherent piezo- phenomena are well documented in biological systems such as cellulose, collagen, DNA, proteins, and polysaccharides.[60-62] The creation of bio-inspired piezoelectric materials aims to take advantage of the inherent electromechanical properties present in many bio-architectures, with the goal of tuning these native properties for specific applications.

10

Hindering the creation of such piezo-materials is the poorly understood relationship between molecular properties and the magnitude of a molecule's piezoelectric response.

The piezoelectric effect is a reversible physical occurrence observed when a material converts electrical energy into mechanical energy and vice versa. This phenomenon is captured numerically through the piezo coefficient (d_{33}) which is a measure of the percent geometry change generated by an applied field (converse effect) or the electrical charge created by an applied force (direct effect) along the molecular breathing mode (z-axis).[63] Materials exhibiting piezoelectric response are non-centrosymmetric, polar, and poorly conductive. Common, well-documented piezo-materials include lead zirconate titanate (PZT), zinc oxide (ZnO), and quartz with piezoelectric coefficients of 300-500 pm/V,[64] 12 pm/V,[65] and 2.3 pm/V,[66] respectively. The robust responses of these materials are counterbalanced by a number of practical issues. For instance, these materials are inflexible and brittle, which can result in cracking, and they often require high temperatures and voltages for dipole alignment.[67-68] Additional drawbacks of the widely used piezoelectric, PZT, are the toxic effects of lead containing devices that make their implementation concerning due to the possibility of lead poisoning and environmental pollution.[69] Although lead-free piezoelectrics have been reported, few come close to the high piezoelectric coefficients observed in PZT, thus, they are insufficient for high demanding energy harvesting applications (**Figure 7**).
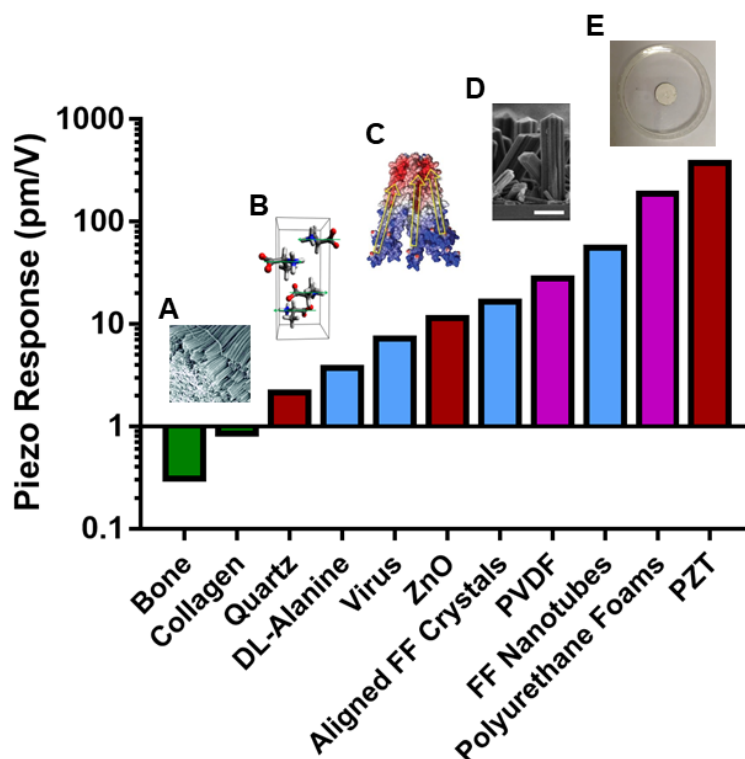
Figure 7. Comparison of the measured piezo response (d_{33}) in pm/V of bulk biological materials (green), inorganic materials (red), polymer-based materials (purple), and bio-inspired materials (blue). Examples depicted include (A) Bulk collagen. Image adapted with permission from ref. 70. Copyright 2018 Royal Society of Chemistry. (B) DL-alanine films. Image adapted with permission from ref. 71. Copyright 2019 American Physical Society. (C) M13 bacteriophage. Image adapted with permission from ref. 72. Copyright 2012 Nature Publishing Group. (D) Aligned peptide crystals. Image adapted with permission from ref. 73. Copyright 2016 Nature Publishing Group. (E) PZT ceramics. Image adapted with permission from ref. 68. Copyright 2015 Taylor and Francis Publishing Group.

Though most of the well-studied piezoelectrics are inorganic materials, piezoelectricity has also been observed in semicrystalline polymers, such as polyvinylidenefluoride (PVDF) (d_{33} = 33 pm/V), and polar small molecules, such as 2-methyl-4-nitroaniline (d_{33} = 14 pm/V) and *DL*-alanine films (d_{33} = 4.8 pm/V).[71, 74-76] Organic small molecule and polymer crystals often exhibit piezoelectricity due to non-covalent interactions, such as hydrogen bonding and π-stacking, that permit the material to be easily deformed.[76] These materials can also have valued attributes such as low force and dielectric constants as well as high polarizability.[71, 76] Polymer-based foams, such

as molecularly doped polyurethane foams, display a very high piezo response (d_{33} = 150-200 pm/V) arising from substantial polarizations and large volume changes under an applied force.[77]

Natural bulk materials typically show small piezo-coefficients (d_{33} = 1-5 pm/V), though some bio-inspired systems have been engineered to produce larger responses.[78] One study reported piezoelectric dipeptide nanotubes constructed via the self-assembly of diphenylalanine peptide monomers that are polarized along the tube axis and estimated to have a piezo-coefficient of about 60 pm/V.[67] Another study describes the piezoelectric response of a M13 bacteriophage; increased charge distribution, created by engineering in greater densities of oppositely charged amino acids at either termini, produced a large macrodipole in the virus resulting in increased piezo activity.[72] The Achilles tendon of ox and horse, which is comprised of aligned collagen fibers, is an early example of piezoelectric response in natural bulk materials;[61] however, recent work by the Thompson lab has shown that crystals of collagen subcomponents (alanine-hydroxyproline-glycine trimers) yield an increase of two orders of magnitude in piezo response over macroscopic collagen.[70] Aligned diphenylalanine peptide crystals have also demonstrated a significant piezo response.[73, 79] Arrays of these polarized crystals were sandwiched between two electrodes to demonstrate the power generation resulting from compression of the device.[73, 79] Lastly, composite polymer piezoelectric films were fabricated from rod-like, α-helical fibrils composed of poly(γ-benzyl α,L-glutamate) (PBLG) and had a response of 23 pm/V.[80]

A major barrier to the design of new bio-inspired piezo-active molecules is the lack of understanding regarding what molecular properties give rise to a strong piezoelectric response. Enhanced understanding of the mechanisms giving rise to piezoresponse will enable the bottom-up design of new systems that address practical needs;[81] however, few studies have given insight into the fundamental properties required to increase piezo-response. In one such study, the

Hutchison lab showed promising results from density functional theory (DFT) calculations on [6]helicenes and their analogues that predict d_{33} values greater than current organic and even some inorganic piezoelectrics.[63] They also showed that deformation in these systems is driven by conformational changes rather than covalent bond stretching.[63] Although synthetic inaccessibility remains an issue in realizing the helicene-based systems, valuable knowledge can be gained regarding key properties of the molecules that gave significant d_{33} values. These results suggest that the two key features necessary for piezo response at the molecular level are (1) a dipole moment to couple to the applied electric field and (2) a deformable conformation along a low-energy vibrational mode. Using standard self-assembly techniques, one can easily create monolayers with intrinsic polar order to screen molecules for the above properties.[82] As a proof of concept, the Hutchison lab demonstrated piezo response in simple oligo-alanine peptide SAMs.[82] Comparison of the oligo-alanine peptide monolayer to simple alkane monolayers indicated the conformational flexibility of the polypeptide backbone was essential for piezoresponse.[82] This work served as one of the main inspirations for my investigations into the molecular origins of peptide and foldamer piezo response.

1.3 Surface-bound Versus Bulk Solution: The Effect on Peptides and Proteins

Amino acid sequence is the primary determinant of protein folding and function. When a peptide or protein is anchored to a surface, the monolayer itself may also affect folding behavior and thereby, properties. The environment a peptide encounters at the surface is very different from its environment in solution due to increased molecular crowding and potential interactions with the surface itself. A number of studies, using a range of surface characterization techniques,[83] have

indicated that peptide and protein folding behavior can change drastically between a free solution and surface bound context. Using on-surface circular dichroism, the Wälti lab showed that the α-helical secondary structure of a synthetic coiled-coil peptide, which was not present under identical solution conditions, can be induced and stabilized by a densely packed monolayer.[84] Molecular crowding of immobilized proteins within a high-density monolayer has also been shown to influence the kinetics and thermodynamics of protein-ligand interactions.[85] The Latour group demonstrated that proteins adsorbed to artificial surfaces can exhibit structural changes based on the amount of protein adsorbed and the functional groups present at the surface (**Figure 8**).[86] Human fibrinogen was adsorbed onto alkanethiol SAMs with varying terminal groups from solutions of different protein concentrations.[86] The terminal group at the surface can either promote or prevent protein adsorption through interactions with amino acids at the protein interface. In this case, increased hydrophobicity of the terminal group led to larger amounts of protein adsorption and a higher degree of structural change from the native conformation.[86]
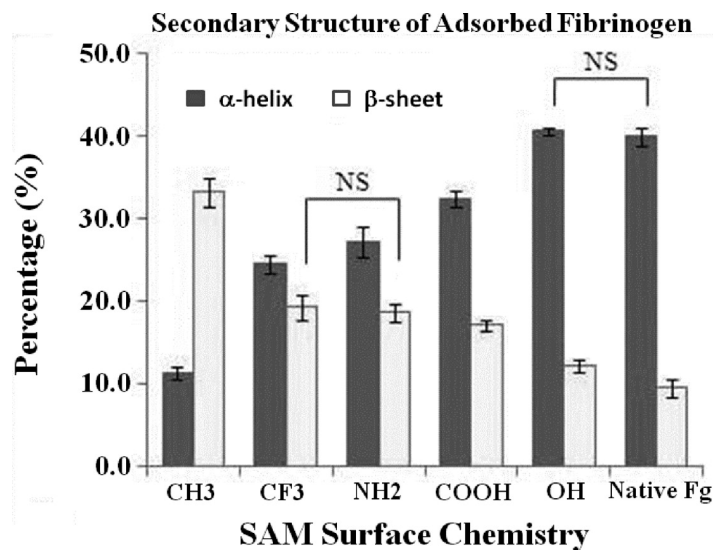
Figure 8. Changes in secondary structure of adsorbed human fibrinogen (Fg) in functionalized SAM surfaces made from 0.1 mg/mL Fg in PBS solution. Changes were determined by CD of the SAMs compared to native

conformation. (n = 6, mean ± 95% CI). (NS denotes not significant, all other values are significantly different from one another; $p < 0.05$). Reproduced with permission from ref. 86. Copyright 2009 American Chemical Society.

The field of plasma polymers has also provided insights into biomolecule-surface interactions. An early study used competitive protein adsorption as a mechanism to understand the effect surface polarity has on protein-surface interactions. A mixture of human serum albumin (HSA), human IgG, and human fibrinogen (Fgn) was exposed to various plasma polymer surfaces, including hexamethyldisiloxane (PP-HMDSO), acrylic acid (PP-AA), and 1,2-diaminocyclohexane (PP-DACH).[87] While adsorption of HSA and IgG were prevalent on hydrophobic PP-HMDSO, Fgn was found to be the prominent protein adsorbed on positively and negatively charged surfaces (PP-DACH and PP-AA, respectively).[87] The catalytic function of enzymes adhered to plasma modified surfaces has also been an area of interest. Generally, better retention of protein function occurs when the protein is covalently bound to hydrophilic plasma polymer surfaces.[88]

Studies comparing mammalian cell adsorption on synthetic surfaces bearing plasma polymers was also carried out.[89] In this case, plasma polymers were used to form chemical "gradients," going from hydrophobic to hydrophilic on a single surface.[89] By comparing water contact angles, it was shown that cellular adhesion to hydrophilic surfaces is greater than hydrophobic surfaces, reflecting an increase in cell density across the gradient.[89] Further studies indicate that the net negative surface charge of mammalian cells can be used to influence cellular adsorption onto surfaces.[90] Minimizing positive surface charge while maximizing negative surface charge can decrease cell adhesion and proliferation at the surface.[90] These studies on plasma polymer surfaces highlight the influence surface charge and polarity has on the adsorption of biomolecules and cells to surfaces as well as the functional capabilities of these molecules once bound to the surface.

16

Investigations into the folding thermodynamics of surface-bound proteins has also shed light on the various factors that stabilize or destabilize protein folds. Interactions at the protein-SAM interface can destabilize the native protein fold as evidenced in recent work by Plaxco, where the folding free energy of a surface bound FynSH3 domain was measured via a redox-active probe and found to be destabilized as compared to the bulk solution context (**Figure 9**).[91] However, Protein L, investigated by the same method, proved to be stabilized overall when introduced to the same hydroxy-terminated surface.[92] In these systems, enthalpic contributions are generally small and destabilizing due to favorable interactions with the SAM interface that better accommodate the unfolded state.[92] Entropic contributions are generally stabilizing, arising from excluded volume effects that restrict the number of conformations available upon surface attachment.[92] The interplay and magnitude of these effects, which are highly dependent on the protein as well as the properties of the surface, will determine whether surface attachment is ultimately favorable or unfavorable to native folding. These studies highlight the complexity of protein-surface interactions that make their folding, dynamics, and activity on a surface hard to predict.
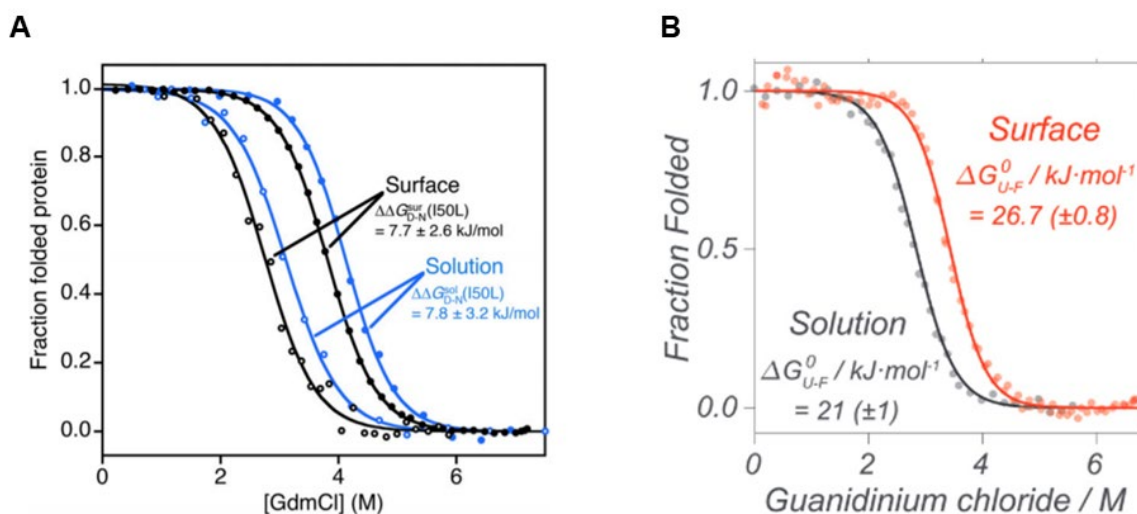
Figure 9. Experimentally determined change in folding free energy of (A) FynSH3 domain (I50L variant, open circles; FynSH3, closed circles) for the surface-attached protein (black) and the protein when it is free in bulk

solution (blue). Image adapted with permission from ref. 91. Copyright 2018 National Academy of Sciences. (B) Folding free energy of Protein L at the surface (red) and in bulk solution (black). Image adapted with permission from ref. 92. Copyright 2019 Wiley. While FynSH3 is destabilized when bound to a hydroxy-terminated surface, Protein L is overall stabilized by the same surface.

Biomolecule-functionalized surfaces have proven to be useful as sensors for small molecules and proteins. An early example is the functionalization of a gold surface with biotin which recognizes the protein streptavidin.[93] In this system, higher packing densities limited the binding ability of streptavidin.[93] Other examples include a structure -switching, redox-tagged DNA aptamer covalently bound to a gold surface via self-assembly that has been developed as an electrochemical sensor for the detection of cocaine and thrombin protein.[94-95] Detection was optimized by controlling the aptamer density at the surface as well as the length of the alkanethiol linker, which tethers the aptamer to the surface.[96] Immobilization of cytochrome c through the heme group onto mixed alkanethiol functionalized electrodes was studied by electrochemical methods,[97] paving the way for the development of multilayer cytochrome c electrodes for the sensing and quantification of superoxide radicals.[98] Surface plasmon resonance (SPR) biosensors are a popular detection and analysis tool that can detect analytes of interest in solution through biomolecular recognition.[99] The surface-bound biomolecule is often an antibody, peptide, or aptamer which is chemically and site-specifically bound in order to create a uniform alignment that orients the binding site towards the sample solution.[99] Finally, "smart" bio-interfaces using switchable surface coatings that respond to stimuli such as light, temperature, electric potential, pH, and ionic strength have been developed.[100] These next generation biosensors aim to provide control over biomolecular adsorption and desorption processes.

The implications of understanding how surface properties affect peptide folding and orientation extend far beyond the realm of piezo-active species to almost any bio-functionalized

surface application including biosensors, tissue engineering, implants, protein microarrays, and drug delivery vehicles.[91] Consistent implementation of peptides and proteins onto surfaces is irregular and difficult to predict. Harnessing methodology to create tailored and tunable surfaces that predictably alter biomolecule conformation warrants further study.

1.4 Project Goals

The major goals of the projects detailed herein are to understand and control molecular and surface properties that dictate the folding of peptides, proteins, and foldamers on surfaces and to elucidate how these conformations affect properties such as piezo response. In Chapter 2, I detail our efforts to gain a fundamental understanding of the molecular characteristics that create a strong bio-inspired piezoelectric. Properties such as conformational rigidity, folding propensity, chain length, dipole moment, and polarizability are investigated systematically with the ultimate goal of informing the design of an optimized piezoelectric. Through a combination of design, synthesis, and solution and monolayer characterization techniques, the inherent piezo coefficients of a number of peptidic and bio-inspired organic oligomers are analyzed revealing important principles for creating soft piezo materials.

In Chapter 3, I detail efforts to modulate surface properties, such as molecular crowding and polarity, as a means to further understand and control peptide-surface interactions and surface-bound folding. Understanding the complexities of peptide-surface folding will aid in the design of piezoelectrics, as well as an array of other useful biomaterials. To achieve this goal, a method for covalently modifying surfaces with biomolecules through copper-catalyzed click chemistry is

developed and utilized; this methodology allows for surfaces to be readily tailored for testing an array of surface conditions and biomolecules.

2.0 Molecular Properties Influence the Piezoelectric Response of Peptides, Peptoids, and Bio-inspired Oligomers

This chapter has been adapted with permission from

1. Marvin, C.W.*; Grimm, H. M.*; Miller, N. C.; Horne, W. S.; Hutchison, G. R. Interplay among Sequence, Folding Propensity, and Bio-Piezoelectric Response in Short Peptides and Peptoids. *J Phys. Chem. B* **2017**, 121(44), 10269-10275. (*equal author contribution)

2. Miller, N.C.; Grimm, H. M.; Horne, W. S.; Hutchison, G. R. Accurate Electromechanical Characterization of Soft Molecular Monolayers Using Piezo Force Microscopy. *Nanoscale Adv.* **2019**. Just Accepted.

Contributions:

This work was performed in collaboration with Christopher W. Marvin, Nathaniel C. Miller, and Geoffrey R. Hutchison and their specific contributions are as follows:

> *Christopher W. Marvin developed the AC voltage sweep DART-PFM methodology and aided in the collection of PFM data on the peptide and DDT monolayers (Figures 16-22). Nathaniel C. Miller assisted with the XPS measurements of peptide, peptoid, and DDT monolayers (Figures 23 and 24) and calculated the monolayer thickness from the these XPS results (Table 1). He also developed the DC voltage sweep methodology and re-collected PFM data on a subset of peptide and peptoid monolayers using his methodology (Figure 33 and Table 2). Geoffrey R. Hutchison performed density functional theory calculations on peptide and peptoid helices to determine the macrodipole.*

As alluded to in the introduction, the molecular properties that give rise to electromechanical response in bio-based materials is not well understood. Studies that experimentally evaluate the piezoelectric properties of biomolecules are far fewer than those describing bulk inorganic substrates. Properties thought to be important for piezo response in biomolecules include electrostatics, deformability, polarizability, and macrodipole moment; however, most of these have only been demonstrated through computation.[63, 76] Chapter 2 presents our "bottom up" approach, combining synthesis, characterization and self-assembly, to create tailored piezoactive surfaces. This approach is a unique method for developing piezoelectric materials and experimentally determining the molecular level properties that impact this response.

The first molecular property we sought to investigate was the relationship of peptide conformation to piezoelectric response. Underlying this choice was prior computational work performed by the Hutchison Lab which indicated that conformational deformations in single molecules can give rise to an electromechanical response.[63] Experimentally, this phenomenon was demonstrated via the measured piezo response in oligoalanine peptide monolayers (**Figure 10**).[82] Patterned single monolayers of oligoalanines were prepared and confirmed by AFM topography. Piezo response was then determined against a built-in background of bare gold. Comparison of oligoalanine peptide monolayers to simple alkane monolayers indicated that the conformational flexibility of the polypeptide backbone was essential for piezo response (**Figure 10**).[82]
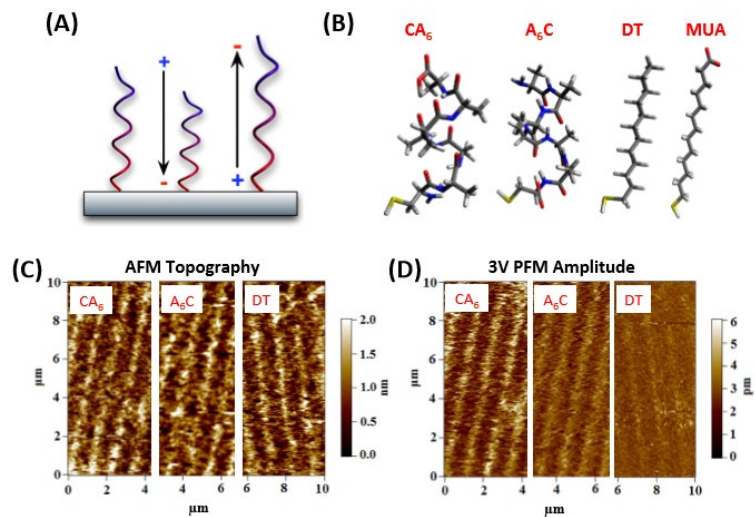
Figure 10. (A) Schematic of piezoelectric distortion through compression and extension of a molecular helix, (B) Molecular structures of oligopeptides CA_6, A_6C, and rigid alkanes DT and MUA, (C) AFM topography of oligopeptide CA_6 (left), oligopeptide A_6C (middle) and DT, (right) patterned monolayers, and (D) DART PFM amplitude at an applied bias of 3V for patterned CA_6, A_6C, and DT monolayers, showing contrast with bare gold. Reproduced with permission from author of ref. 82.

Not clear from these prior experiments was the potential role of peptide folding in the piezoelectric output. One possibility is that the α-helix, likely favored in the Ala-rich sequences, can act as a polar "molecular spring" that undergoes conformational deformation in an applied field (**Figure 11**). If true, this would imply a correlation between peptide helicity and the magnitude of piezo response. This chapter details our systematic study into the interplay among peptide chemical structure, folding propensity, and piezoelectric properties, uncovering in the process new insights into the origin of electromechanical response in peptides and related oligomers. Finally, a new DART-PFM, AC voltage sweep methodology was employed to sample piezo response over an array of peptide conformations.
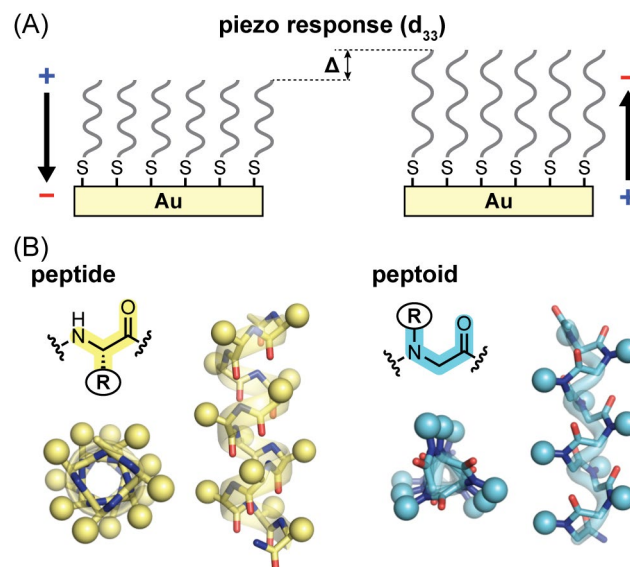
Figure 11. (A) Schematic depicting nanoscale piezo response of a self-assembled monolayer on gold upon applying an electric field. (B) Backbone chemical structures alongside models of the α-helix and PPI-helix folds formed by peptide and peptoid oligomers.

2.1 System Design and Solution Characterization

To evaluate the effect of helicity on piezo response, we designed a series of peptides (**1-3**) of identical length but varying folding propensity (**Figure 12**). Keeping the molecule size comparable among the series focuses the analysis of structure-function relationships on folding behavior. Peptide **1** is based on a previously reported sequence that is among the shortest known to show appreciable helical folded population in aqueous solution.[101] This characteristic results from the presence of three aminoisobutyric acid (Aib, U) residues that restrict backbone conformational freedom and promote the helical fold. We replaced the three Aib residues in **1** with either alanine (Ala, A) or glycine (Gly, G) to generate peptides **2** and **3**, respectively. Ala is also helix promoting, though to a lesser degree than Aib, while Gly is strongly helix disrupting. Each

24

peptide was functionalized with a thiol group at the N-terminus to provide an anchor point for attachment to gold in the fabrication of polar monolayers.
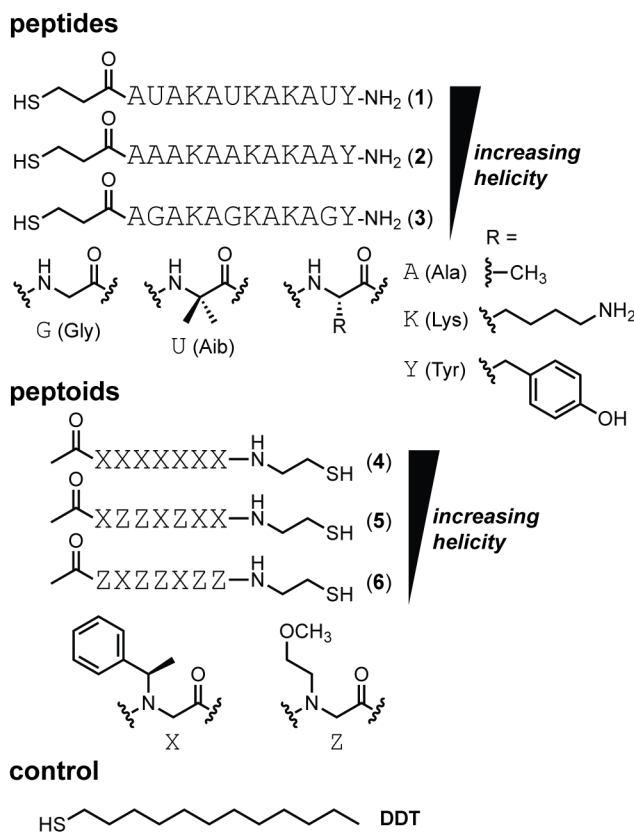
Figure 12. Peptides **1-3**, peptoids **4-6**, and control small molecule dodecanethiol (DDT).

A powerful strategy complementary to sequence modification for controlling folding in peptides is to alter the chemical structure of the backbone. Many backbone compositions differing from nature can give rise to discrete folding motifs.[25, 102-104] One of the first artificial scaffolds shown to manifest such behavior is the peptoid, a variant of the α-peptide backbone where each side chain is transposed from C_α to N.[31, 105] Folding in these structures is primarily driven by avoidance of steric clash between side chains and electrostatic repulsion between the π clouds of the aromatic side chains and the carbonyl backbone.[106] Peptoids are intrinsically more flexible than peptides; however, incorporation of α-chiral aromatic side chains such as the (R)-α-methylbenzyl moiety in residue X (**Figure 12**) gives rise to highly rigid chains that adopt polyproline-I (PPI)

helical folds.[105] The PPI helices formed by peptoids have ~ 3 residues per turn and contain *cis* amide bonds, rather than *trans* amide bonds found in peptide α-helices.[107, 108]

Following logic analogous to that applied in peptides **1-3**, we designed a series of peptoids (**4-6**) of identical length but systematically altered helicity by combining known structure-promoting (X) and structure-disrupting (Z) peptoid residues in varying fractions.[109-110] The macrodipole of the PPI helix (δ+ toward C-terminus) is oriented opposite that of a the α-helix (δ+ toward N-terminus). To keep the alignment of the helix dipole the same in the polar monolayers across the series of oligomers examined, we placed the thiol for anchoring to gold at the C-terminus in the peptoids through incorporation of a terminal cysteamine. Density functional theory calculations indicate the macrodipole for a 12-residue peptide α-helix (54 D) is approximately double that of a 7-residue peptoid PPI helix (27 D). Importantly, these values assume fully folded helical states, and the magnitude of the macrodipole will vary greatly with folded structure.

Peptides **1-3** and peptoids **4-6** were prepared by standard solid-phase methods (Fmoc strategy for the peptides, submonomer approach for the peptoids). Each oligomer was purified by preparative reverse phase HPLC, and the identity and purity of the final products were confirmed by analytical HPLC and MALDI-TOF mass spectrometry.

To establish that relative solution folding propensity in **1-6** followed the intended trends, we used circular dichroism (CD) spectroscopy (**Figure 13**). Solvent conditions for CD measurements were selected based on the solutions used for monolayer preparation (aqueous for the peptides, acetonitrile for the peptoids). The CD spectrum of peptide **1** showed minima at 222 and ~208 nm, characteristic of right-handed helical secondary structure. Moving through the series **1-3**, the band at 222 nm decreased in magnitude and the lower wavelength signal blue shifted to ~200 nm. These changes are both diagnostic of an increase in random coil character and support

our design hypothesis regarding the relative helicity across the series (**1** > **2** > **3**). Qualitative features of the CD spectra of the peptoids were consistent with the expected left-handed PPI helical fold. The decrease in the intensity of the band at 222 nm with increasing fraction of flexible Z residues supported the relative trend in helical character **4** > **5** > **6**. On an absolute scale, estimated folded populations (**Table 1**) vary from 3% for the least helical peptide (**3**) to ~100% for the most helical peptoid (**4**).
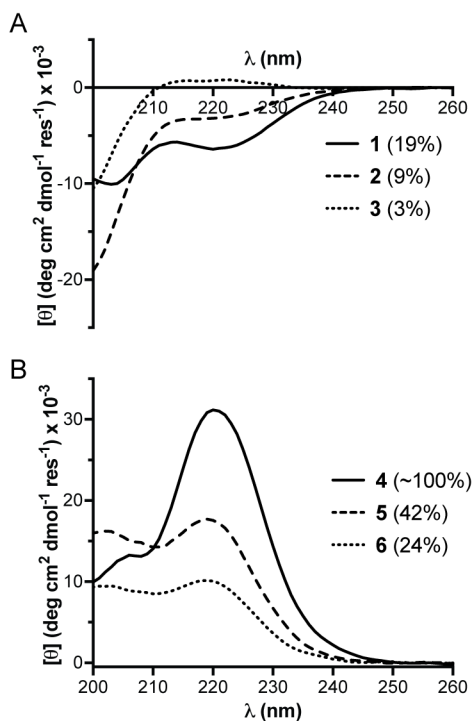
Figure 13. CD spectra of (A) peptides **1-3** (50 μM in 10 mM phosphate pH 7.2) and (B) peptoids **4-6** (50 μM in acetonitrile). Estimated helical folded population for each compound is indicated in parentheses.

2.2 Electromechanical Response and Surface Characterization

To compare the electromechanical response of the peptides and peptoids, monolayer films were deposited by solution self-assembly on gold substrates. Determining the piezo response of

these self-assembled monolayers (SAMs) entails the use of piezoelectric force microscopy (PFM), an AFM technique where an AC voltage is applied through a conductive tip in contact with the surface being analyzed (**Figure 14A**).[111] The resulting voltage-induced change in thickness (Δt) illustrates the SAM's piezoelectric character. However, the deflection of the cantilever encompasses components beyond just the deformation of the sample, namely electrostatic effects from tip-sample interactions, which can be difficult to quantify.
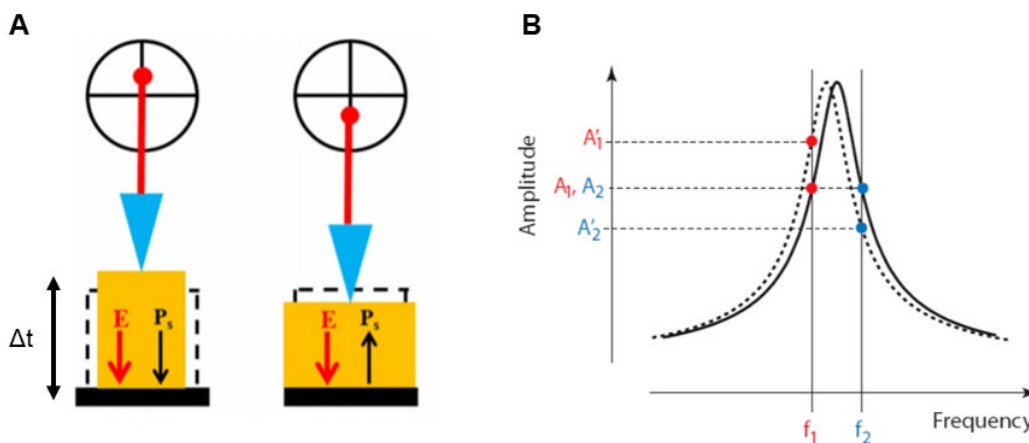
Figure 14. (A) PFM schematic. The direction of the polarization (P_s) and the applied electric field (E) cause an up or down displacement of the cantilever tip in contact with the surface. This motion is detected by a laser spot reflected onto a photodiode detector. Adapted with permission from ref. 111. Copyright 2017 Korean Ceramic Society. (B) Depection of the feedback loop using dual frequency-based resonance amplitude tracking in DART-PFM. Adapted with permission from ref. 112. Copyright 2007 IOP Publishing.

Upon attempting to characterize the peptide SAMs by PFM, low tune frequencies were noted, indicating poor signal to noise. Dual AC resonance tracking piezoresponse force microscopy (DART-PFM), a method developed by Kalinin, takes advantage of the increased signal to noise achieved when operating at the contact resonance frequency.[112] Unlike PFM, which operates at a single frequency, DART-PFM operates on a frequency feedback loop system that monitors two amplitudes bracketing either side of the contact resonance peak (**Figure 14B**). The

contact resonance is constantly tracked, leading to signal amplification. Because of this advantage, we decided to pursue DART-PFM to measure our peptide and peptoid SAMs.

Another concern in evaluating our SAMs was the precision and reproducibility of the measurement. It is common in the literature to see piezo response measured at only a single voltage, leading to difficulty in reproducibility and a poor sense of the experimental uncertainty. Therefore, we introduced an AC voltage sweep method. Using DART-PFM, we determined the Δt of each film by scanning with a series of applied tip voltages (1.5 to 4 V) and averaging across a $1~\mu m^2$ area for each voltage. The slope of a linear fit to a plot of Δt vs. applied voltage provides a measure of the piezoelectric response along the polarization axis (d_{33}). Ideally, the intercept of this line would pass through zero (i.e., no mechanical response with no applied field); however, due to electrostatic and tip-sample interactions, that is rarely the case. We repeated this experiment for each oligomer across independently prepared films on multiple days using different tips (**Figure 15, Table 1**). Averaging across multiple samples and tips minimizes artifacts arising from tip-surface interactions, and averaging across a large area (rather than a single point) for each measurement samples an ensemble of different molecular conformations and local environments. The validity of the methodology was supported by of the determination of the piezo response of quartz by the same approach, yielding a d_{33} (3.8 pm V^{-1}) close to the known value for d_{11} (2.3 pm V^{-1}).[66]
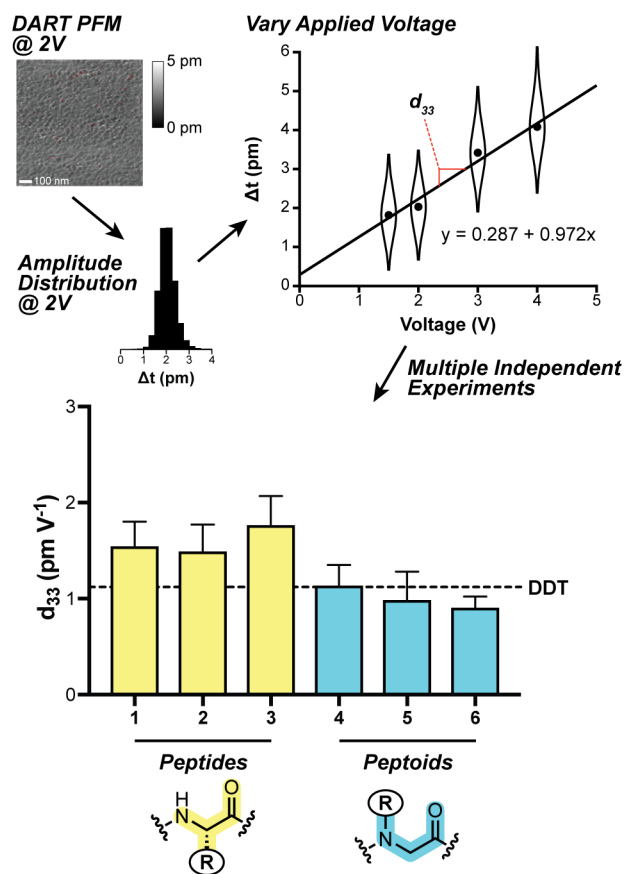
Figure 15. Summary of DART-PFM methodology used to determine piezoelectric response and the resulting d_{33} values obtained from replicate independent experiments with peptides **1-3**, peptoids **4-6**, dodecanethiol (DDT).

In general, across all monolayers of **1-6**, the distribution of piezo response showed high positive skewness, which did not have a clear trend with voltage (**Figures 16-22**). On the other hand, for five out of six compounds (**1-3**, **4**, and **6**) the distributions yielded voltage-dependent increases in peak width and standard deviation. For peptoid **5**, three out of four samples showed slight broadening with increasing voltage.
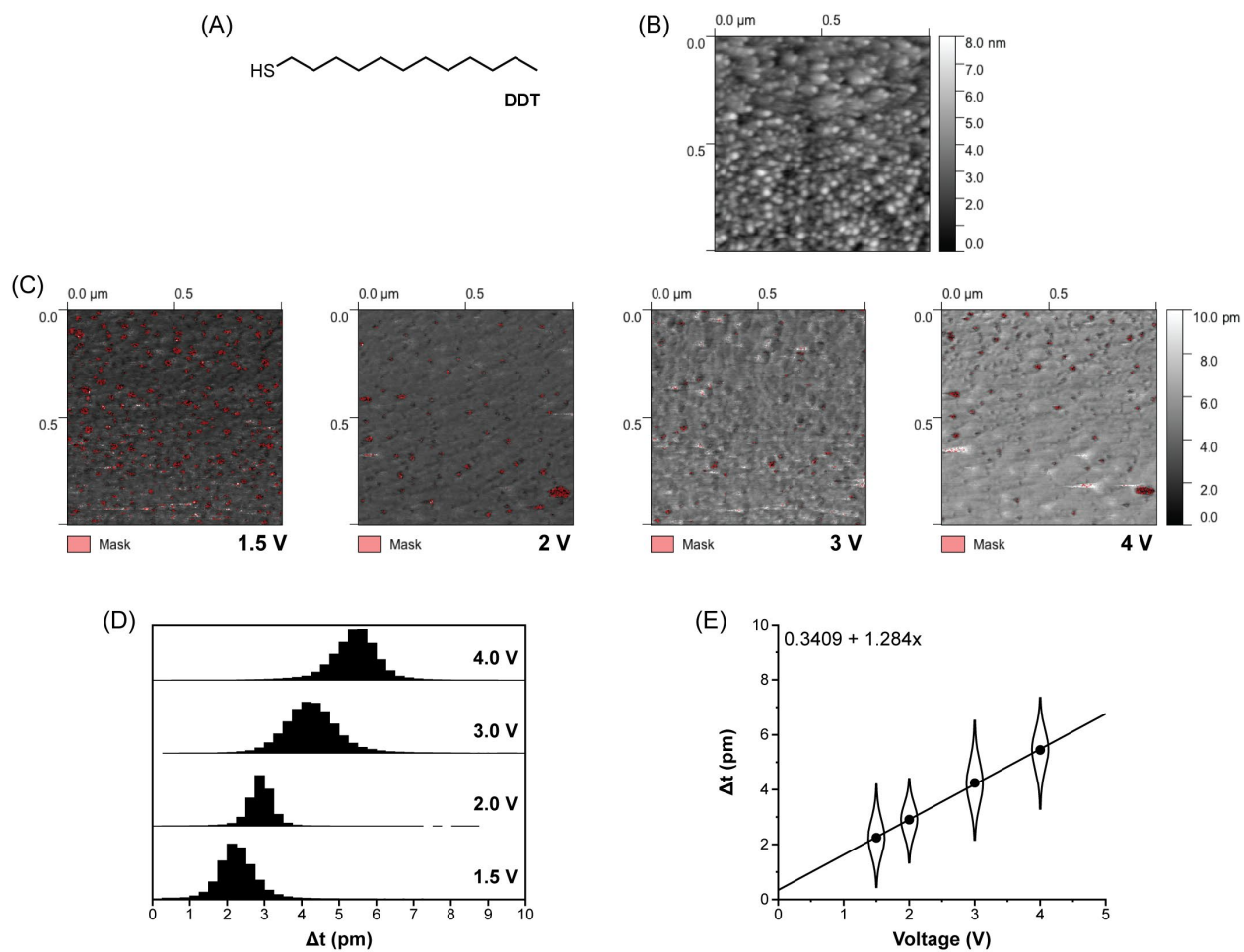
Figure 16. Representative raw DART PFM data for analysis of a self-assembled monolayer of **DDT** on gold. (A) Chemical structure of DDT. (B) Height image from DART-PFM measurement at an applied voltage of 1.5 V. (C) Images depicting q-corrected DART amplitude (Δt) at the indicated applied voltage. (D) Histogram analysis of the images shown in panel (C). (E) Linear regression of the histograms in panel (D) vs applied voltage; equation for the best-fit line is shown, where d_{33} is the slope.
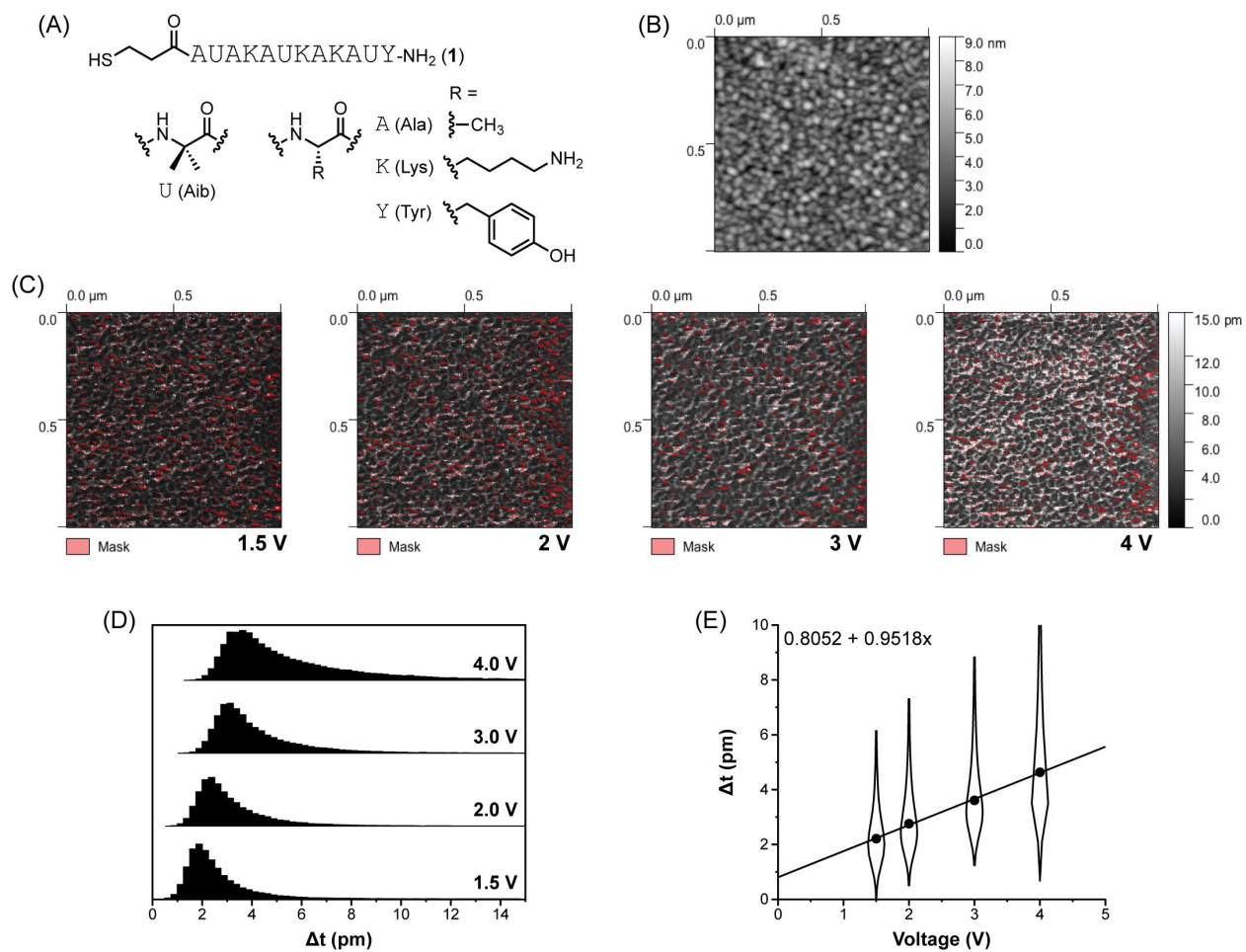
Figure 17. Representative raw DART PFM data for analysis of a self-assembled monolayer of peptide **1** on gold. (A) Chemical structure of peptide **1**. (B) Height image from DART-PFM measurement at an applied voltage of 1.5 V. (C) Images depicting q-corrected DART amplitude (Δt) at the indicated applied voltage. (D) Histogram analysis of the images shown in panel (C). (E) Linear regression of the histograms in panel (D) vs applied voltage; equation for the best-fit line is shown, where d_{33} is the slope.
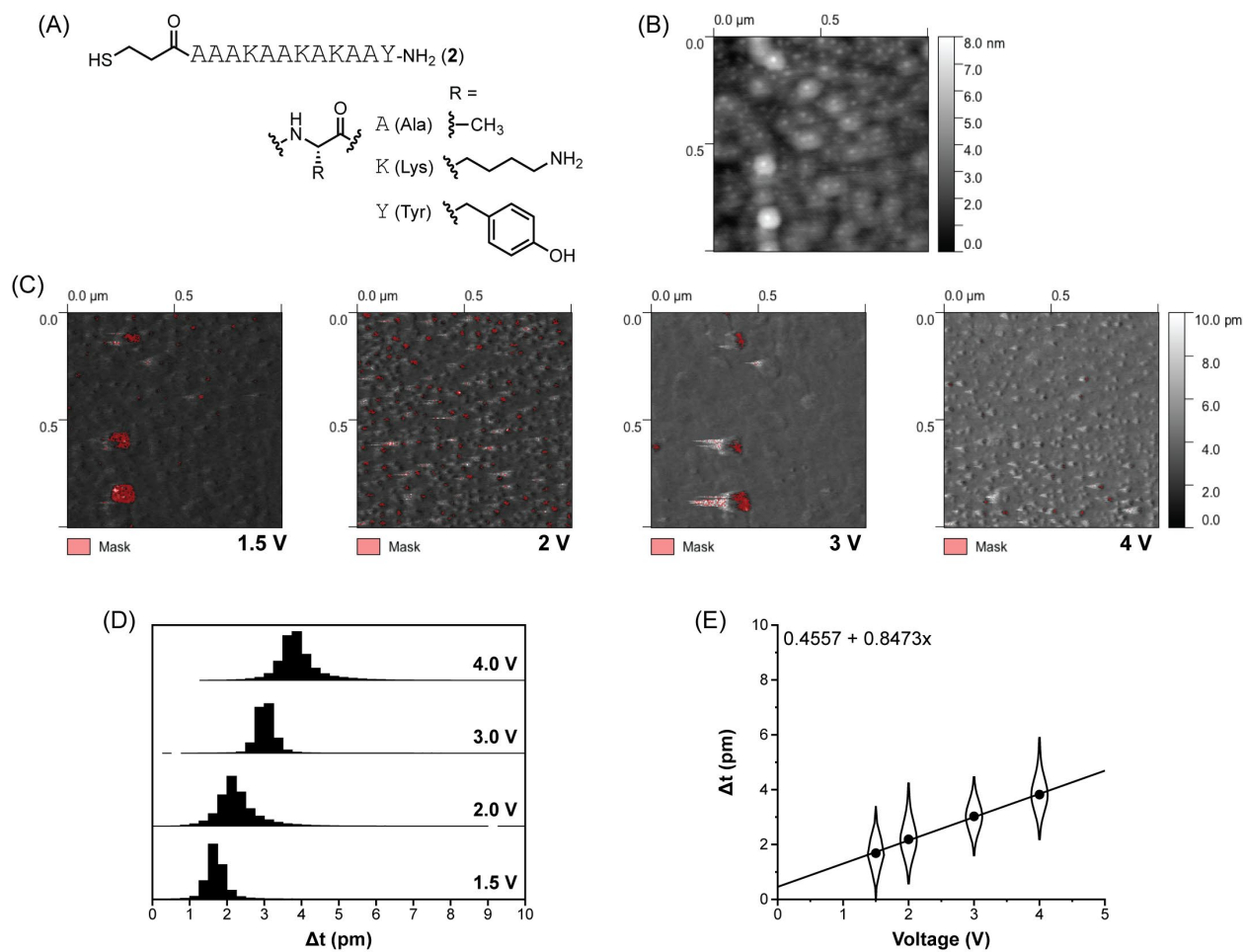
Figure 18. Representative raw DART PFM data for analysis of a self-assembled monolayer of peptide **2** on gold. (A) Chemical structure of peptide **2**. (B) Height image from DART-PFM measurement at an applied voltage of 1.5 V. (C) Images depicting q-corrected DART amplitude (Δt) at the indicated applied voltage. (D) Histogram analysis of the images shown in panel (C). (E) Linear regression of the histograms in panel (D) vs applied voltage; equation for the best-fit line is shown, where d_{33} is the slope.
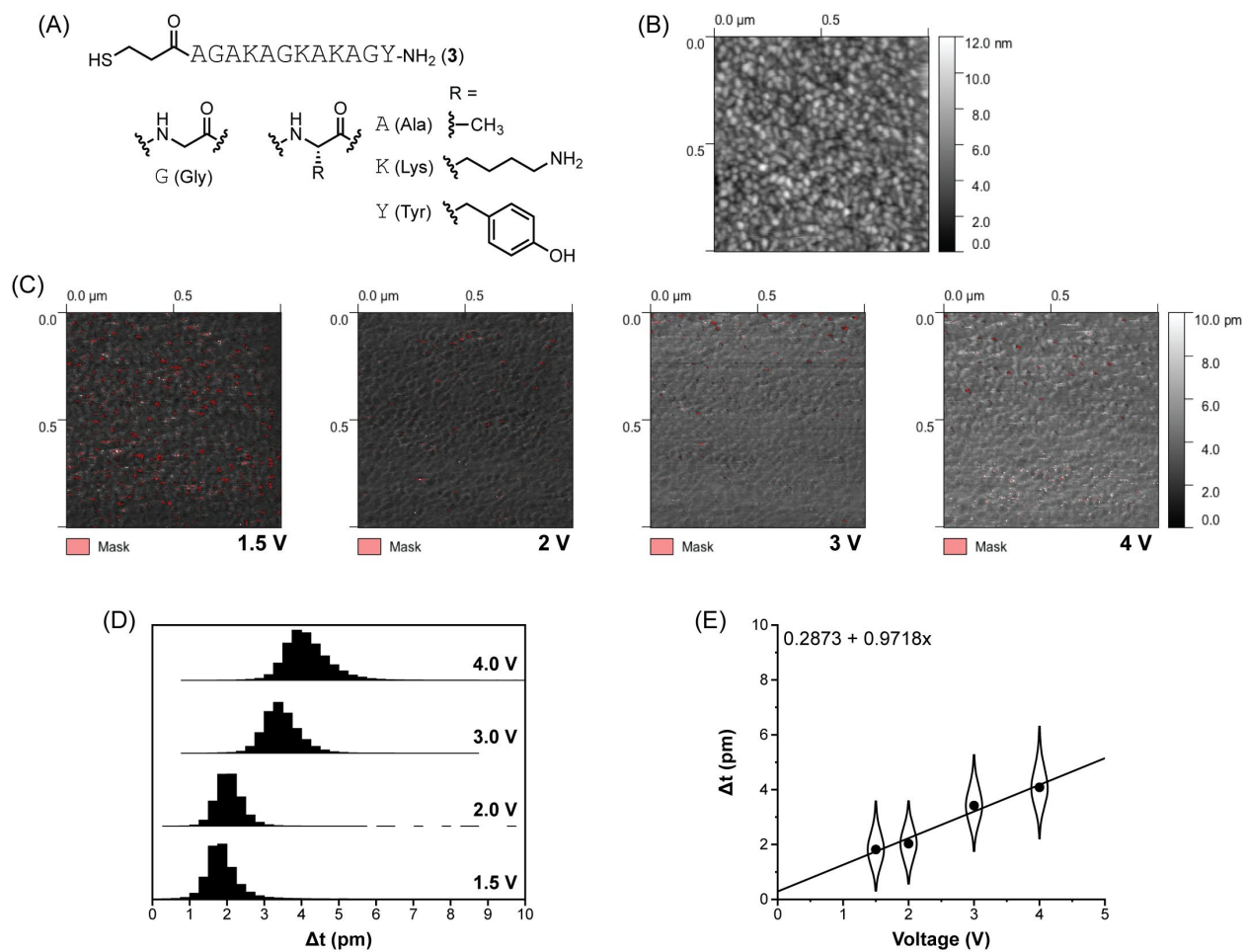
Figure 19. Representative raw DART PFM data for analysis of a self-assembled monolayer of peptide **3** on gold. (A) Chemical structure of peptide **3**. (B) Height image from DART-PFM measurement at an applied voltage of 1.5 V. (C) Images depicting q-corrected DART amplitude (Δt) at the indicated applied voltage. (D) Histogram analysis of the images shown in panel (C). (E) Linear regression of the histograms in panel (D) vs applied voltage; equation for the best-fit line is shown, where d_{33} is the slope.
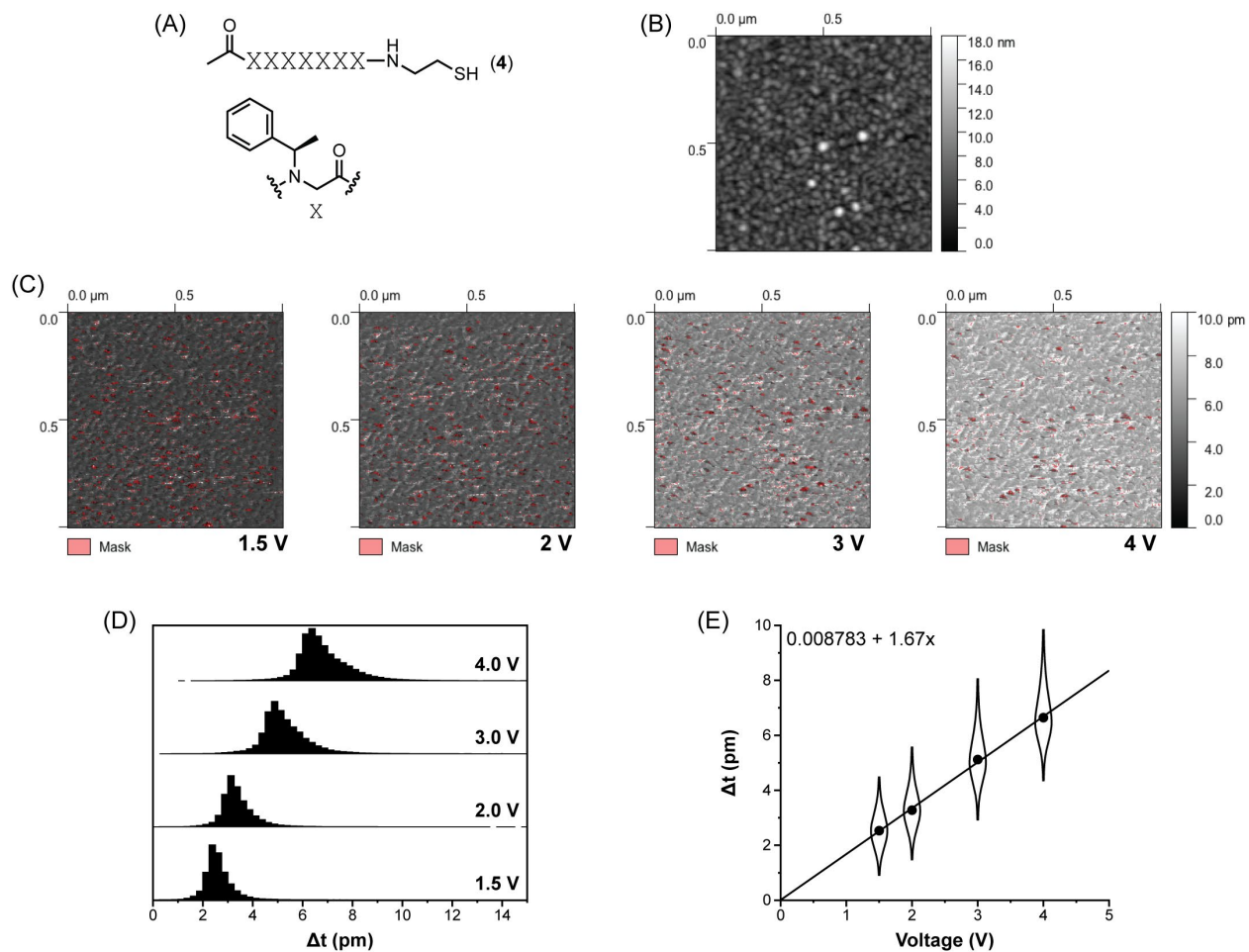
Figure 20. Representative raw DART PFM data for analysis of a self-assembled monolayer of peptoid **4** on gold. (A) Chemical structure of peptoid **4**. (B) Height image from DART-PFM measurement at an applied voltage of 1.5 V. (C) Images depicting q-corrected DART amplitude (Δt) at the indicated applied voltage. (D) Histogram analysis of the images shown in panel (C). (E) Linear regression of the histograms in panel (D) vs applied voltage; equation for the best-fit line is shown, where d_{33} is the slope.
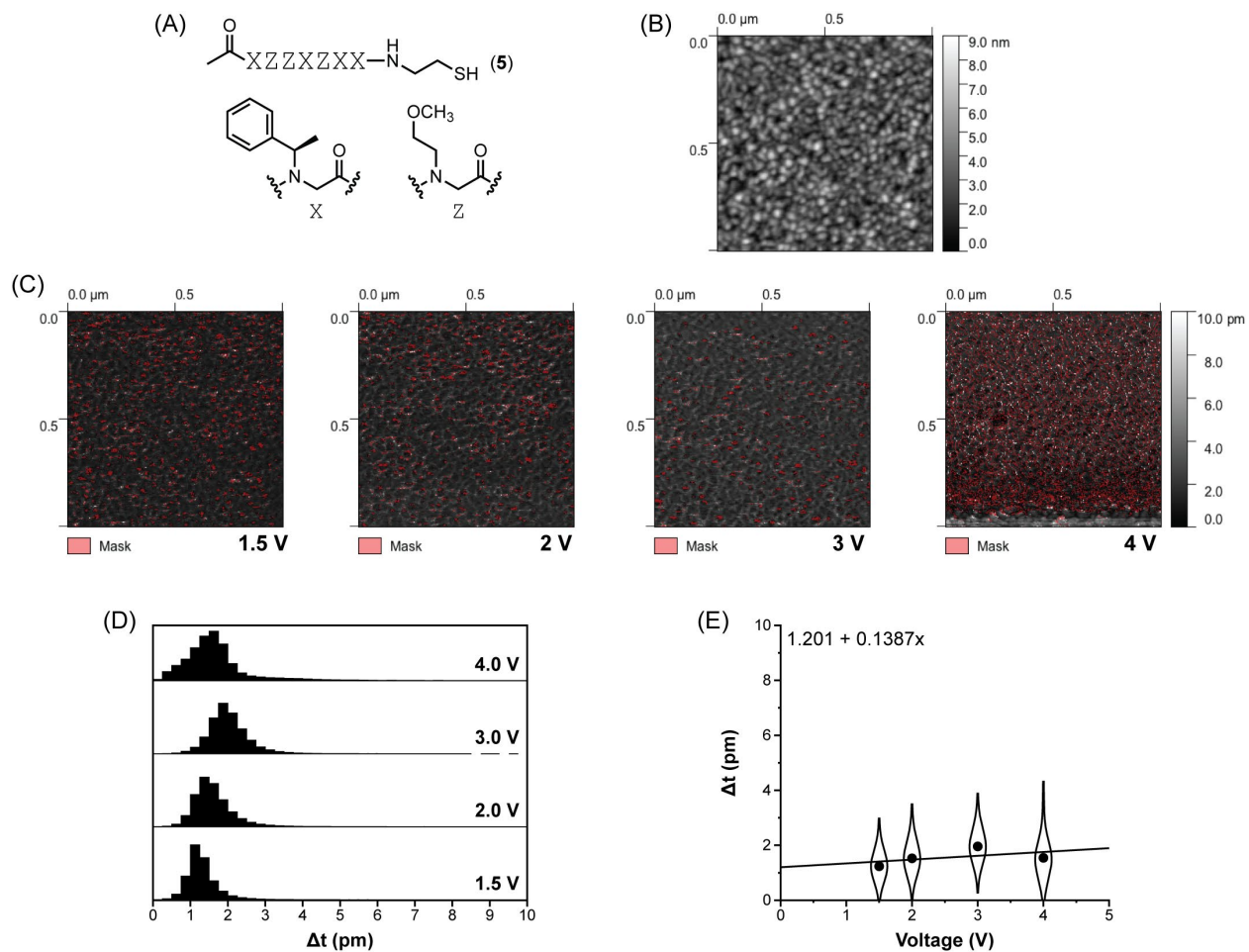
Figure 21. Representative raw DART PFM data for analysis of a self-assembled monolayer of peptoid **5** on gold. (A) Chemical structure of peptoid **5**. (B) Height image from DART-PFM measurement at an applied voltage of 1.5 V. (C) Images depicting q-corrected DART amplitude (Δt) at the indicated applied voltage. (D) Histogram analysis of the images shown in panel (C). (E) Linear regression of the histograms in panel (D) vs applied voltage; equation for the best-fit line is shown, where d_{33} is the slope.

Figure 22. Representative raw DART PFM data for analysis of a self-assembled monolayer of peptoid **6** on gold. (A) Chemical structure of peptoid **6**. (B) Height image from DART-PFM measurement at an applied voltage of 1.5 V. (C) Images depicting q-corrected DART amplitude (Δt) at the indicated applied voltage. (D) Histogram analysis of the images shown in panel (C). (E) Linear regression of the histograms in panel (D) vs applied voltage; equation for the best-fit line is shown, where d_{33} is the slope.

When comparing the two different backbone compositions, the average response from monolayers of peptides **1-3** was significantly greater than that of monolayers made up of **DDT** or peptoids **4-6** (p 0.016 for peptides vs peptoids) (**Figure 15**). On average, peptides **1-3** yielded PFM response ~41% larger than **DDT** and ~59% larger than peptoids **4-6**. Interestingly, no statistically significant trends beyond experimental uncertainty were discernable within a given backbone (i.e., among **1-3** or among **4-6**). While one might expect both peptides **1-3** and peptoids **4-6** to yield

much greater conformational flexibility than a straight-chain alkane such as **DDT**, the high packing density in the monolayers may diminish this difference. Placing these results in context of known bulk biomaterials that are piezoactive, the d_{33} of the peptide monolayers, while small, is greater than the response of bulk collagen (0.8 pm V^{-1}),[61] bone (0.29 pm V^{-1}),[113] and wood (0.04 pm V^{-1}).[114] It is likely that the parallel arrangement of molecular dipole moments in the monolayer samples enhances piezo response. Still, the magnitudes are modest compared to crystalline piezoelectric polymers, such as PVDF (~30 pm V^{-1}),[115] molecularly-doped polyurethane foams (~150-250 pm V^{-1}),[77] or PZT ceramics (~300-500 pm V^{-1}).[64]

To rule out the possibility that differences in piezo response observed resulted from differences in monolayer packing density rather than molecular structure, we carried out X-ray photoelectron spectroscopy (XPS). We determined the ratio of XPS peak intensities for sulfur versus gold signals for representative monolayers of **1-6** and **DDT**. Calibrating against a reported packing density for **DDT**,[116] we estimated the surface coverage density for the peptides and peptoids (**Table 1**). Variation among the observed packing densities were small and not sufficient to explain the observed differences in piezo response. Moreover, no significant trend was apparent based on backbone composition (peptides vs peptoids) or helicity in solution. We also used the XPS peak intensities for carbon versus gold signals to estimate monolayer thickness, following published methods previously applied to peptide SAMs.[116] As with monolayer density, no clear correlations were observed to folding propensity or backbone composition (**Table 1**), although the value for peptide **2** was somewhat lower than the rest of the series.

Table 1. Solution folding and monolayer properties for peptides **1-3** and peptoids **4-6**.

compound	d_{33} (pm V^{-1})[a]	n[a]	Monolayer properties density (molecules cm^{-2} x 10^{14})[b]	thickness (nm)[b]	Fraction helical (%)[c]
1	1.53 ± 0.27	8	3.3 ± 0.4	2.34 ± 0.06	19
2	1.48 ± 0.29	6	4.0 ± 0.4	2.03 ± 0.08	9
3	1.75 ± 0.32	6	3.9 ± 0.4	2.56 ± 0.06	3
4	1.12 ± 0.23	4	4.1 ± 0.1	2.52 ± 0.02	100
5	0.97 ± 0.31	4	4.2 ± 0.1	2.45 ± 0.03	42
6	0.89 ± 0.13	4	4.3 ± 0.2	2.58 ± 0.02	24
DDT	1.12 ± 0.25	4	4.6[d]	1.5[d]	–
Quartz	3.80 ± 0.50	2	–		–

[a]Average ± SEM for piezo coefficient (d33) as determined from n independent PFM experiments. [b]SAM density and thickness, as estimated from XPS.[116] [c]Fraction helicity as estimated by CD in solution (water for **1-3**, acetonitrile for **4-6**). [d]From ref. [116].

Additionally, the XPS data showed the chemical integrity of the peptide and peptoid monolayers (**Figures 23 and 24**). The presence of an amide nitrogen peak at 400 eV in the N1s region for all peptide and peptoid samples was absent in the control DDT confirming the presence of peptide and peptoid monolayers. Furthermore, a single peak at 162 eV in the S2p spectra was observed for all SAMs, indicative of the sulfur to gold bond. Older or improperly stored SAMs showed an additional S2p peak at 168 eV, commonly attributed to sulfoxides. Therefore, sulfur-

gold linkages were also evaluated to ensure they were not oxidized over the course of sample preparation and storage.
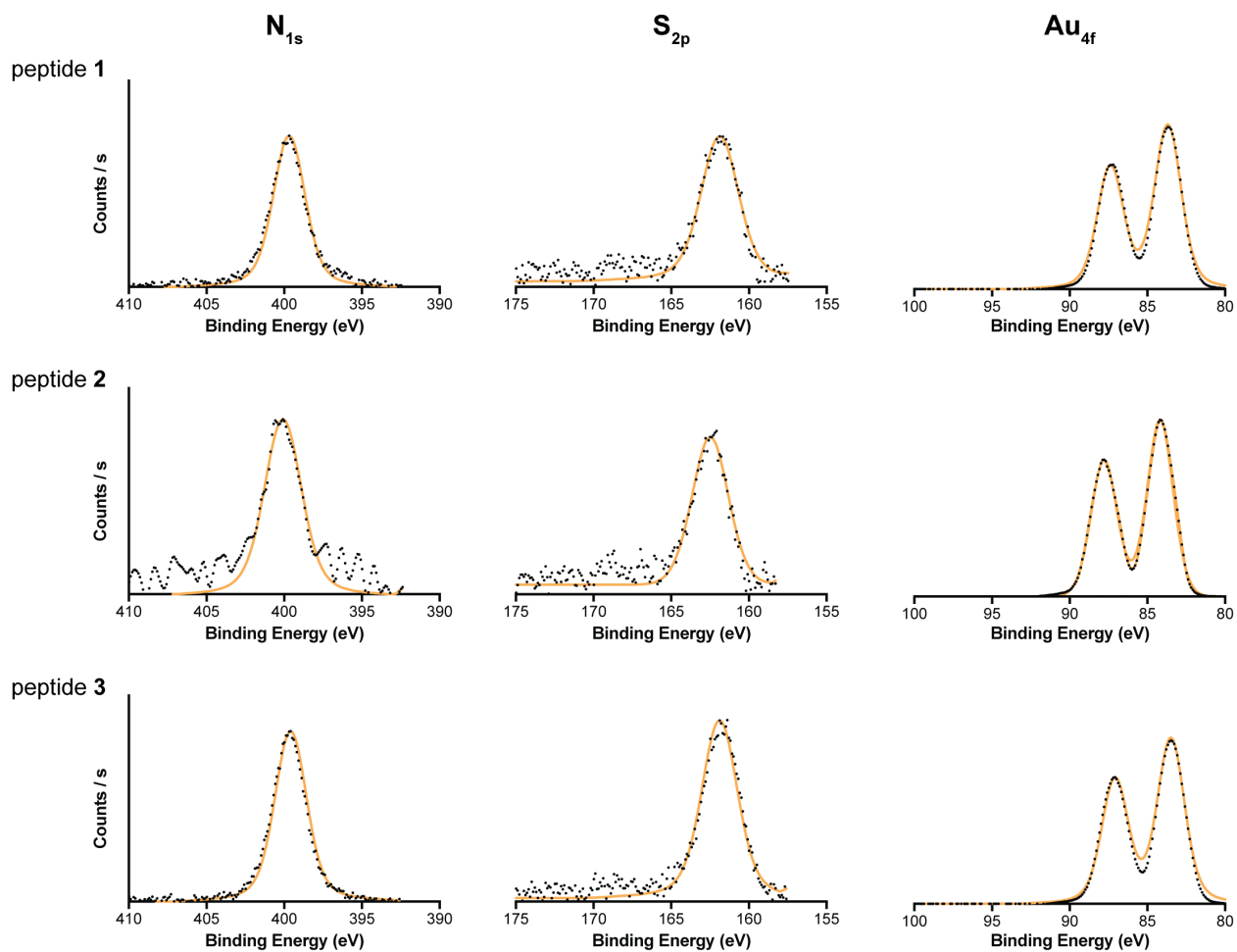
Figure 23. Representative N_{1s}, S_{2p}, and Au_{4f} XPS spectra for peptides **1-3**.
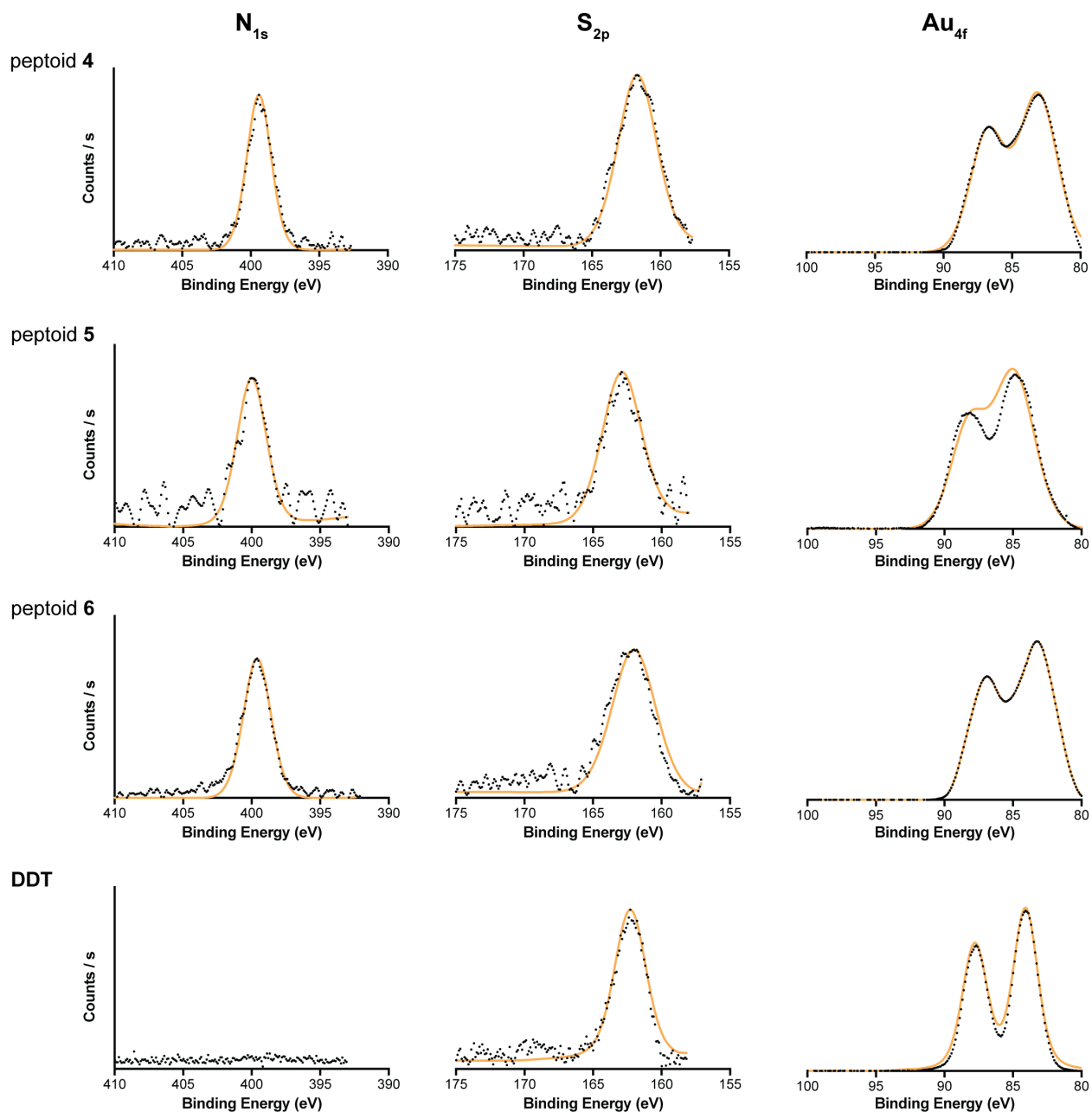
Figure 24. Representative N_{1s}, S_{2p}, and Au_{4f} XPS spectra for peptoids **4-6** and control dodecanethiol (**DDT**).

In an effort to gain information about folding by an analytical method applicable both in solution and SAM contexts, we turned to infrared spectroscopy. The amide I band (1600- 1700 cm^{-1}), arising from C=O stretching vibrations in the peptide backbone, is used to analyze secondary structural components in peptides.[117] Changes in hydrogen bonding patterns or amide bond geometry affect vibrational frequencies, ultimately shifting the peak maximum.[118-117] In solution

FTIR spectra of peptides **1-3** acquired in D_2O (**Figure 25A**), the amide I band observed shifts from ~1641 to ~1650 cm^{-1} across the series. We interpret this as corresponding to 3_{10}-helical secondary structure shifting toward increasing random coil,[119-120] consistent with the trend observed by CD. A consistent shoulder is observed at 1672 cm^{-1} in each spectrum from residual TFA remaining after HPLC purification and lyophilization.[121]

Polarization modulated infrared reflection absorption spectroscopy (PM-IRRAS) was chosen as the FTIR method to analyze our thin monolayer films due to its high degree of sensitivity and ability to minimize atmospheric contributions to the spectra. PM-IRRAS of the peptide monolayers showed amide I bands for peptides **1** and **2** ~1667 cm^{-1} (**Figure 25B**). Others have interpreted such spectral features for peptide SAMs to correspond to α-helical or distorted α-helical secondary structure.[122-123] The amide I band of peptide **3** appears at a higher frequency, ~1674 cm^{-1}, which we interpret as reflecting increased random coil character. An important caveat in the above analysis is that the complexity of the amide I region for all the peptide monolayers indicates a highly heterogeneous ensemble of folded states present at the surface.
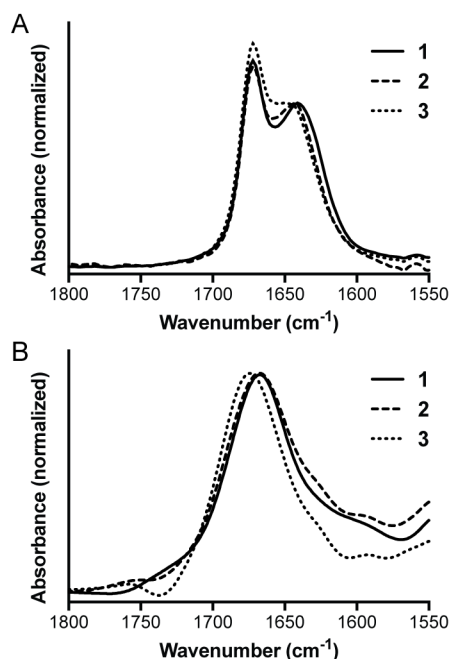
Figure 25. Amide I region from (A) solution FTIR spectra of peptides **1-3** (5 mg/mL in D2O) and (B) PM-IRRAS spectra of peptide monolayers on gold.

In summary, our initial hypothesis on the molecular basis for piezoelectric response focused on the effect of helical conformational preferences and the magnitude of the piezo response. That is, as "molecular springs," an unstructured peptide **3** would show low response. The data here argue the opposite is true and that a balance between helicity and flexibility is needed for increased molecular piezoelectric response. Small changes in helical secondary structure between peptides **1-3** results in no statistical difference in measured piezo response; however, more rigid peptoids **4-6** show significantly lower response, on par with the control **DDT** alkane thiol monolayer.

2.3 Investigations of Other Molecular Properties and Their Relationship to Piezo Response

Since bio-based piezoelectrics have not been extensively explored, we began this project with limited knowledge of the mechanisms governing a strong piezo response and little experimental precedent for measuring electromechanical response of soft, flexible materials. When it came to designing molecules, our approach was to sample a variety folds, backbones, and properties to pinpoint which design features result in the largest effects on piezo response. Computational research indicated that a strong dipole moment, enhanced through folded structures that align individual dipoles in a single direction, and a high degree of polarizability are important factors for a strong piezo response.[63] Therefore, in addition to the effect of conformational preferences which was exemplified by the peptide and peptoid systems, we also explored the effects of length and polarizability. For the former, we designed peptide **7** that was double the sequence length of peptide **1**, the most helical of our original peptide series (**Figure 26**). We hypothesized this peptide would be more helical than **1**, possess an increased dipole moment due to more aligned dipoles, and therefore have a large response. As predicted, the CD spectra of peptide **7** displayed increased helical character compared to peptide **1**, indicated by the more intense minimum at 222 nm (**Figure 26**). Also notable is the ratio of the two minima which is closer to unity for peptide **7**, indicative of a larger helical population.
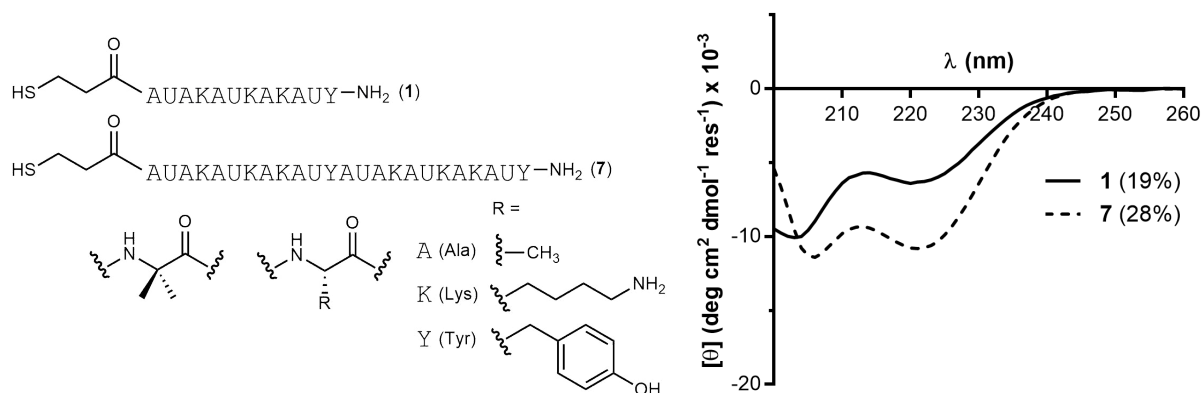
Figure 26. Peptides **1** and **7** and the CD scan of each (50 μM in 10 mM phosphate buffer pH 7.2). Estimated helical population for each peptide is indicated in parentheses.

The latter property, polarizability, was not as straightforward to modulate. Since prior computational studies on π-conjugated helicenes yielded large piezoelectric responses, we wanted to test a molecule that incorporated a fundamental feature that our peptide systems were lacking when compared to helicenes— backbone conjugation. Therefore, we chose an abiotic quinoline oligoamide helix first introduced by Huc.[124-125] We hypothesized that the presence of a conjugated backbone, which creates enhanced polarizability, will increase piezo response in comparison to the α-peptides, which have minimal backbone delocalization. The rationale for this hypothesis is that increasing polarizability increased the computationally predicted piezo response in helicene-type molecules.[63]

The synthesis of Fmoc-quinoline monomers, adapted from a literature approach,[124,126] gave two building blocks— one with a hydrophobic, all carbon side chain similar to leucine and one with a hydrophilic, basic side chain similar to lysine. These monomers were applied in solid phase synthesis to make the desired oligoquinoline via acid chloride activation.[127] It was determined that common coupling agents, such as HCTU, HATU, PyAOP, PyBrOP, DAST, and TFFH, did not promote the coupling of two oligoquinolines, presumably due to the poor nucleophilicity of the aniline-like amine.[126] Using Ghosez's reagent, an acid chloride was formed, creating a strong

enough electrophile to allow the couplings to proceed. A 5-mer oligoquinoline foldamer (**8**) which alternates monomers (Leu-type, Lys-type, Leu-type, etc.) and is capped with mercaptopropanoic acid to provide a free thiol for SAM formation on gold was obtained (**Figure 27A**). Based on prior structural and folding studies performed by the Huc lab, we expected oligomer **8** to be folded in a very rigid helical fashion, due to a stable three-centered backbone hydrogen bonding arrangement (**Figure 27B**), and have 2.5 monomer units per turn (**Figure 27C**).[124,128]
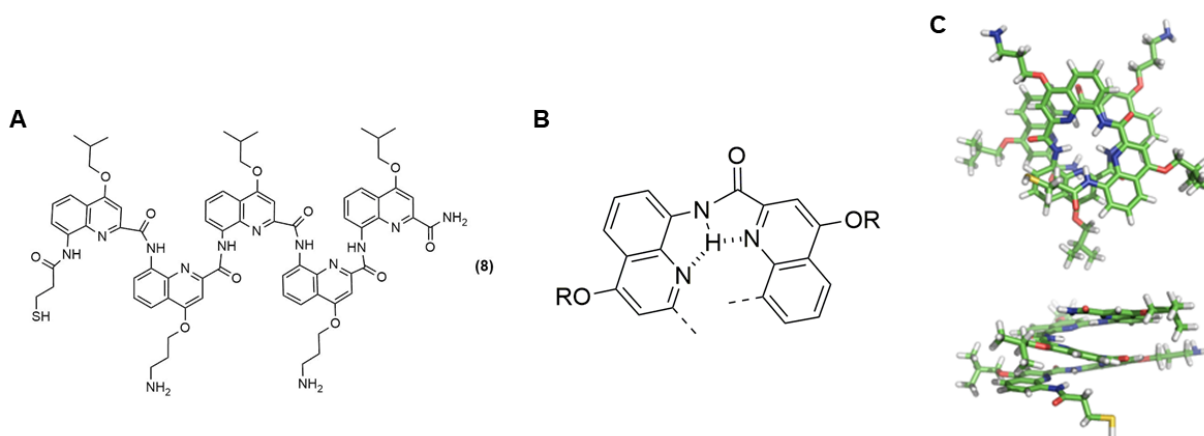
Figure 27. (A) Linear structure of oligoquinoline 8. (B) Predicted 3-center hydrogen bonding arrangement. (C) Predicted folding based on a published crystal structure.[124, 129]

Confirming the helical structure of **8** is not possible by CD because the molecule is achiral. Thus, the folding was probed via ^{1}H NMR and comparison to previous NMR studies by Dolain et. al. on related quinoline oligomers.[128] NMR studies suggest the presence of the desired hydrogen bonding pattern, which provides evidence for helical folding in solution. In the putative helix, the backbone amide protons H_b-H_e should engage in a three-centered hydrogen bonding pattern with the quinoline nitrogen, resulting in deshielding. In contrast, amide proton H_a is unable to form this type of hydrogen bonding arrangement, which should cause it to appear further upfield. The position of amide resonances in the ^{1}H NMR is consistent with the expected helical fold — four downfield peaks (11.5-12 ppm) and one upfield peak (~9 ppm) (**Figure 28**). Since the foldamer is

achiral, it is expected that a racemic mixture of right and left-handed helical folds is present in solution. The handedness of the fold is not expected to have an impact on piezo-response.
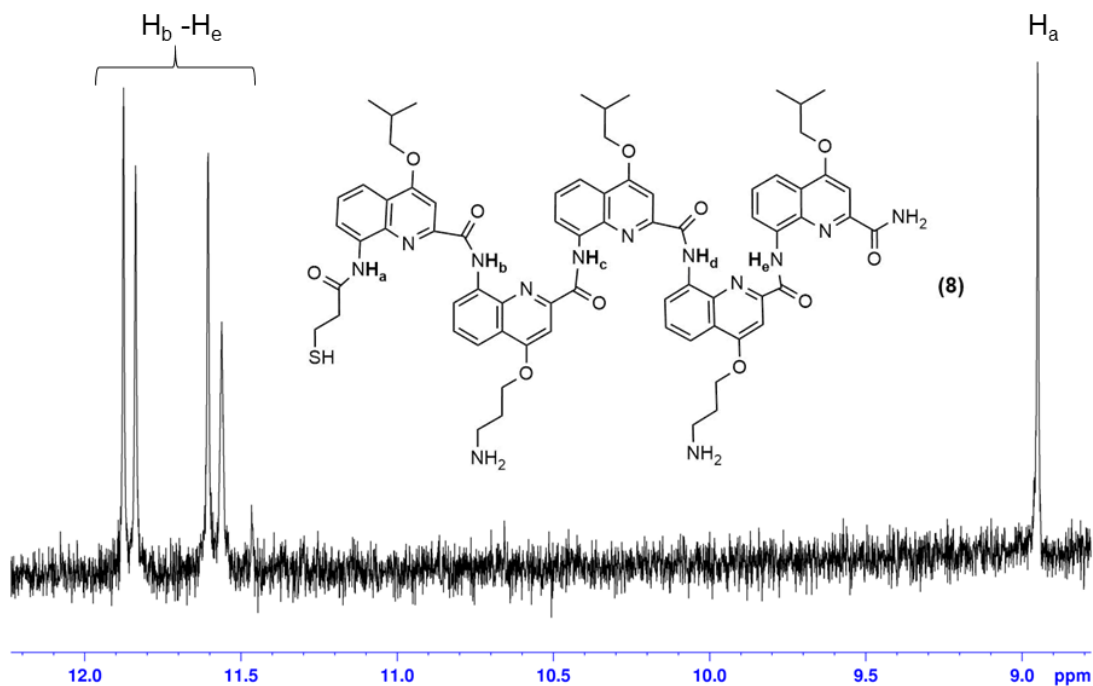
Figure 28. Displays the backbone amide hydrogen signals as they appear for **8** in the ^{1}H NMR (CD$_3$OH with 0.2 mM DSS).

Piezo response of self-assembled monolayers of **7** and **8** on gold was determined using the DART-PFM AC voltage sweep method described above and compared to the responses of peptides **1-3** (**Figures 29 and 30**). Like peptides **1-3**, voltage-dependent increases in peak width and standard deviation were observed for both SAMs.
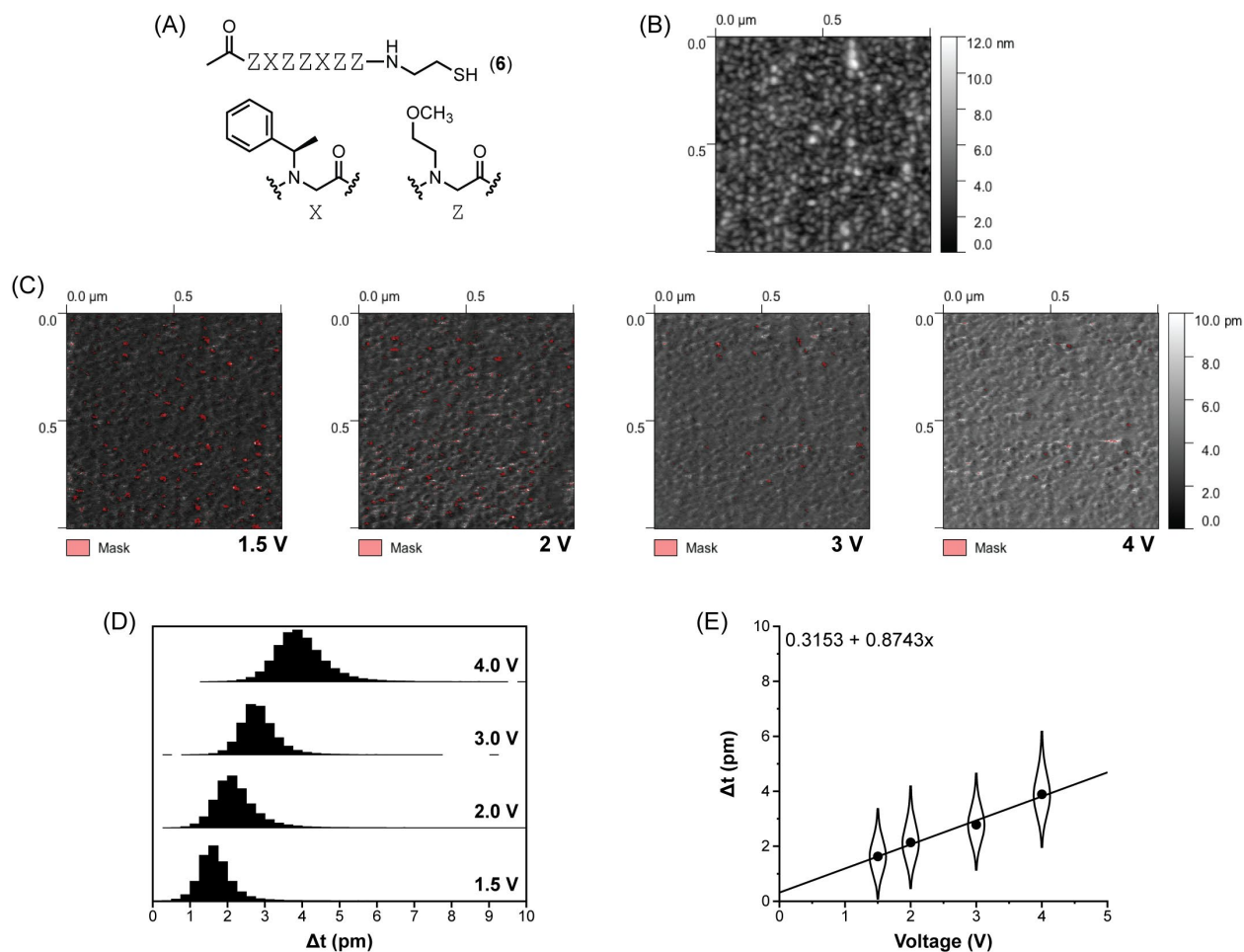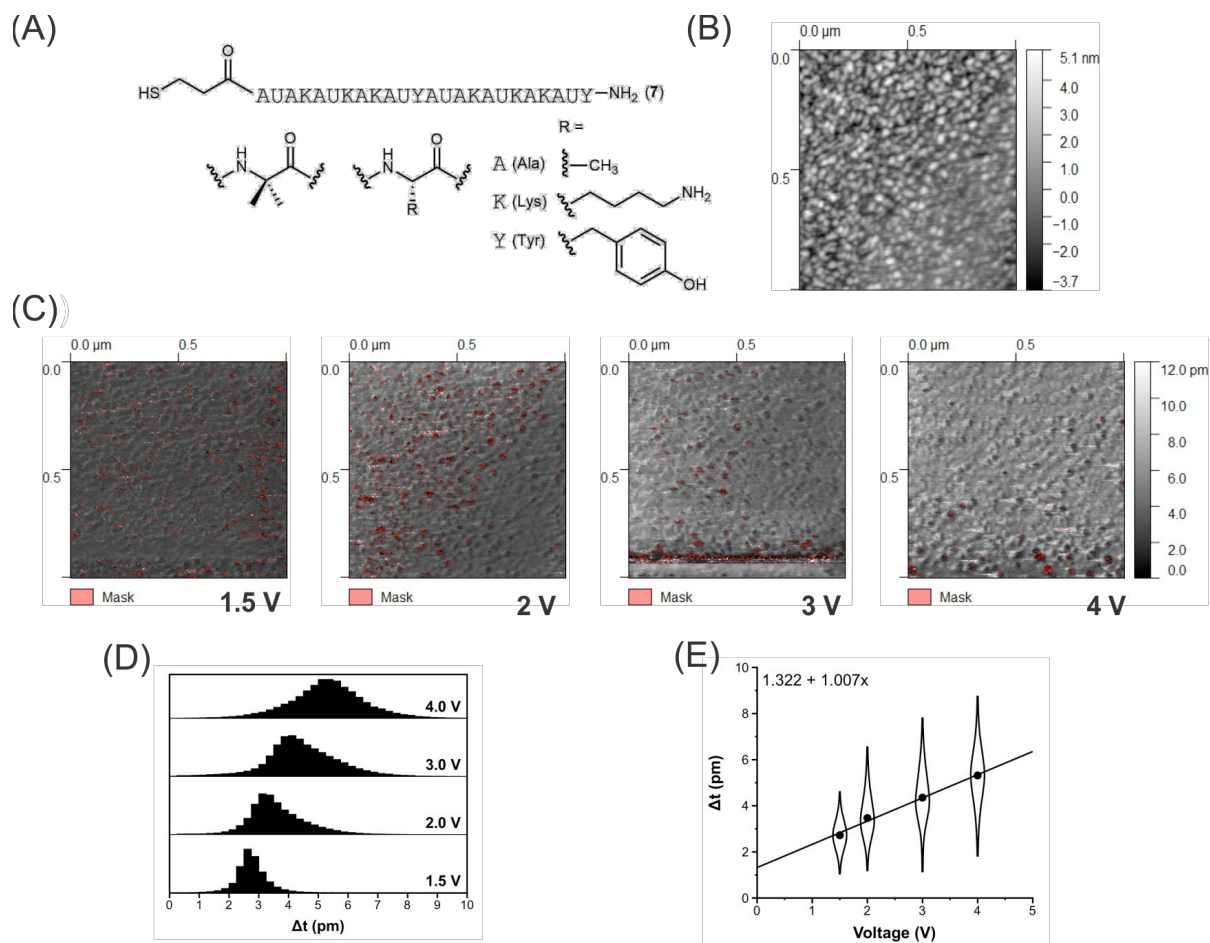
Figure 29. Representative raw DART PFM data for analysis of a self-assembled monolayer of peptide **7** on gold. (A) Chemical structure of peptide **7**. (B) Height image from DART-PFM measurement at an applied voltage of 2.0 V. (C) Images depicting q-corrected DART amplitude (Δt) at the indicated applied voltage. (D) Histogram analysis of the images shown in panel (C). (E) Linear regression of the histograms in panel (D) vs applied voltage; equation for the best-fit line is shown, where d_{33} is the slope.
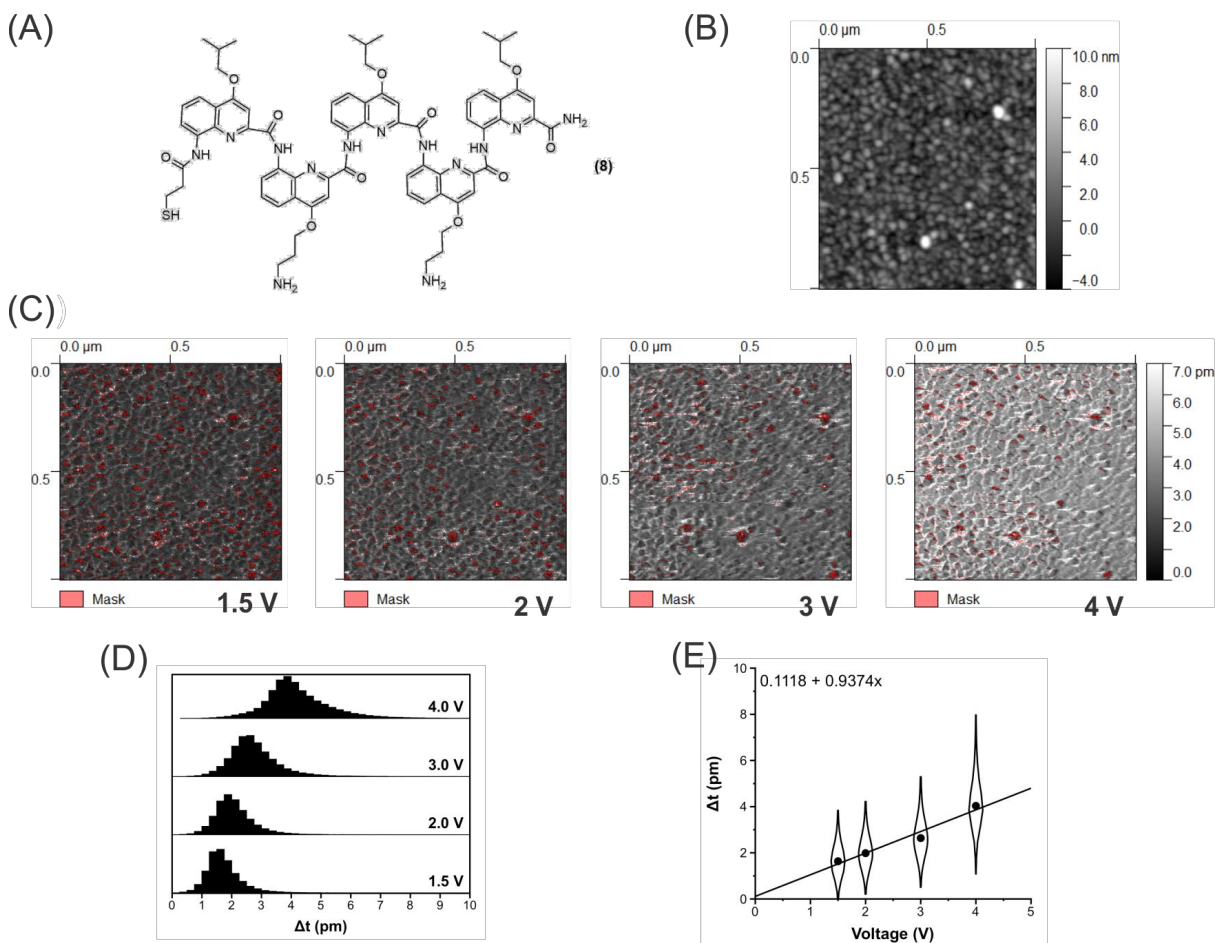
Figure 30. Representative raw DART PFM data for analysis of a self-assembled monolayer of foldamer **8** on gold. (A) Chemical structure of foldamer **8**. (B) Height image from DART-PFM measurement at an applied voltage of 2.0 V. (C) Images depicting q-corrected DART amplitude (Δt) at the indicated applied voltage. (D) Histogram analysis of the images shown in panel (C). (E) Linear regression of the histograms in panel (D) vs applied voltage; equation for the best-fit line is shown, where d_{33} is the slope.

Somewhat surprisingly, neither SAM out-performed peptides **1-3** (**Figure 31**). Instead the response was on par with that of peptoids **4-6** and **DDT**. Upon further consideration, the increased length of peptide **7** relative to its' helicity could be a drawback. While a longer peptide chain does have a larger absolute molecular dipole moment, piezo response is derived from the relative geometric deformation over the entire length of the molecule. In other words, a larger molecule must deform more to achieve the same piezo response as a small molecule. While the length of

49

peptide **7** doubled, the helical fraction only increased about 10%. Therefore, one possibility is that peptide **7** cannot geometrically deform enough to overcome its increased length.
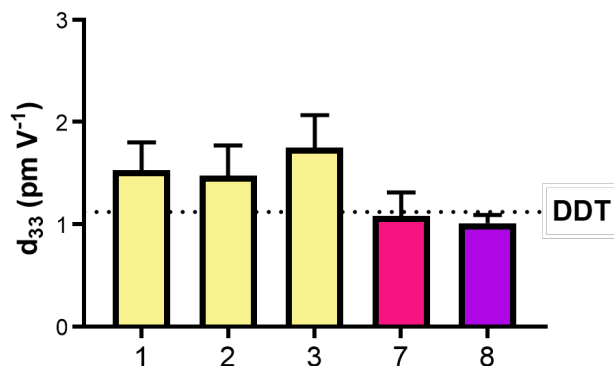
Figure 31. Piezo response represented by experimentally determined d_{33} values from multiple independent experiments with peptides **1-3**, peptide **7**, and foldamer **8**. Error bars are the SEM of 4-8 independent experiments.

Foldamer **8** which has a fully conjugated backbone, also displayed lower piezo response to peptides **1-3**. Oligomer **8** has been shown to be extremely stable in a large range of solvents and significantly more stable than Aib containing helical peptides.[130] Although polarizability has increased, the rigid helical conformation may be hindering electromechanical response. To tip the balance towards a more flexible structure, a flexible monomer could be introduced into the backbone to disrupt quinoline stacking,[131] making the chain less rigid and more amenable to conformational deformation under an applied field (**Figure 32**).
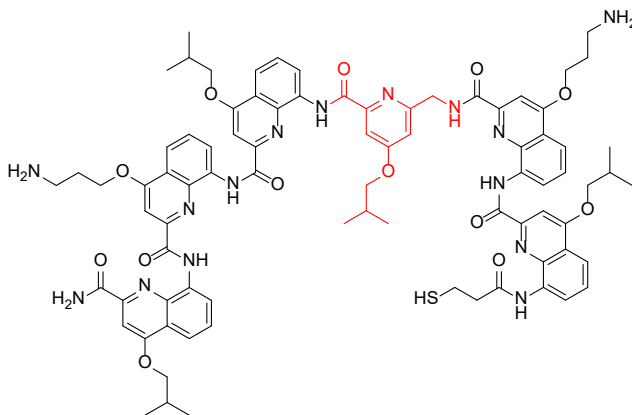
Figure 32. Proposed structure of a more flexible oligoquinoline foldamer by insertion of the monomer in red.

50

2.4 Improvements to DART-PFM Methodology

A significant challenge in the above described studies was accurately measuring the piezo response of the soft, flexible materials of interest. For all the molecules tested, we used an AC voltage sweep method which considers the responses of a multitude of various peptide conformations and surface packing arrangements. The AC voltage sweep method, while more robust and reproducible than typical single-point measurements, still requires the averaging of multiple measurements of independently prepared samples over several days with different tips. We recognized this time and material intensive methodology still has potential for improvement. Also hampering our measurements are unaccounted-for electrostatic effects arising from interactions between the tip and the surface. The electrostatic component was difficult to account for in our AC voltage sweep methodology. Operating near the noise floor of the instrument made collecting data as well as quantifying small differences in response challenging. Finally, maintaining the contact resonance frequency throughout the measurement, required for the DART-PFM method, was problematic at low tune frequency signals.

To improve our measurements further, a new DART-PFM methodology that entails the use of a soft lever, coupled with the quantification of the electrostatic component of tip response was developed by my collaborator.[132] In all prior measurements, we chose to use a high spring constant cantilever (k_1 = 2.8 N/m), which has been demonstrated as a means to minimize electrostatic effects for ceramic materials.[133] However, our organic monolayers are very different from typical piezoactive ceramics. The use of soft, low spring constant levers prevents the deformation of soft organic monolayers and increases the electrostatic component of the response. This leads to 1) enhancement of the contact resonance signal making it easier to track via DART-

PFM feedback mechanisms and 2) amplitudes above the noise floor of the instrument that can be more accurately measured.
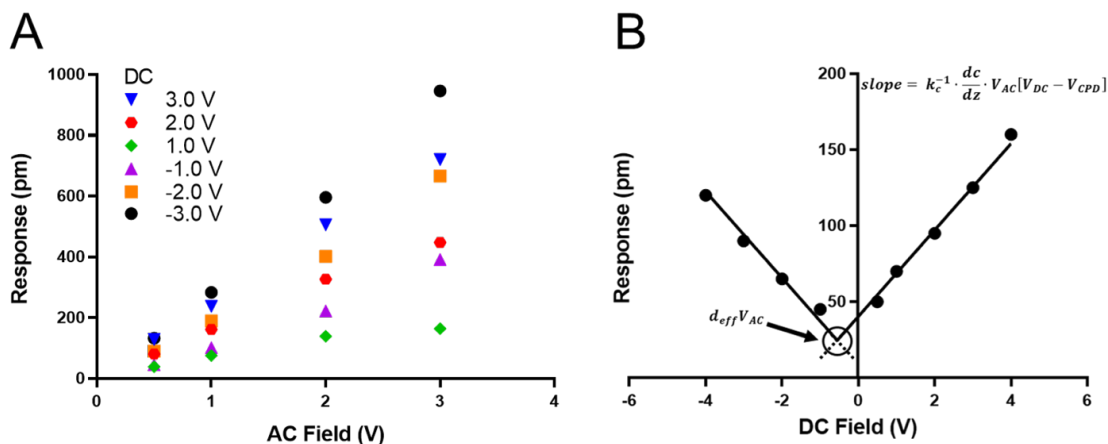
Figure 33. (A) Prior AC voltage sweep methodology for determination of piezo response using DART-PFM by varying V_{AC}. The slope of the trend line should reflect the d_{eff} piezo response (pm/V). (B) Suggested V_{DC} sweep technique to determine the piezo response in soft-organic piezo materials. The crossing point reflects the d_{eff} piezo response and the slope reflects the electrostatic contribution of the material. Image reproduced with permission from ref. 132.

To quantitatively separate the electrostatic component from the piezo response, a DC field sweep is performed while applying a constant AC voltage (**Figure 33**). The intersection point, where response is minimized, represents the piezo response as $d_{eff} \cdot V_{AC}$. By accurately compensating for the electrostatic component, the true d_{eff} of the material can be established. Rewardingly, application of this methodology to a subset of sequences described earlier in the chapter further confirmed our findings regarding the increased piezo response of peptide over peptoid and DDT monolayers (**Table 2**). Also significant is the sign of the piezo response, which was unable to be resolved using prior methodology. Both the peptide and peptoid SAM tested gave a negative d_{33} indicating that these materials compress under an applied field. This negative piezo response contrasts piezo ceramics such as ZnO or PZT, but is analogous to responses observed in

PVDF and a variety of other piezoelectric materials.[134-135] For these materials, a negative piezoelectric response is thought to arise from the electrostrictive response and strain of the material.[134] It is our hope that this improved, higher accuracy methodology will make future studies of organic and biomaterials more efficient and reproducible.

Table 2. Calculated d_{33} as a function of applied DC voltage at a constant V_{AC} of 3.0 V using 0.09 N/m k_l levers. Table adapted with permission from ref. 132.

Material	d_{33} (pm/V)
Quartz	1.68
DDT	0.100
Peptide 1	-6.42
Peptoid 5	-1.35

2.5 Summary

The results of Chapter 2 provide insights into the structural parameters affecting electromechanical response and suggest that peptide-based materials exhibiting piezo response have regions of highly aligned flexible backbones. Short, flexible peptides gave responses that were larger in magnitude than structurally rigid molecules, such as peptoids or an oligoquinoline foldamer. Structural heterogeneity in the peptide conformational ensemble observed at the surface precludes us from saying whether a particular subpopulation of folded states in the monolayer contributes disproportionately to the observed apparent d_{33}. This open question is an important area for future study. Understanding the factors that influence conformational preferences of surface-bound peptides and exerting control over these preferences is central to answering this

53

question and will be explored further in Chapter 3. In conclusion, the results reported here demonstrate the promise of combining systematic synthesis guided by computational design and DART-PFM monolayer characterization for SAMs of peptides and related oligomers as a means to unlock new avenues to highly responsive piezomaterials.

2.6 Experimental

2.6.1 General Information

All Fmoc α-amino acids and resins used for solid phase synthesis were purchased from Novabiochem. All other starting materials, solvents, and reagents were purchased from Sigma-Aldrich and used without further purification. Reverse phase HPLC was carried out using Phenomenex Luna C_{18} columns. Products were eluted using gradients between 0.1% TFA in water [solvent A] and 0.1% TFA in acetonitrile [solvent B], monitored by UV detection at 220 nm and 280 nm. MALDI-TOF MS experiments were performed on a Voyager DE Pro (Applied Biosystems) or an ultrafleXtreme (Bruker) using α-cyano-4-hydroxy cinnamic acid as the ionization matrix.

2.6.2 Peptide Synthesis

Peptides **1-3,** and **7** were synthesized by microwave-assisted Fmoc solid phase methods on a CEM MARS 5 microwave using NovaPEG rink amide resin (0.05 mmol scale). Resin was swelled in DMF for 15 min prior to the first coupling reaction. For a typical cycle, a 0.1 M solution

of HCTU in NMP (4 equiv relative to resin, 2 mL, 0.20 mmol) was added to Fmoc-protected amino acid (4 equiv, 0.20 mmol), followed by DIEA (6 equiv, 0.30 mmol). After a 2 min preactivation, the solution was transferred to resin, and the mixture heated to 90 °C over 1.5 min, followed by a 2 min hold at that temperature. Fmoc deprotection was carried out by treatment with 20% 4-methylpiperidine in DMF (4 mL), and the mixture was heated to 90 °C over 2 min, followed by a 2 min hold at that temperature. The resin was washed 3 times with DMF after each coupling and deprotection cycle. For Aib residues and those coupled to it, PyAOP (4 equiv, 0.20 mmol) was used in place of HCTU. The N-terminus of each peptide was capped with S-trityl-3-mercaptopropionic acid using the standard HCTU coupling described above. After the final coupling, the resin was washed 3 times each with DMF, DCM, and MeOH, and the resin was dried under vacuum for at least 20 min. Peptides were cleaved from resin by treatment with a solution of TFA/EDT/H_2O/TIS (92.5%/3%/3%/1.5% by volume) for 3 hours followed by precipitation in cold ether. The pellets were collected by centrifugation and re-dissolved in 90:10 solvent A / solvent B for purification by preparative HPLC. The identity and purity of final products were confirmed by analytical HPLC (**Figure 34**) and MALDI-TOF MS (**Table 3**). Peptide stock solution concentrations were quantified by UV spectroscopy (Hewlett Packard 8452A Diode Array Spectrometer, ε_{276} = 1450 cm^{-1} M^{-1} from the single Tyr in each sequence).

Table 3. MALDI-TOF MS data for peptides **1-3**, peptoids **4-6**, peptide **7** and foldamer **8**.

#	m/z (monoisotopic)	
	Calculated	**Observed**
1	1262.7[a]	1263.7
2	1220.7[a]	1221.4
3	1178.6[a]	1179.5
4	1269.6[b]	1269.5
5	1131.6[b]	1131.8
6	1039.5[b]	1039.6
7	2420.4[a]	2420.9
8	1317.5[a]	1318.7

[a] $[M+H]^+$ ion; [b] $[M+Na]^+$ ion
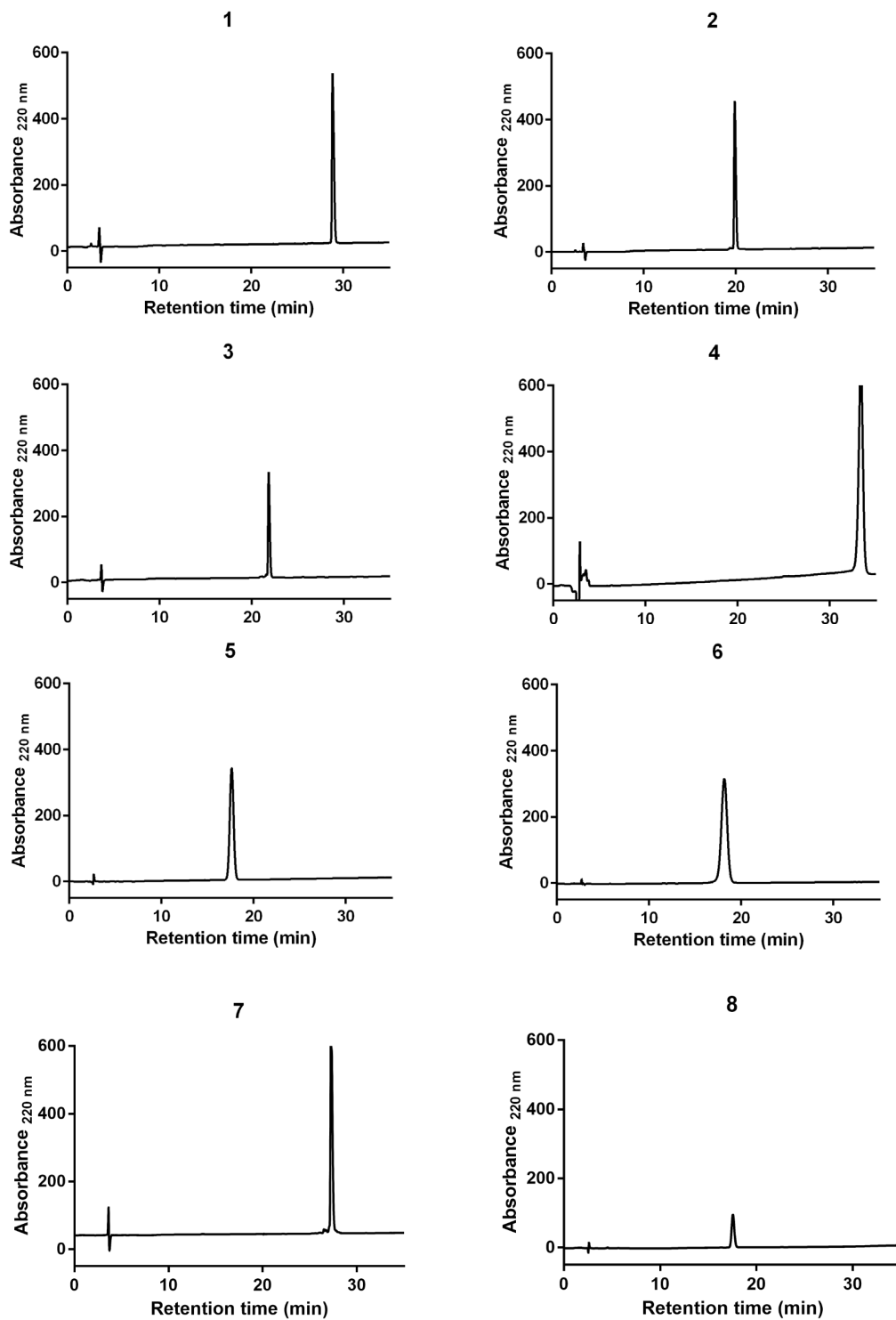
Figure 34. Analytical HPLC chromatograms of purified peptides **1-3**, peptoids **4-6**, peptide **7**, and foldamer **8**.

2.6.3 Peptoid Synthesis

Peptoids **4-6** were synthesized using a microwave-assisted submonomer solid phase approach on a CEM MARS 5 microwave using cysteamine 2-chlorotrityl resin (41.4 mg, 0.06 mmol). Resin was swelled in DCM for 30 min, then washed with DMF prior to the synthesis. In a typical cycle, a solution of 1.2 M bromoacetic acid in dry DMF (1.0 mL, 1.2 mmol) was added to resin, followed by DIC (188 µL, 1.2 mmol). The reaction was heated to 35 °C over 2 min, followed by a 2 min hold at that temperature. The resin was washed three times with DMF, followed by addition of a 1.5 M solution of primary amine (R-(+)-α-methylbenzylamine or 2-methoxyethylamine) in NMP (1.6 mL, 2.4 mmol). The mixture was then heated to 90 °C over 2 min, followed by a 2 min hold at that temperature. The resin was washed again with DMF (3x) prior to the next cycle. The N-terminus of each peptoid was capped by treatment of resin with a solution of DMF (800 µl), DIEA (200 µl), and acetic anhydride (100 µl) and stirring at ambient temperature for 20 min. The resin was then washed 3 times each with DMF, DCM, and MeOH, and dried under vacuum for at least 20 min. Each peptoid was cleaved from resin by treatment with a mixture of TFA/H_2O/TIS (95%:2.5%:2.5% by volume) for 30 min. The cleaved peptoid solution was diluted in H_2O, lyophilized, and re-dissolved in 50:50 solvent A / solvent B for purification by preparative HPLC. The identity and purity of final products were confirmed by analytical HPLC (**Figure 34**) and MALDI-TOF MS (**Table 3**). Peptoid stock concentrations were determined by weight followed by dilution to a desired concentration.

2.6.4 Quinoline Monomer Synthesis
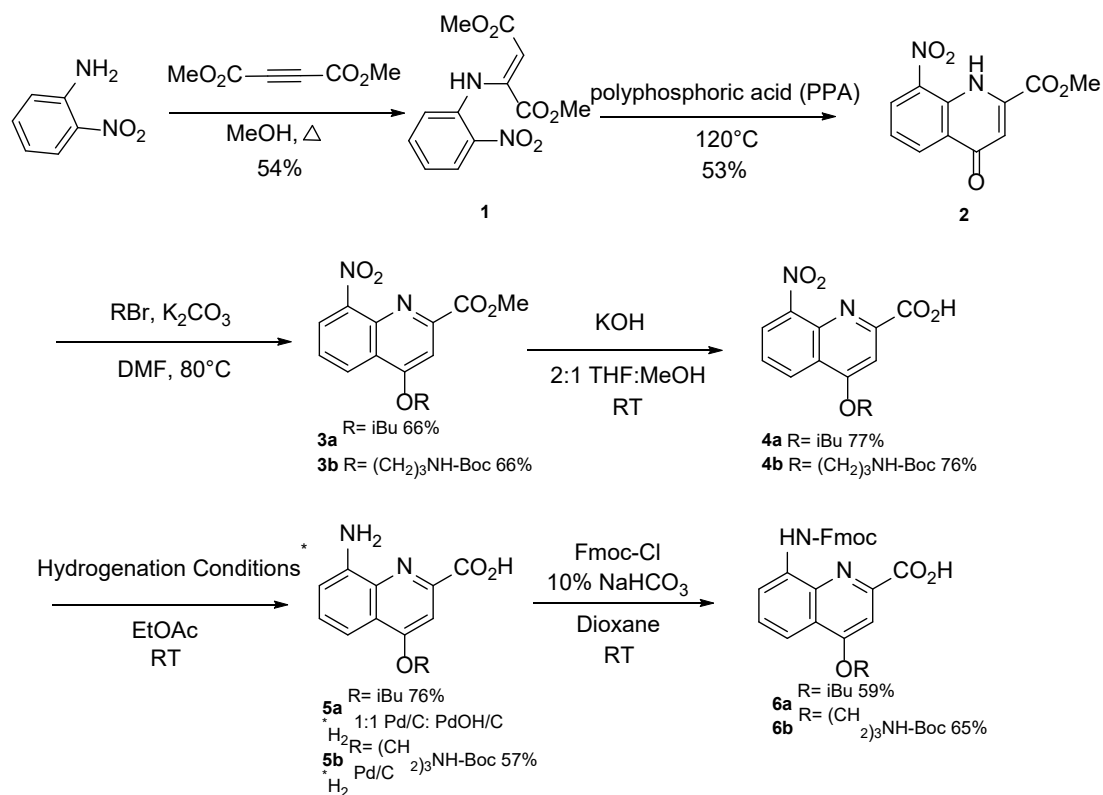
Figure 35. Synthesis of Fmoc-protected quinoline monomers, similar to the route described by the Huc lab.[124, 126]
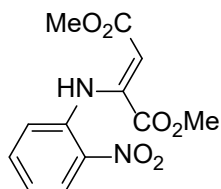
Synthesis of dimethyl 2-((2-nitrophenyl)amino)fumarate (1)

Prepared by a literature protocol.[136] To a solution of 2-nitroaniline (13.49 g, 97.66 mmol) dissolved in methanol (140 ml), dimethyl but-2-ynedioate (12.00 ml, 97.66 mmol) was added. The solution was stirred at 65°C overnight. The resulting bright yellow precipitate was collected via filtration, washed with cold methanol, and dried to yield product (14.73 g, 54% yield). ^{1}H NMR spectrum matched literature values.[136] ^{1}H NMR (300MHz, CDCl$_3$) δ3.74 (3H, s), 3.81 (3H, s),

5.84(1H, s), 6.76 (1H, d, J= 8.1), 7.08 (1H, td, J= 1.2, 8.4), 7.46 (1H, td, J= 1.5, 8.4), 8.14 (1H, dd, J= 1.5, 8.4), 11.10 (1H, s).
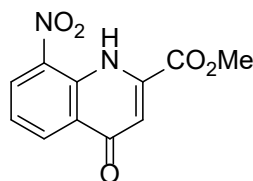
Synthesis of methyl 8-nitro-4-oxo-1,4-dihydroquinoline-2-carboxylate (2)

Prepared by a literature protocol.[136] Polyphosphoric acid (67.6 g) was heated to 120°C before dimethyl 2-((2-nitrophenyl)amino)fumarate **1** (11.29 g, 40.27 mmol) was carefully added. The solution was allowed to stir for four hours before cautiously pouring into a saturated solution of sodium carbonate. The brown precipitate was removed by filtration and dried to yield the product (5.26 g, 53% yield). ^{1}H NMR spectrum matched literature values.[136] ^{1}H NMR (300MHz, CDCl$_3$) δ4.08 (3H, s), 7.07 (1H, s), 7.48 (1H, t, J= 8.1), 8.73 (2H, t, J= 7.2), 11.78 (1H, s).
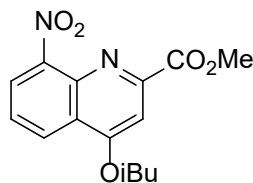
Synthesis of methyl 4-isobutoxy-8-nitroquinoline-2-carboxylate (3a)

Prepared by a literature protocol.[124] Isobutyl bromide (4.60 ml, 42.39 mmol) was added to a solution of methyl 8-nitro-4-oxo-1,4-dihydroquinoline-2-carboxylate (5.26 g, 21.19 mmol) and potassium carbonate (5.86 g, 42.39 mmol) in dry dimethylformamide (127 ml) under nitrogen. The solution was stirred overnight at 80°C before quenching with water and extracting with dichloromethane (3x 20 ml). The combined organic layers were washed with saturated sodium chloride and saturated ammonium chloride and dried over sodium sulfate. The remaining dimethylformamide was removed by forming an azeotrope with toluene and the product was

purified by recrystallization from cold methanol (4.25 g, 66% yield). ^{1}H NMR spectrum matched literature values.[124] ^{1}H NMR (300MHz, CDCl$_3$) δ1.15 (6H, d, J= 6.6), 2.31 (1H, m, J= 6.9), 4.04 (3H, s), 4.09 (2H, d, J= 6.6), 7.65 (2H, m), 8.11 (1H, dd, J= 1.5, 7.8), 8.48 (1H, dd, J= 1.2, 8.4)
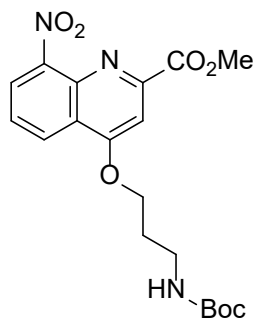
Synthesis of methyl 4-(3-((tert-butoxycarbonyl)amino)propoxy)-8-nitroquinoline-2-carboxylate (3b)

Protocol adapted from literature.[126] Tert-butyl (3-bromopropyl)carbamate (10.00 g, 42.03 mmol) was added to a solution of methyl 8-nitro-4-oxo-1,4-dihydroquinoline-2-carboxylate (5.23 g, 21.01 mmol) and potassium carbonate (5.80 g, 42.00 mmol) in dry dimethylformamide (125 ml) under nitrogen. The solution was stirred overnight at 80°C before quenching with water and extracting with ethyl acetate (3x 20 ml). The combined organic layers were washed with saturated sodium chloride and saturated ammonium chloride and dried over sodium sulfate. The remaining dimethylformamide was removed by forming an azeotrope with toluene to give a brown solid (5.63 g, 66% yield). ^{1}H NMR spectrum matched literature values.[126] ^{1}H NMR (300MHz, CDCl$_3$) δ1.43 (9H, s), 2.19 (2H, m, J= 6.3), 3.43 (2H, q, J= 6.6), 4.04 (3H, s), 4.39 (2H, t, J= 6.0), 4.71 (1H, s), 7.65 (2H, m), 8.11 (1H, dd, J= 1.2, 7.5), 8.46 (1H, dd, J= 1.2, 8.4).
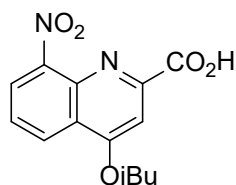
Synthesis of 4-isobutoxy-8-nitroquinoline-2-carboxylic acid (4a)

Prepared by a literature protocol.[124] **3a** (2.53 g, 8.30 mmol) was dissolved in tetrahydrofuran (200 ml) and methanol (100 ml). Crushed potassium hydroxide (1.16 g, 20.76 mmol) was added to the mixture, which was stirred at ambient temperature overnight. The solution was neutralized with acetic acid to ~pH 2. The aqueous layer was washed with dichloromethane (3x50ml) and the combined organic layers were washed with water and saturated sodium chloride, and then dried over magnesium sulfide. The solvent was evaporated to give a brown solid (1.86 g, 77% yield). ^{1}H NMR spectrum matched literature values.[124] ^{1}H NMR (300MHz, CDCl$_3$) δ1.16 (6H, d, J= 6.9), 2.33, (1H, m, J= 6.9), 4.14, (1H, d, J= 6.3), 7.73, (2H, m), 8.23 (1H, dd, J= 1.5, 7.5), 8.54 (1H, dd, J= 1.2, 8.4)
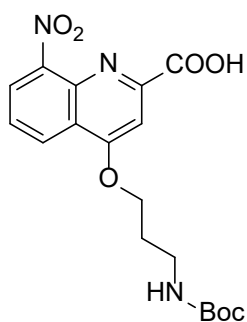
Synthesis of 4-(3-((tert-butoxycarbonyl)amino)propoxy)-8-nitroquinoline-2-carboxylic acid (4b)

Prepared by a literature protocol.[126] Carried out as described for **4a** starting from **3b** (1.00 g, 2.47 mmol) to yield the product as a yellow solid (0.7341 g, 76% yield). ^{1}H NMR spectrum matched literature values.[126] ^{1}H NMR (300MHz, CDCl$_3$) δ1.43 (9H, s), 2.21 (2H, m, 6.6), 3.43

(2H, q, *J*= 6.0), 4.44 (2H, t, *J*= 6.0), 4.71 (1H, s), 7.72 (2H, m), 8.23 (1H, d, *J*= 7.2), 8.54 (1H, d, *J*= 8.1).
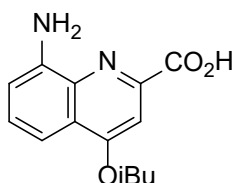
Synthesis of 8-amino-4-isobutoxyquinoline-2-carboxylic acid (5a)

Prepared by a literature protocol.[124] A mixture of palladium on carbon (172 mg, 1.62 mmol) and palladium hydroxide on carbon (172 mg, 1.22 mmol) catalysts were added to a solution of **4a** (1.86 g, 7.15 mmol) in ethyl acetate (60 ml). The reaction was stirred at ambient temperature under a hydrogen atmosphere overnight. The reaction was filtered through celite and washed with ethyl acetate and methanol. A dark brown solid product was isolated after solvent evaporation (1.26 g, 76% yield). ^{1}H NMR spectrum matched literature values.[124] ^{1}H NMR (300MHz, DMSO) δ1.07 (6H, d, *J*= 6.6), 2.18 (1H, m, *J*= 6.6), 4.08 (2H, d, *J*= 6.6), 6.49 (2H, s), 6.87 (1H, dd, *J*= 1.2, 7.5), 7.24 (1H, dd, *J*= 1.2, 8.1), 7.36 (1H, t, *J*= 8.1), 7.45 (1H, s) MS (ESI) m/z calculated for $C_{14}H_{16}N_2O_3$ [M+H]$^+$ 261.1 Da, found 261.2 Da.
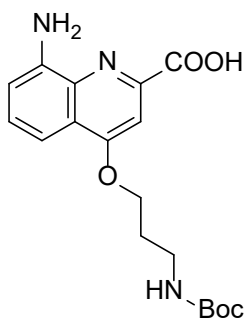
Synthesis of 8-amino-4-(3-((tert-butoxycarbonyl)amino)propoxy)63uinolone-2-carboxylic acid (5b)

Prepared by a literature protocol.[126] The same procedure to synthesize **5a** was followed starting from **4b** (1.94 g, 4.98 mmol) with the exception that only a single catalyst, Pd/C, was used.

The product was collected as a brown solid (1.01 g, 56 % yield). ^{1}H NMR spectrum matched literature values.[126] ^{1}H NMR (300MHz, CDCl$_3$) δ1.44 (9H, s), 2.17 (2H, m), 3.42 (2H, m), 4.35 (2H, t, J= 5.7), 4.76 (1H, s), 7.02 (1H, d, J= 6.9), 7.44 (1H, m), 7.58 (2H, m); MS (ESI) m/z calculated for C$_{18}$H$_{23}$N$_3$O$_5$ [M+H]$^+$ 362.1 Da, found 362.2 Da.
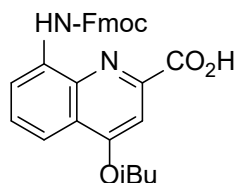
Synthesis of 8-(((((9H-fluoren-9-yl)methoxy)carbonyl)amino)-4-isobutoxyquinoline-2-carboxylic acid (6a)

Adapted from a literature protocol.[126] **5a** (0.259 g, 1.00 mmol) was dissolved in dioxane (15.6 ml) and a saturated sodium bicarbonate solution (15.7 ml). A solution of fluorenylmethyloxycarbonyl chloride (0.313 g, 1.20 mmol) dissolved in dioxane (5.0 ml) was added dropwise while the reaction stirred for one hour on ice. The reaction was stirred at ambient temperature overnight before the contents were poured into water (50 ml) and acidified to ~pH 2 with HCl (1M). The organic layer was extracted with dichloromethane (2x50 ml). The combined organic layers were washed with saturated sodium chloride and dried over sodium sulfate. Purification was achieved by dry loading the crude product onto silica gel with 20% ethyl acetate, 1% triethylamine in hexanes, then running 50% ethyl acetate in hexanes through the column. The product was eluted with 1% acetic acid in ethyl acetate. Acetic acid was removed through forming an azeotrope with heptane to give a yellow solid (0.281 g, 59% yield). ^{1}H NMR spectrum matched literature values.[126] ^{1}H NMR (300MHz, CDCl$_3$) δ1.10 (6H, d, J= 6.9), 2.26 (1H, m, J= 6.6), 4.04 (2H, d, J= 6.6), 4.38 (1H, t, J= 6.3), 4.63 (2H, d, J= 6.6), 7.35 (2H, td, J= 1.2, 7.5), 7.43 (2H, t, J=

7.5), 7.59 (1H, m), 7.67 (3H, m), 7.81 (2H, d, 7.5), 7.93 (1H, dd, J= 1.2, 8.7), 8.44 (1H, s), 8.68 (1H, s).
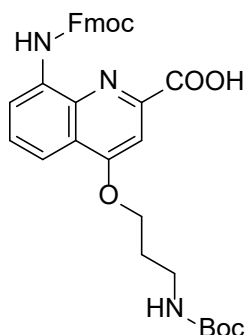
Synthesis of 8-(((((9H-fluoren-9-yl)methoxy)carbonyl)amino)-4-(3-((tert-butoxycarbonyl)amino)propoxy)65uinolone-2-carboxylic acid (6b)

Adapted from a literature protocol.[126] Carried out using the protocol for **6a**, starting from **5b** (1.01 g, 2.79 mmol) to yield the product, after purification, as a yellow solid (1.06 g, 65% yield). ^{1}H NMR spectrum matched literature values.[126] ^{1}H NMR (300MHz, CDCl$_3$) δ1.44 (9H, s), 2.15 (2H, m, J= 6.6), 3.13 (1H, q, J= 7.8), 3.42 (2H, q, J= 6.6), 4.36 (2H, t, J= 6.0), 4.62 (2H, d, J= 6.6), 4.74 (1H, s), 7.32 (2H, t, J= 7.2), 7.41 (2H, t, J= 7.2), 7.56 (1H, m), 7.65 (3H, d, J= 9.3), 7.79 (2H, d, J= 7.5), 7.88 (1H, d, J= 8.4), 8.69 (1H, s). MS (ESI) m/z calculated for C$_{33}$H$_{33}$N$_3$O$_7$ [M-H]$^-$ 582.2 Da, found 582.2 Da.
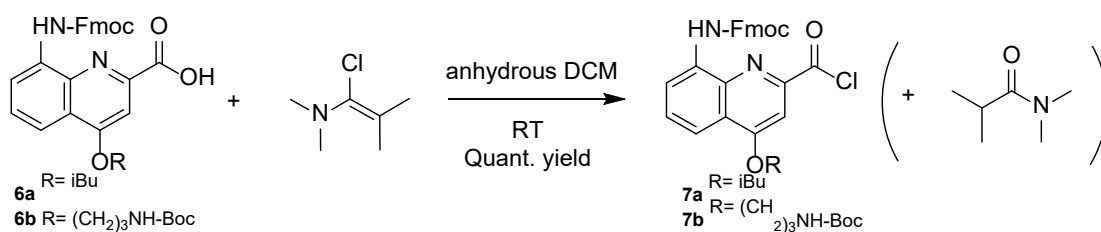
Figure 36. Acid chloride activation of quinoline monomers using Ghosez's reagent.
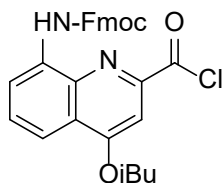
Monomer activation: Synthesis of (9H-fluoren-9-yl)methyl (2-(chlorocarbonyl)-4-isobutoxyquinolin-8-yl)carbamate (7a)

Prepared by a literature protocol.[126] 1-chloro-N,N,2-trimethylprop-1-en-1-amine (82.0 µl, 0.62 mmol) was added to a solution of **6a** (150.0 mg, 0.31 mmol) in anhydrous dichloromethane (4.5 ml) under nitrogen gas. The reaction was stirred under ambient temperature for two hours before the solvent was evaporated resulting in a yellow solid. The product was dried under high vac for at least 3 hours before use in solid phase synthesis to ensure dryness. Assumed quantitative yield. ^{1}H NMR spectrum matched literature values.[126] ^{1}H NMR (300MHz, CDCl₃) δ1.13 (6H, d, *J*= 6.6), 2.29 (1H, m, *J*= 7.2), 4.04 (2H, d, *J*= 6.6), 4.36 (1H, t, *J*= 7.2), 4.53 (2H, d, *J*= 7.2),7.34 (2H, td, *J*= 1.2, 7.5), 7.44 (3H, m, *J*= 6.6), 7.65 (1H, t, *J*= 8.1), 7.72 (2H, d, *J*= 7.5), 7.80 (2H, d, *J*= 7.2), 7.88 (1H, dd, *J*= 1.2, 8.4), 8.45 (1H, s), 9.32 (1H, s).
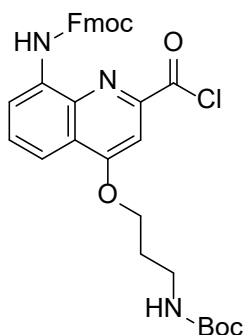
Synthesis of tert-butyl (3-((8-(((((9H-fluoren-9-yl)methoxy)carbonyl)amino)-2-(chlorocarbonyl)quinolin-4-yl)oxy)propyl)carbamate (7b)

Prepared by a literature protocol.[126] Carried out as described for **7a**, starting from **6b** (90 mg, 0.15 mmol). Assumed quantitative yield. ^{1}H NMR (300MHz, CDCl₃) δ1.44 (9H, s), 2.19 (2H,

m, *J*= 6.6), 3.13 (1H, q, *J*= 7.8), 3.42 (2H, q, *J*= 6.0), 4.36 (2H, t, *J*= 5.4), 4.54 (2H, d, *J*= 7.5),

4.74 (1H, s), 7.34 (2H, t, *J*= 8.4), 7.42 (2H, t, *J*= 6.6), 7.49 (1H, s), 7.65 (1H, t, *J*= 7.5), 7.71 (2H,

d, *J*= 7.2), 7.80 (2H, d, *J*= 7.5), 7.84 (1H, d, *J*= 7.5), 9.32 (1H, s).
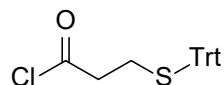
Synthesis of 3-(tritylthio)propanoyl chloride (8)

Adapted from a literature protocol.[126] Carried out as described for **7a**, starting from 3-(tritylthio)propanoic acid (36 mg, 0.10 mmol). Assumed quantitative yield. ^{1}H NMR (300MHz, CDCl$_3$) δ2.43 (2H, m, *J*= 6.6), 2.57 (2H, m, *J*= 5.7), 7.21 (9H, m), 7.35 (6H, d, *J*= 7.5).

2.6.5 Oligomer 8 Synthesis

Protocol adapted from literature.[127] Oligoquinoline foldamer **8** was synthesized on Rink amide MBHA resin (41.7 mg, 0.015 mmol) which was allowed to swell in DCM for 30 minutes. After swelling, the resin was washed with DMF (3x). The resin was deprotected using 20% 4-methylpiperidine in DMF (2 ml) for 2 minutes after a 2 minute ramp to 90°C. The resin was then washed with DMF (3x) and anhydrous THF (3x). The desired acid-chloride activated monomer (3 equivalents relative to resin loading) was dissolved in anhydrous THF (1 ml) just before use. A small amount of anhydrous THF (~0.3 mL) was added the resin, followed by anhydrous DIEA (6 equiv, 0.09 mmol). *The desired monomer was added to the resin after DIEA* (order of addition was found to be vital for high yielding couplings). Isobutoxy containing monomers were coupled for 5 min after a 5 min ramp to 50°C, while amino-propoxy containing monomers and the thiol capping group were coupled for 15 min after a 5 min ramp to 50°C. All monomers were double coupled (i.e. the coupling step was carried out twice before a deprotection step). After each

coupling step the resin was washed three times each with anhydrous THF and additionally three times with DMF after the second coupling. Deprotections were performed with 20% 4-methylpiperidine in DMF (2 ml) by stirring at room temperature for 10 min. The resin was washed three times with DMF, and the deprotection step was repeated two more times. After the third deprotection and washing step, the resin was additionally washed three times with anhydrous THF. Following the final coupling of **8**, the resin was washed three times each with DMF, DCM and 1:1 DCM:MeOH and dried under vacuum for at least 15 hours. The oligoquinoline was cleaved for 2 hours with a mixture of TFA (95%), H_2O (2.5%) and TIS (2.5%). The resin was washed with excess TFA once cleavage was complete and the excess TFA was evaporated before precipitation in cold ether. Centrifugation for 15 minutes resulted in a yellow pellet. The ether was carefully removed and the pellet was re-dissolved in HPLC solvents (50%A, 50%B) for purification (**Figure 34**).

2.6.6 Circular Dichroism (CD)

CD measurements were performed on an Olis DSM17 circular dichroism spectrophotometer. Scans were performed at 20 °C from 200-260 nm with 1 nm increments, a bandwidth of 2 nm, and a 5 sec integration time. Cells with a 2 mm path length were used. Peptide solutions (50 µM as determined by UV absorbance) were prepared in 10 mM phosphate buffer (pH 7.2). Peptoid solutions (50 µM as determined by accurate weighing) were prepared in acetonitrile (HPLC grade). Percent helical population was calculated using a previously described method[101] that uses the assumption that the population only consists of two states, helical and random coil, and that the contribution to ellipticity from the random coil population is negligible at 222 nm. Fraction helical population was estimated by dividing the observed ellipticity at 222

nm, $[\Theta_{obsH}]_{222}$, in deg cm^2 dmol^{-1} by the limiting value for ellipticity for a 100% helical backbone. The latter was calculated via the equation $[\Theta_H]_{222} = 43000(1-[x/n])$, where n is the number of residues and x is a factor that accounts for end effects, for which a value of 2.5 was used.

2.6.7 Self-Assembled Monolayer Formation

Gold-thiol self-assembled monolayers (SAMs) were prepared using 1.0 mM dodecanethiol in ethanol, 1.0 mM peptide in distilled water, or 1.0 mM peptoid in acetonitrile. These solvents were chosen due to solubility of the molecule being deposited and have no impact on the production of the monolayers. Substrates consisted of gold metal deposited on glass (Thermo Scientific BioGold substrates produced by Electron Microscopy Sciences). Prior to SAM formation, substrates were cleaned by washing with ethanol and water, followed by sonication for 10 min in the corresponding solvent used for deposition (ethanol for **DDT**, water for **1-3** and **7-8**, acetonitrile for **4-6**). After cleaning, the substrates were dried with compressed air or N$_2$ and submerged into the solution of thiol ligand for 24 h at room temperature. The substrates were then taken out of the solution, rinsed three times with the respective solvent, blown dry, covered with aluminum foil, and placed in a desiccator for at least 1 h prior to analysis. Samples not measured immediately were stored in a desiccator, protected from light exposure.

2.6.8 X-ray Photoelectron Spectroscopy (XPS)

XPS measurements were collected on a Thermo Scientific ESCALAB 250XI XPS spectrometer. Peptide, peptoid, and DDT monolayers were deposited on Thermo Scientific BioGold substrates produced by Electron Microscopy Sciences. A survey spectrum was collected

at a pass energy of 150 eV and a dwell time of 10 ms. Au_{4f} and N_{1s} were averaged over 50 scans with a pass energy of either 100 eV for peptides **1-3** or 150 eV for peptoids **4-6** and a dwell time of 50 ms. S_{2p} spectra were taken as an average of 100 scans with a pass energy of either 100 eV for peptides **1-3** or 150 eV for peptoids **4-6** and dwell time of 50 ms. Standard baseline subtraction, normalization, and peak fits were performed. The surface density and film thickness of each SAM was estimated using a previously published method,[2] where ratio of the sulfur and gold peak maxima, at 162 eV and 84 eV respectively, were averaged across three different spots on a single SAM to estimate the surface density. Similarly, the film thickness is estimated using the ratio of the carbon, at 284.8 eV, and gold peak maxima. The average peak ratio for a given SAM was compared to that of the measured DDT SAMs. DDT has a known packing density of 4.62×10^{14} molecules per cm^2 and a film thickness of 1.5 nm, which allows the surface density and film thickness of each monolayer to be estimated by comparison.

2.6.9 Atomic Force Microscopy (AFM) and Piezo Force Microscopy (PFM)

AFM and PFM measurements were performed using an Asylum Research MFP-3D SPM. PFM experiments were carried out using the dual-AC resonance tracing (DART-PFM) mode. Asyelec.01-R2 (Asylum Research) iridium-coated, conductive silicon probes were used for the characterization of the surface. These tips have a free-air resonance frequency of 70 kHz, but a contact resonance of ~280 kHz. They have a spring constant of 2.8 N/m. Multiple tip-sample AC voltages from 1.5 - 4.5 V were applied for each sample, as described below. The deflection was set to -0.30 and the humidity in the sample box maintained below 30%. If ambient relative humidity was above 30%, the instrument was flushed with dry nitrogen during the measurement. For each sample, a 1 μm x 1 μm area was scanned with a scan rate of 1.0 Hz. Topography,

piezoresponse amplitude, and phase images were recorded. The recorded amplitudes were q-corrected to take the tip-sample resonance amplification used by DART-PFM into account. This q-correction was performed using the default analyzing software. A histogram of the q-corrected amplitude scan was generated. The median value of the distribution was plotted versus the appropriate voltage. The slope from a linear regression of this plot for the same sample measured on the same day was used to determine a single d_{33} value for a given compound. Multiple independent experiments performed for different samples and days provided multiple d_{33} values for each compound. These values were averaged to generate the statistics reported in **Table 1**.

For the DC voltage sweep method, the same protocol was used with a few significant changes. Low spring constant TR400PB (TR: S and L), Asylum Research, gold-coated conductive silicon nitride probes were used. They have a 32.0 ± 14.5 and 10.0 ± 7 kHz free air resonance frequency, but a ~120 and 40 kHz contact resonance. The TR levers have a free air spring constant of 0.09 ± 0.12 and 0.02 ± 0.02 N/m respectively. DART experiments were conducted at multiple tip-sample AC, and DC biases ranging from |0-4| V. Deflection was set to -0.30 V with a tune z-voltage of ~15 V and a scan z-voltage of ~ -7.0 V to maximize signal and ensure stable contact between probe and sample during scanning.

2.6.10 Calculation of Dipole Moment for Model Helices

Gaussian 09 revision D.01[137] was used to perform geometry optimizations using density functional theory (DFT), with the dispersion-corrected ωB97X-D functional[138] and the 6-31G(d) basis set to optimize all computed structures. Initial geometries were generated using PyMol version 1.8.4[139] with idealized backbone dihedral angles for α-helix (peptide) or PPI (peptoid)

secondary structure. Computed dipole moments from DFT have been found to be highly accurate with errors in the 0.1-0.2 D range.[140]

2.6.11 Solution Fourier Transform Infrared Spectroscopy

Spectra were collected on a Bruker Vertex-70LS FTIR that was purged with N_2 gas for at least 30 minutes prior to taking measurements. A liquid cell with CaF_2 windows and a 50 μm spacer was assembled and this empty cell was used as the reference. The cell was thoroughly cleaned with methanol and dried with N_2 before each measurement. Peptide solutions (~ 5 mg/ml in D_2O) were measured with 1000 scans, a 3 mm aperture, and a resolution of 4 cm^{-1} collected over a range of 500-4000 cm^{-1}. Raw data for each sample were collected as a transmission spectrum, corrected by subtraction of a blank (D_2O) transmission spectrum, converted to absorption, and smoothed.

2.6.12 Polarization-Modulated Infrared Reflection Absorption Spectroscopy (PM-IRRAS)

PM-IRRAS spectra were collected on a Thermo Fisher Nicolet iS50 FTIR Spectrometer equipped with a liquid nitrogen cooled MCT-A detector. Gold-thiol self-assembled monolayers were prepared as described above. The interferogram was automatically aligned using the "align" function prior to collection. The physical sample alignment was found to be highly important for collection of high quality and reproducible spectra. Gold substrates were attached to a glass microscope slide using double-sided copper tape and the slide was aligned using the rotation, tilt, and mirror adjustment levers so that the interferogram intensity was maximized in "sum" mode (rough max of 5.0-6.5). (*NOTE:* This max value may be hard to reach until the box is fully purged

with nitrogen). The gain is chosen by looking at the "dual channel polarization modulation window"; the input gain should be maximized at 10 and the output gain (typically 1 or 2) was chosen by picking a gain value that maximizes channel B, without overtaking the maximum of channel A. PM-IRRAS spectra were collected with a 30 min acquisition time (3000 scans) and a resolution of 4 cm^{-1} at an incidence angle of 80°. The wavelength was centered at 1600 cm^{-1} to get good signal in the amide region. Atmospheric correction was applied to all spectra, followed by a manual baseline correction and smoothing.

3.0 Creation of Tailored Surfaces for Probing Peptide and Protein Surface Folding and Activity

Contributions:

This work was performed in collaboration with Nathaniel C. Miller, Geoffrey R. Hutchison, Alaina N. McDonnell, and Alexander Deiters and their specific contributions are as follows:

> *Nathaniel C. Miller fabricated the thin gold- on-silicon surfaces used for contact angle goniometry. Geoffrey R. Hutchison developed code to implement the arPLS baseline correction method for PM-IRRAS data sets. Alaina N. McDonnell carried out the expression of wild type and K39PK mutant BAP enzymes, performed solution-based activity assays [Figure 50 and 51A], and assisted with the development of the surface-bound BAP activity assay.*

The importance of peptide conformation to the electromechanical response of piezoactive synthetic oligopeptide self-assembled monolayers described in Chapter 2 inspired further study into the folding behavior of peptides bound to surfaces. In addition to tailoring oligomers at the molecular scale (i.e. changing the primary sequence) to alter conformational rigidity, controlling surface properties of the monolayer also provides an avenue for affecting oligomer conformation. An understanding of how surface properties influence peptide folding is of interest not only in the design of piezoelectrics, but also for a variety of bio-functionalized surface applications.[80, 141-142] Harnessing methodology to create tailored and tunable surfaces is the first step towards predictably altering biomolecule conformation via surface properties.

As discussed in Chapter 1, biomolecules can be introduced onto a gold surface via adsorption, self-assembly, or by covalent attachment methods. Adsorption and self-assembly methods are widely used due to their relative experimental simplicity, however, a significant downside to adsorption and self-assembly exists as there is minimal ability to control placement, spacing, or orientation of the molecules deposited. In some circumstances, this can lead to decreased stability or loss of activity. While self-assembly typically results in a well-packed monolayer,[17, 141] adsorption often results in surfaces with randomly oriented molecules, which are hard to predict or control.[143] Alternatively, covalent attachment provides more control over biomolecule incorporation at a surface.[42] One example is the ubiquitous click reaction that has been successfully used in the context of surface functionalization to attach DNA,[144] oligonucleotides,[145] proteins,[146] ferrocenes,[147-149] fullerenes,[150] and small peptides[151-154] to organic SAMs. In the context of small peptides, copper-catalyzed click chemistry has been used to covalently tether peptides to surfaces in a manner that induces helical structure by constraining the peptide with multiple triazole linkages resulting from reaction of the alkyne-containing peptide to an azide-terminated alkanethiol on a gold substrate.[154] The efficiency of the click reaction has been shown to be dependent on the alkanethiol SAM, particularly the terminal group's ability to interact with the peptide to either promote or impede reaction progress.[155] Although multiple studies have used click chemistry to attach peptides and other biomolecules to surfaces and analyzed the efficacy of this reaction in variety of contexts, it remains unclear how surface properties work in tandem to control surface bound conformation and orientation of covalently bound molecules.

New interactions not present in solution conditions, namely peptide-peptide interactions and peptide-surface interactions, must be taken into account when considering peptide environment on a surface.[156] To effectively alter peptide environment, these interactions can either

be disrupted or enhanced. In Chapter 3, we systematically alter three factors: peptide density, surface polarity, and the inherent folding propensity of the chosen biomolecule in a solvated context with the goal of altering biomolecule environment and creating surfaces with tunable properties (**Figure 37**).
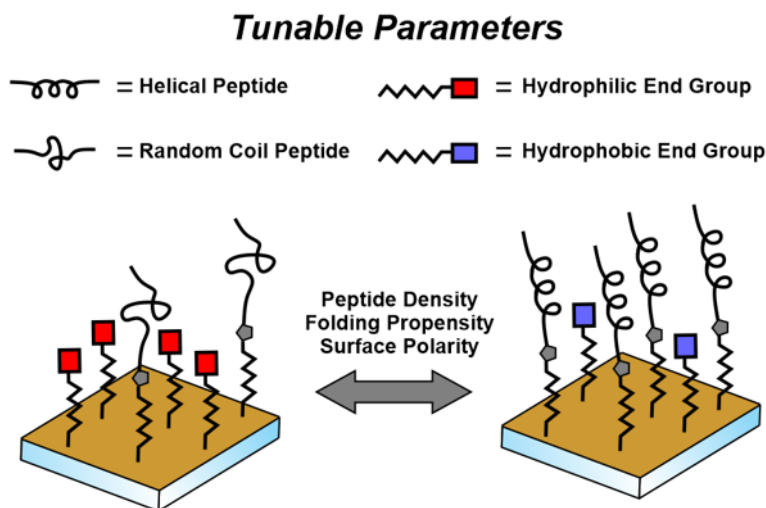
Figure 37. Scheme depicting the parameters under study at the surface, namely peptide density, solution folding propensity, and surface polarity.

A number of biomolecules, ranging in size and conformation, were selected for this study. First, we chose two small, simple peptides with the aim of demonstrating that we can effectively alter surface parameters and covalently incorporate a biomolecule onto these surfaces. Second, we incorporated a more rigid and structured coiled-coil fold into our surface designs. This system created a new challenge for surface incorporation that required the use of a synthetic linker for surface attachment. The final system was a large dimeric enzyme that we hypothesized would be highly sensitive to the specific properties of the surface to which it is bound.

3.1 Tailored Surface Design

Interchain interactions at a peptide-functionalized surface can be altered by changing peptide density and thereby interchain spacing. At high densities, peptides experience extensive interactions with neighboring molecules (e.g. electrostatic repulsions and sterically driven folding) which may alter folding behavior from that observed in a solution context. A decrease in peptide density leads to more independent folding (i.e. fewer peptide-peptide interactions). Homogenous, self-assembled monolayers allow little room for manipulation of surface density, since peptides pack in close proximity. Mixed monolayers can be prepared by self-assembly with a mixture of thiol ligands; however, this approach can lead to heterogenous monolayers when the two ligands have very different properties.[157] To alter the peptide spacing in a predictable way, we utilized copper-catalyzed click chemistry to site-specifically attach peptides to a self-assembled monolayer of mixed alkanethiols, one of which has a terminal azide functionality (**Figure 38**). By varying the ratio of alkanethiolates in the SAM deposition solution, the resulting ratio in the monolayer can be controlled, which correlates to peptide density.
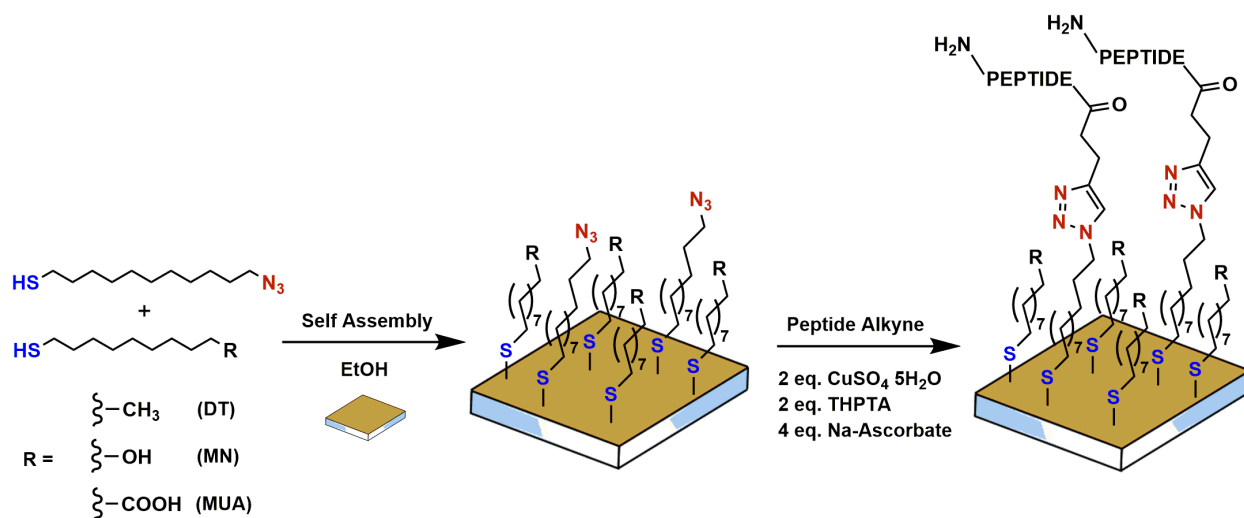
Figure 38. Scheme depicting surface construction via mixed monolayer self-assembly followed by a subsequent, on-surface click reaction with a peptide alkyne. The density of the peptide at the surface is the direct result of the ratio of alkanethiolates chosen during SAM formation.

Peptide-surface interactions can also affect peptide folding. In the simplest terms attachment to a surface introduces a loss of conformational freedom by an excluded volume effect relative to solution.[92, 158] Further, the peptide may interact with specific functional groups available at the surface interface in ways that favor or disfavor folding. Alterations to the terminal group of the "background" (i.e. non-azide containing) alkanethiolate were made to change the physical properties of the surface (**Figure 38**). Swapping a terminal methyl group for a hydroxyl or carboxylic acid creates a surface with increased hydrophilicity, the potential to hydrogen bond with the peptide, and, in the latter case, a negatively charged surface capable of electrostatic interactions. Decanethiol (DT), 9-mercaptononanol (MN), and 11-mercaptoundecanoic acid (MUA) were chosen so that the peptide would not be buried in the monolayer, which could hinder folding, as well as hamper click reaction efficiency.

Finally, it is well known that making changes to the primary sequence of a peptide can alter its folding propensity in solution. Peptides with differing degrees of helicity were designed to

evaluate whether solution folding conformations are retained once peptides are covalently bound to a surface via click chemistry. Furthermore, we wanted to assess whether these folds are dependent on density or surface polarity. More complex systems, such as a dimeric coiled-coil and dimeric enzyme, were also incorporated to assess the conformational changes resulting from each surface condition to these biomolecules. Peptides were functionalized with a N-terminal 4-pentynoic acid moiety to allow for covalent attachment to the surface bound azide via a click reaction. An alkyne bearing linker was utilized to attach the coiled-coil dimer onto the surface and the unnatural residue, propargyl lysine, was incorporated into the expressed enzyme for surface functionalization.

3.2 Evaluation of Mixed Alkanethiol SAMs and Small Peptide Incorporation

To create surfaces with tunable properties, we employed a two-step process: 1) the formation of a mixed monolayer containing the reactive azide component followed by 2) reaction of the surface bound azide with an alkyne-functionalized peptide via a copper catalyzed click reaction (**Figure 38**). Mixed alkanethiol monolayers were formed via self-assembly from solutions of decanethiol (DT), 9-mercaptononanol (MN), or 11-mercaptoundecanoic acid (MUA) and 11-azidoundecanethiol (AZT). The mole fraction of AZT was varied between 0.50 and 0.05 of the total thiol concentration in the monolayer deposition solution. Since statistical alkanethiol adsorption cannot be assumed,[159] each mixed monolayer was scrutinized for its surface alkanethiol composition. PM-IRRAS was used to compare the ratio of alkanethiolates in the deposition solution to the alkanethiol ratio in the resulting SAM. The intensity of the azide stretch ($\sim$ 2100 cm^{-1}) to the normalized CH$_2$ asymmetric stretch ($\sim$2926 cm^{-1}) provides a means of comparing the

azide content across SAMs. The intensity of the azide peak resulting from a pure AZT monolayer was assigned as 1.0 fraction azide surface coverage. The AZT content in each mixed monolayer was determined by taking the ratio of the normalized azide peak intensity to that in the pure AZT SAM (**Figure 39A**).

For all mixed monolayers, AZT was incorporated preferentially resulting in a greater azide proportion on the surface than in the SAM formation solution (**Figure 39B**). Generally, the preference for AZT was greatest in the mixtures bearing hydrophilic terminal groups. While the extent of AZT incorporation is somewhat alkanethiol dependent, the density of AZT at the surface can be controlled predictably via the alkanethiol ratio of the SAM deposition solution. The question of true mixing of the two alkanethiols at the surface versus the possibility of phase separation resulting in "islands" of each component was not investigated for these particular surfaces. While phase separation has been noted in the literature,[160] many others have noted the presence of uniform molecular mixing.[161-162] One possible theory seems to indicate that separated domains are more likely to form when the two components are of very different lengths or have a high proportion of hydrophobic groups that could preferentially cluster together.[159, 163] While the former is largely not the case in our SAMs, the latter may be relevant to some extent for DT surfaces with low AZT density. Importantly, creating a mixed alkanethiol monolayer prior to peptide incorporation allows for greater control over peptide placement, than, for instance, creating a mixed monolayer of peptides and alkanethiols, which would be more likely to form domains.
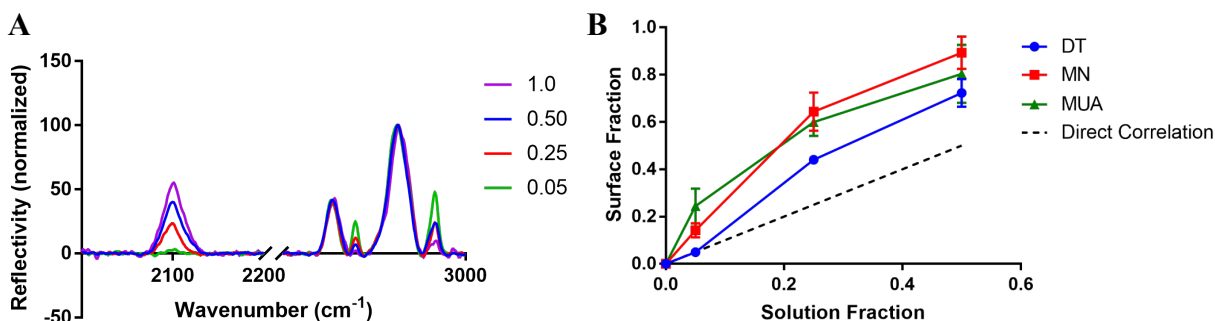
Figure 39. (A) Representative PM-IRRAS spectra of mixed monolayers (background = DT) resulting from various deposition solution fractions of AZT and (B) the fraction of AZT at the surface determined by PM-IRRAS plotted against the fraction of AZT in the SAM depostion solution. Error bars are the result of three independently prepared surfaces.

To confirm that the bulk properties of each mixed monolayer matched those expected based on composition, we assessed their wetting properties. The relative hydrophobicity of each mixed alkanethiol monolayer was quantified by the sessile contact angles of water (**Figure 40**). Contact angles above 100° were observed for entirely methyl-terminated surfaces, whereas contact angles of 40° were observed for entirely hydroxyl or acid terminated surfaces. Entirely azide covered surfaces gave contact angles near 80°. For the mixed monolayers, composition-dependent changes in contact angles between the two extremes provided a clear picture of the hydrophobicity changes resulting from each alkanethiol surface deposition mixture.
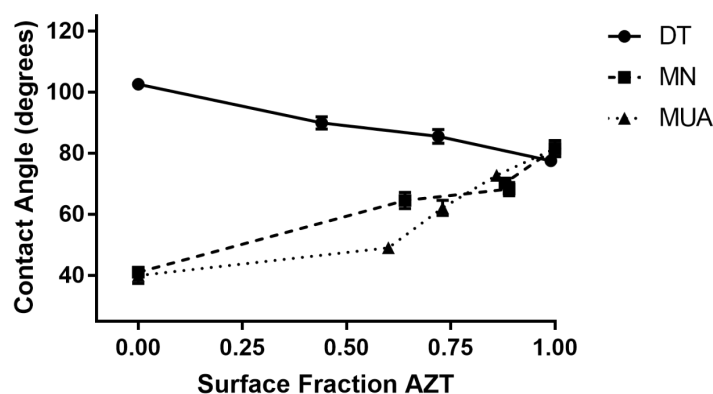
Figure 40. Water contact angles, reported in degrees, measured from 2 μl drops of 18 Ω water. Surface fraction AZT indicates the fraction of AZT at the surface estimated from PM-IRRAS measurements. Error bars are generated from three independent drops on each surface.

Simple oligopeptides were designed based on known sequences that display some degree of helicity in water (**Figure 41A**).[164] Incorporation of increased proportions of alanine (Ala, A) residues, which are helix-promoting, ensured differing folding propensities in solution. The inclusion of an alkyne group at the N-terminus provided an anchoring point for attachment to the mixed SAMs via click chemistry. Peptides **9** and **10** were synthesized via solid phase peptide synthesis and purified by preparative reverse phase HPLC. The identity and purity of each peptide was confirmed by analytical HPLC and MALDI-TOF mass spectrometry. Solution folding propensity was assessed by both circular dichroism (CD) spectroscopy and solution FTIR. The CD spectrum of peptide **9** showed minima at 222 and ~208 nm, characteristic of right-handed helical secondary structure (**Figure 41B**). For peptide **10**, the minimum at 222 nm decreased significantly in magnitude and the lower wavelength signal blue-shifted to ~200 nm. These changes are both indicative of a significant increase in random coil character. Solution FTIR spectra in D_2O display a shift in the amide I band from 1637 cm^{-1} for peptide **9** to 1645 cm^{-1} peptide **10** (**Figure 41C**).

This 8 cm^{-1} shift indicates a difference in relative helical populations in solution consistent with CD data.
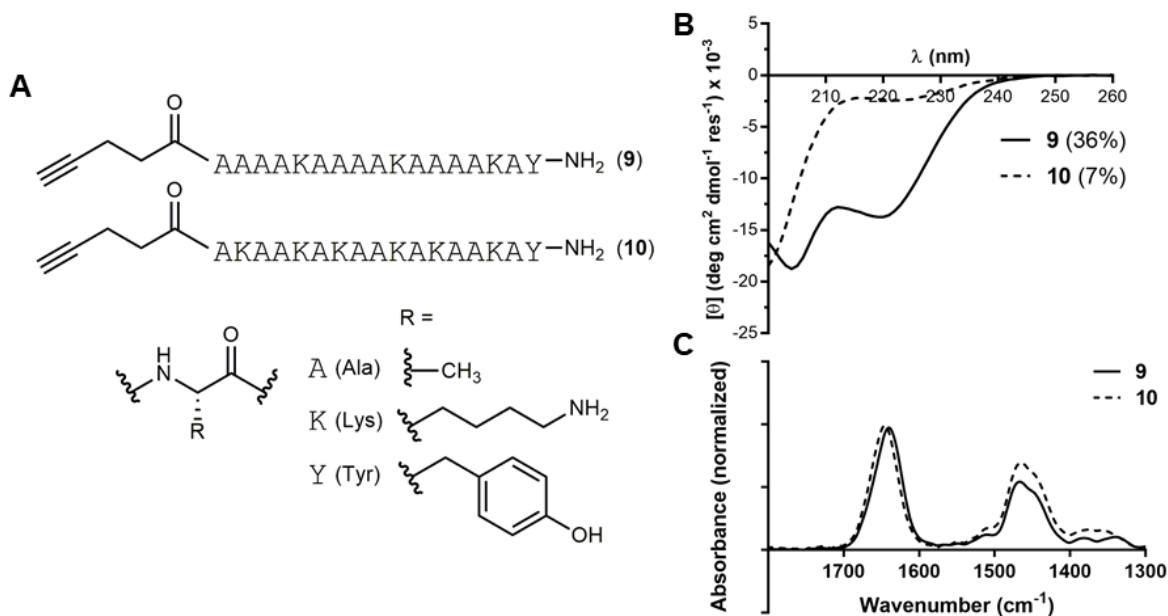
Figure 41. (A) Primary sequences and (B) CD spectra (50 μM in 10 mM phosphate pH 7.2) of peptide alkynes **9** and **10**. The estimated helical population is indicated in parentheses. (C) Amide I region from solution FTIR of peptides **9** and **10** (5 mg/mL in D$_2$O).

PM-IRRAS was used to analyze the peptide-incorporated SAMs resulting from the copper-catalyzed click reaction of peptides **9** and **10** with a series of azide containing SAMs of varying compositions. To assess reaction efficiency, the amount of unreacted azide was measured by the intensity of the azide peak relative to the normalized CH$_2$ asymmetric stretch of the PM-IRRAS spectrum before and after overnight reaction (**Figure 42A**). The reaction yields are lower for surfaces with greater fractions of AZT (**Figure 42B**). This observation is attributed to increased peptide density which leads to more steric crowding and hindered azide accessibility. Similar reaction yields for MN and DT containing SAMs with less than 70% surface fraction AZT provides strong evidence for a steric limit. Once peptide coverage is greater than about 70%, reaction yield begins to decrease as incorporated peptides begin to block available azide terminal groups. For

MUA containing surfaces, this steric limit appears to be lower, possibly because MUA is slightly longer than MN or DT which may hinder azide accessibility further. There was no significant difference in the above trends in reaction yield based on the peptide sequence used in the reaction.
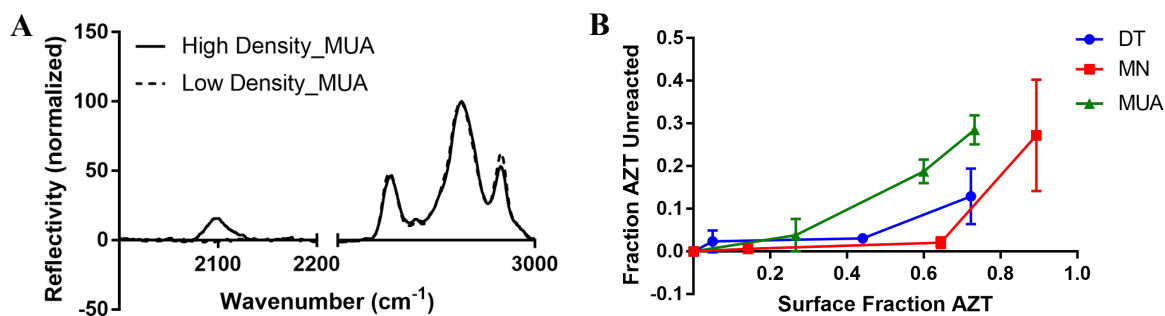
Figure 42. (A) Representative PM-IRRAS spectra for mixed MUA:AZT surfaces displaying the CH_2 and azide regions after copper-catalyzed click reactions were performed. High density surfaces are those with a surface AZT fraction above the steric limit and low density surfaces are those below 0.30 surface mole fraction AZT. (B) Surface click reaction yields shown as the fraction of AZT left unreacted versus the fraction of AZT in the SAM prior to the reaction as determined via PM-IRRAS. Error bars are the result of at least three surface reactions with either peptide sequence.

The amide I and amide II bands of the PM-IRRAS spectra were used to analyze peptide folding and orientation. Changes in position or shape of the amide I band signify differences in the populations of secondary structures present within a sample,[117] whereas changes in the intensity ratio of the amide I: amide II bands signifies differences in peptide orientation relative to the surface.[165] The amide I band showed a maximum in the range of 1661-1666 cm^{-1} across the series of monolayers examined (**Figure 43**). Amide I bands in this region are typically attributed to some amount of distorted helical character.[141, 166] Generally, peptide **10** had a broader amide I band which is indicative of more heterogeneity in the folding patterns present on the surface. Since peptide **10** has more random coil character in a solution context, it is expected to have more variation in folded population at the surface. No significant trends in the amide I band could be

84

correlated to surface polarity or density of peptide for this system. The intensity ratio of amide I:

amide II bands was roughly 2:1 across all monolayers examined.
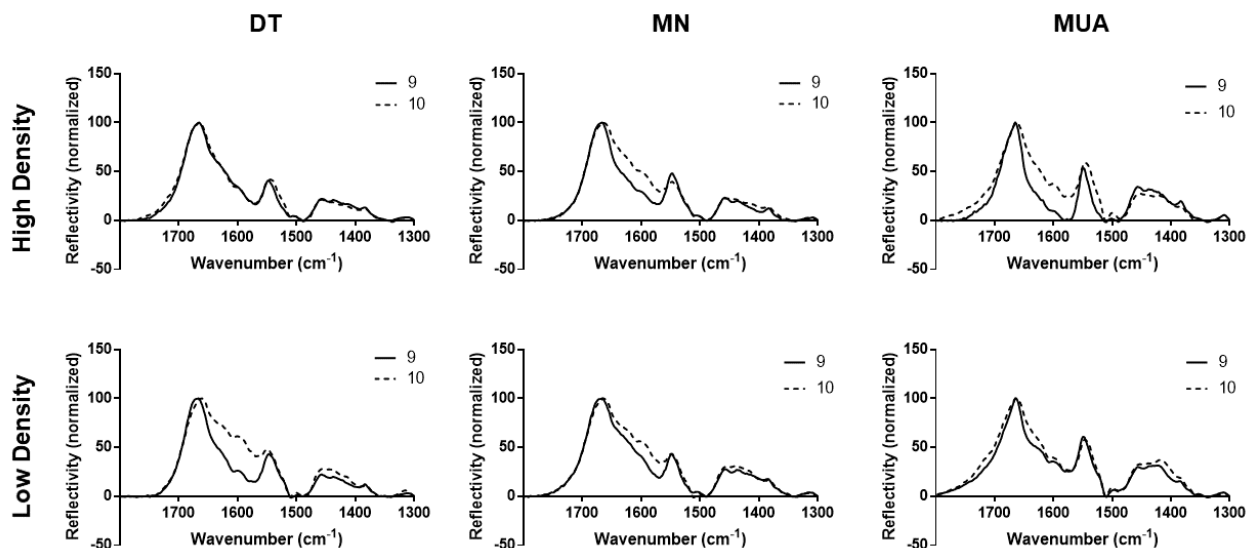
Figure 43. Amide region of the PM-IRRAS spectra for surfaces with high (0.50 fraction AZT in deposition

solution) and low (0.05 fraction AZT in deposition solution) peptide density and changing polarities (DT, MN, or

MUA alkanethiol backgrounds).

To further understand the heterogeneity in peptide folding at the surface, we synthesized

N-terminal thiol variants of each peptide, **9-SH** & **10**-SH (**Figure 44A**). These variants fold

similarly to their counterparts in solution (**Figure 44B**). Direct thiol attachment via self-assembly

of the peptide onto a gold surface creates a well-ordered monolayer due to the peptides packing in

close proximity. The amide I bands for these monolayers were significantly narrower than those

for **9** or **10**, indicative of a more homogeneous array of peptide structures (**Figure 44C**). The

clicked SAMs, which create more space between peptide neighbors, lead to more heterogeneous

structural characteristics and possibly higher orientational disorder. The amide I band for **9-SH**

(1665 cm^{-1}) appeared at a similar position as the clicked surfaces, while the amide I band for **10-**

SH was slightly red-shifted (1659 cm^{-1}), which may indicate increased helical character due to

higher packing densities and molecular crowding. This crowding may force the random coil into a more structured conformation.
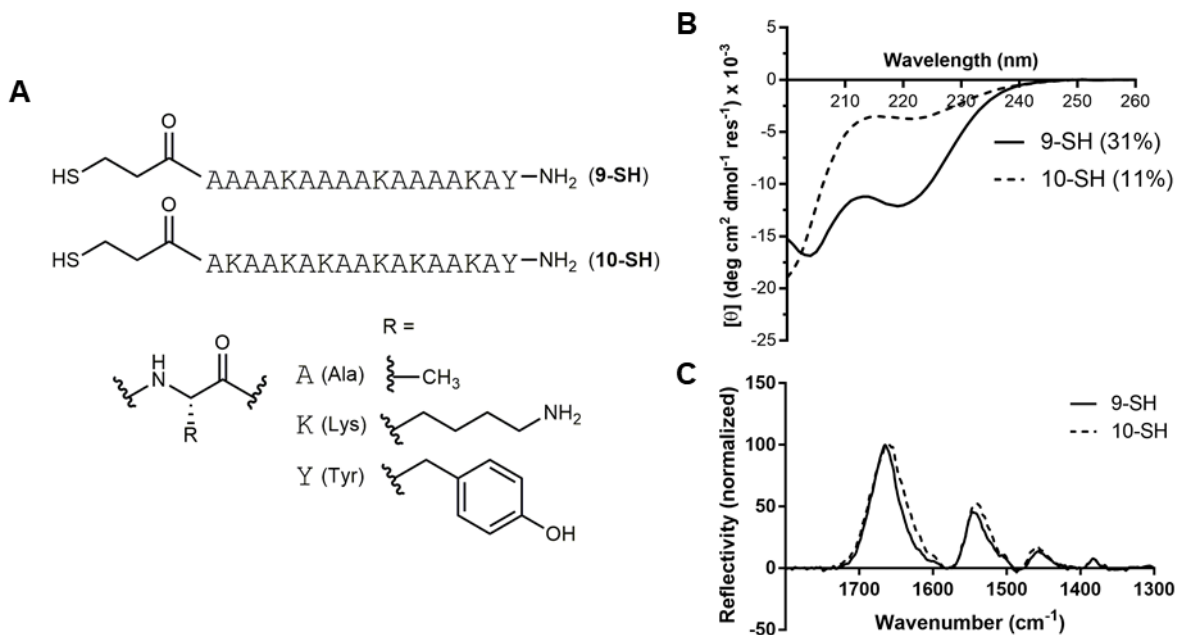
Figure 44. (A) Primary sequences and (B) CD spectra (50 μM in 10 mM phosphate pH 7.2) of peptides **9-SH** and **10-SH**. The estimated helical population is indicated in parentheses. (C) Amide region of the PM-IRRAS spectra for SAMs formed from peptides **9-SH** and **10-SH**.

Summarizing findings to this point, we developed and validated a method using mixed monolayer self-assembly and subsequent copper-catalyzed click chemistry for creating well defined peptide functionalized surfaces of tailored density and polarity. Increased conformational heterogeneity was observed for the click surfaces when compared to self-assembled Au-S monolayers of similar peptides, presumably due to the difference in surface packing. It is difficult to determine from the data presented if variations in peptide surface folding are directly correlated to peptide density or surface polarity for these oligopeptide monolayers. Differences in amide I band shape or position are challenging to discern due to the broadness of these bands and deconvolution of such peaks can be problematic or misleading. While conformational differences in solution are observed for these sequences, we reasoned surface folding may be harder to discern

due to the low helical content. To test this hypothesis, we sought to prepare a series of monolayers bearing a more defined folded architecture.

3.3 Coiled-coil Monolayers

To bear on the hypothesis that folding differences are easier to discern with a more defined folded structure, we incorporated a peptide that should have a very high helical propensity in solution. We hoped that any deviations on the surface from an almost completely helical population would be simpler to differentiate and ultimately help to assess the effect of surface polarity and density on peptide conformation. Highly helical, stable structures are difficult to achieve with short ($<$ 30 residue) peptides. Techniques such as peptide stapling can stabilize helical folds,[167] however, the peptide will be so constrained that it may not show any differentiation in structure when exposed to differing surface conditions. Coiled-coil peptides represent a class of naturally occurring sequences that are short enough to be synthetically realized and that fold into stable multi-helical quaternary structures. We chose the GCN4 leucine zipper (GCN4-p1) as the coiled-coil domain for incorporation into tailored surfaces. GCN4-p1 is a 33-residue dimerization domain of the yeast transcription factor GCN4.[168] GCN4-p1 folds and assembles in solution to form a parallel dimeric coiled-coil;[169] however, it has been observed to populate a trimeric assembly under certain conditions.[170] The following minor alterations were made to the native sequence to generate peptide **11**: 1) norleucine (Nle, B) was substituted for methionine to prevent unwanted oxidation and 2) the sequence glycine, glycine, cysteine (GGC) was appended to the C-terminus (**Figure 45**). The newly introduced cysteine will be used as a functional handle for attachment to surfaces, as detailed below.
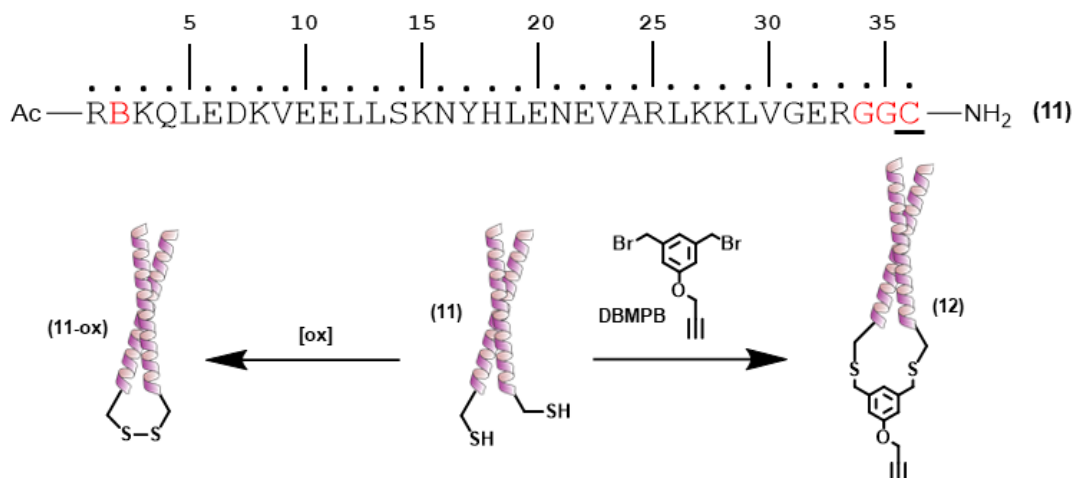
Figure 45. Sequence of GCN4-p1 variant, peptide **11,** and schematic of the the oxidation of peptide **11** to **11-ox** and the reaction between peptide **11** dimer and DBMPB linker to form peptide **12**.

Peptide **11** was synthesized by Fmoc solid phase methods and purified via reverse-phase HPLC. We envisioned using **11** to prepare a series of surfaces: 1) azide-alkyne clicked surfaces with DT, MN, and MUA backfills and 2) self-assembled Au-S surfaces. To attach the coiled-coil to a surface using the click reaction conditions outlined for peptides **9** and **10**, we envisioned a linker functionalized with a free alkyne that would covalently link the homodimeric coils. Synthesized 1,3- di(bromomethyl)-5-propargyloxybenzene (DBMPB) was used to link the dimeric coiled-coils through the C-terminal cysteine side chains, creating **12** (**Figure 45**). The DBMPB linker has been reported in the literature as a means of creating cyclic peptides with subsequent attachment of a fluorophore through click reaction with the alkyne,[171] but not as a means for surface attachment. After reaction of **11** with DBMPB, the azide containing SAMs react with the propargyl group of DBMPB under copper catalyzed click conditions (**Figure 46**). To create self-assembled Au-S surfaces, peptide **11** was oxidized, creating a disulfide bond between the terminal cysteine side chains on each coil, to produce peptide **11-ox** (**Figure 45**). Peptide **11-ox** was then self-assembled onto the substrate through direct Au-S attachment.
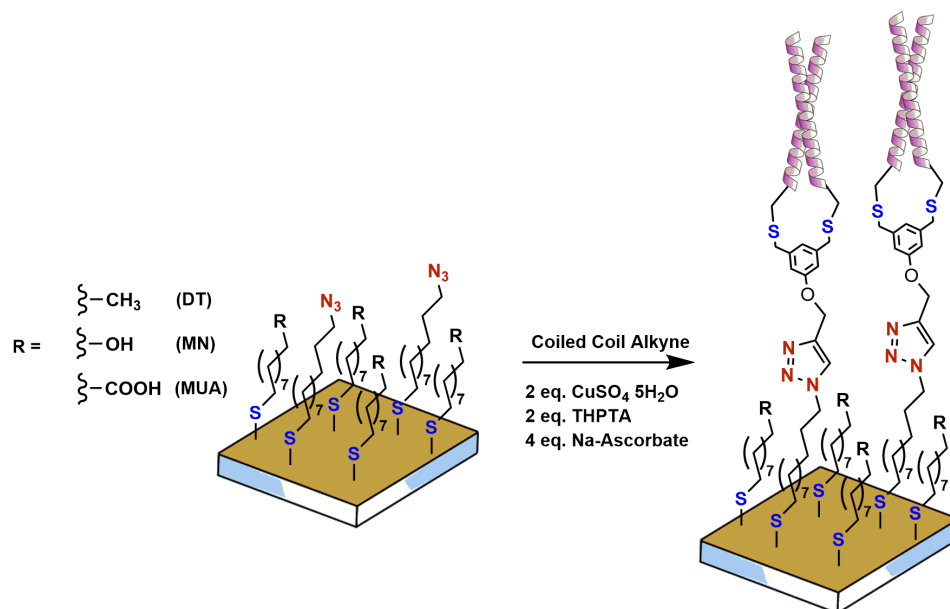
Figure 46. Schematic depicting the click reaction mediated incorporation of peptide **12** onto mixed alkanethiol SAMs.

The solution folding propensity of peptides **12** and **11-ox** was evaluated via CD (**Figure 47A**). Both showed strong helical character in water, indicated by double minima at 208 and 222 nm. Peptide **11-ox** showed a somewhat greater helical population than peptide **12**. It is likely that insertion of the DBMPB linker causes increased rigidity in the C-terminal region, partially disrupting the helical fold. However, thermal unfolding data indicates that the stabilities of **11-ox** and **12** are still comparable (**Figure 47B**).
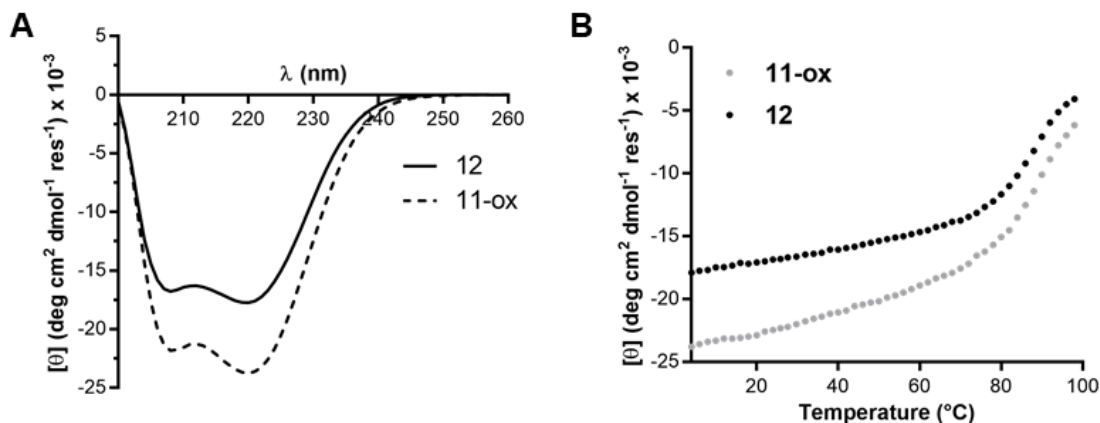
Figure 47. (A) CD spectra of peptides **11-ox** and **12** (50 μM in 10 mM phosphate buffer pH 7.0). (B) CD temperature melt of peptides **11-ox** and **12** (50 μM in 10 mM phosphate buffer pH 7.0).

Surfaces were incubated overnight in a solution of peptide **11-ox** to create a self-assembled monolayer of the coiled-coil. Surfaces covalently incorporating peptide **12** via a copper catalyzed click reaction were prepared using methods analogous to the small peptide click surfaces. The resulting surfaces were analyzed via PM-IRRAS. Reaction yields were comparable to the small peptide surfaces. Low density AZT surfaces had very minimal amounts of AZT remaining after the click reaction and the high-density surface had about 30% AZT remaining. The amide I bands were indistinguishable when comparing surface backfills or even increased peptide density (**Figure 48**). The amide I band was positioned between 1660-1662 cm^{-1}, which is red-shifted 1-4 cm^{-1} as compared to surfaces incorporating peptides **9** and **10.** This observation is consistent with an increased helical population. However, based on the large differences in helical population in solution, peptide **12** was expected to yield an amide I band red-shifted 8 cm^{-1} or more. These results indicate that covalent attachment to a surface may have a destabilizing effect on the quaternary fold. The amide region of peptide **11-ox** SAMs were indistinguishable from the click monolayers. This indicates that packing density may not have as big of an effect on the folded conformations

present at the surface if some degree of structure exists in solution (i.e. peptide **9-SH** and **11-ox** SAMs).
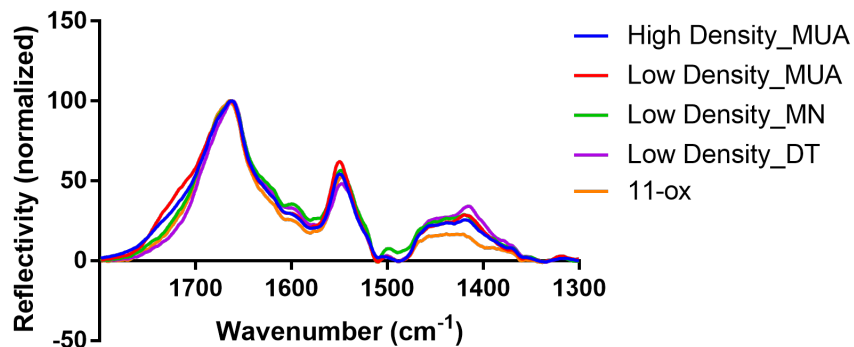
Figure 48. Amide region of the PM-IRRAS spectra for click-type monolayers of peptide **12** and a self-assembled monolayer of peptide **11-ox**. The peptide density was varied (low density = 0.05 fraction AZT and high density = 0.50 fraction AZT in SAM deposition solution) and the surface polarity via the background alkanethiol.

Taken together, the results for the short peptide and coiled-coil monolayers highlight the challenges in applying PM-IRRAS to probe for subtle changes in peptide conformation at a surface. Broad peaks, indicative of heterogeneous folding, were seen for all surface conditions, making analysis challenging. An additional challenge encountered was employing an accurate baseline correction method. Initially baseline correction was performed manually by choosing points along the Bessel function. However, this method may introduce baseline artifacts or influence peak shape. To address this, an adaptive partial least-squares technique (arPLS) for baseline correction, originally designed for processing IR and Raman spectra,[172] was adopted for processing the PM-IRRAS spectra. While this method is much more consistent than manual corrections, assertions made while baseline correcting, such as defining sufficient regions where no peaks are present, may still influence the spectra. Based on the above, we pursued a system for surface functionalization that would provide a maximally sensitive probe for subtle changes in

local chemical environment as well as a convenient indirect method for probing structural rearrangements.

3.4 Investigating Enzyme Activity on Tailored Surfaces

An indirect method for identifying structural changes in biomolecules is to examine function. Altered bioactivity is often the result of a change in conformation, since structure and activity are so closely linked for most peptides and proteins. We chose to move away from small peptides to a much larger biomolecule— an enzyme. Choosing an enzyme allows us to monitor catalytic activity as a means to relate function to protein structure. Additionally, since minimal structural changes were detected for small peptides based on surface polarity or peptide density, analysis of a surface-bound enzyme will allow us to test our hypothesis on a larger system. It has been demonstrated both computationally and experimentally that proteins may alter their conformation upon interaction with a surface due to multiple factors including molecular crowding or preferential interactions with the surface interface that lead to structural rearrangements.[173] However, it is important to note that the majority of these studies evaluate the conformational changes of non-specifically bound proteins. By incorporating an enzyme site-specifically using the surface construction methodology and examining protein activity, we aim to provide support for the idea that tailoring surface composition can be a useful method for controlling protein behavior. We hypothesized that surface composition, specifically surface polarity, would influence enzyme activity.

Bacterial alkaline phosphatase (BAP) was chosen for this study since it has a known 3D structure and an activity assay with a simple colorimetric readout which can be readily adapted for

a surface-bound context (**Figure 49A**).[174] Importantly, BAP does not have any surface cysteines

and is stable at room temperature. BAP is a homodimeric protein that contains two active sites

which require metal ions to be bound for proper catalysis.[175-176] For incorporation onto the surface

using the click reaction methodology, a single point mutation of lysine39 (K39) to propargyl lysine

(PK) was made (**Figure 49C**). K39 is located on an exposed surface on the face opposite the

enzyme's active sites. PK incorporation at this site is followed by attachment of the protein to an

the azide-functionalized surface via click chemistry which should orient the active sites away from

the interface, allowing them to be more accessible to substrate.
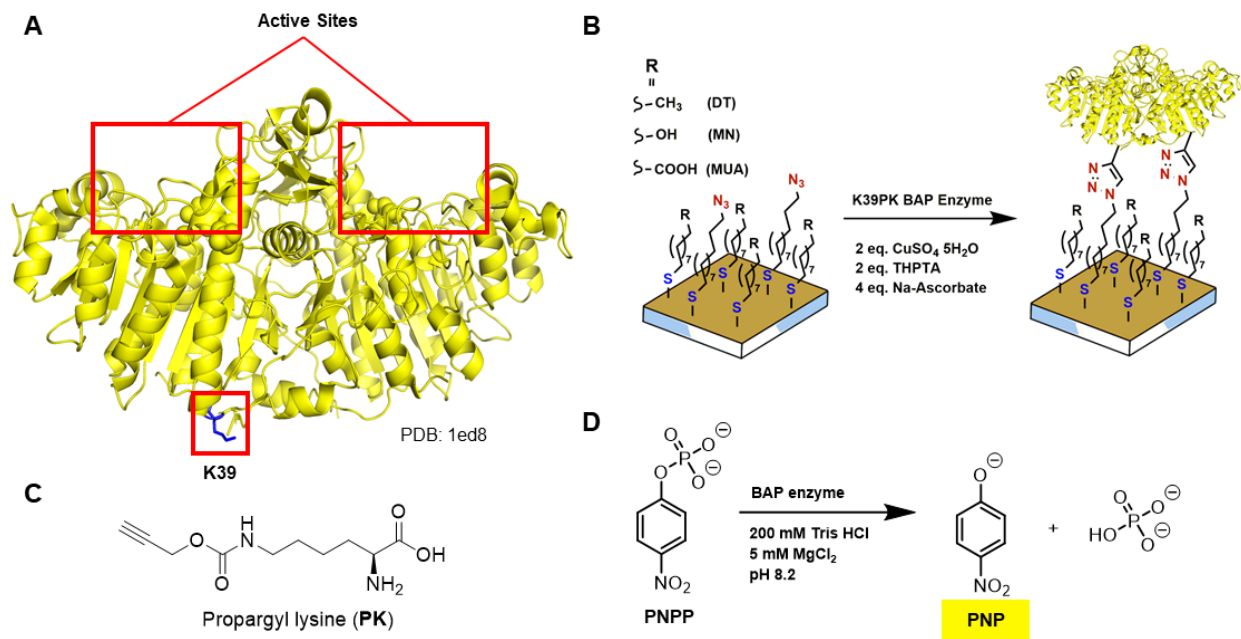
Figure 49. (A) Wild type BAP enzyme (PDB: 1ed8) (B) Schematic describing the incorporation of K39PK into mixed monolayers via click chemistry. (C) Structure of propargyl lysine (PK). (D) The hydrolysis of PNPP used as a colorimetric readout to measure BAP activity.

BAP has the physiological role of dephosphorylating compounds and is largely conserved

across a multitude of organisms.[176] A convenient in vitro assay for BAP activity uses *p*-nitrophenol

phosphate (PNPP) as the substrate (**Figure 49D**). PNPP is hydrolyzed by the enzyme to *p*-

nitrophenol (PNP) which is yellow in color and can be monitored by visible absorption

spectroscopy (λ_{max} 405 nm).[174] As a positive control, the expressed wild type (WT) and K39PK mutant enzymes were tested for their bioactivity in solution using the described BAP activity assay. The point mutation at K39 does not affect BAP bioactivity, as predicted (**Figure 50**).
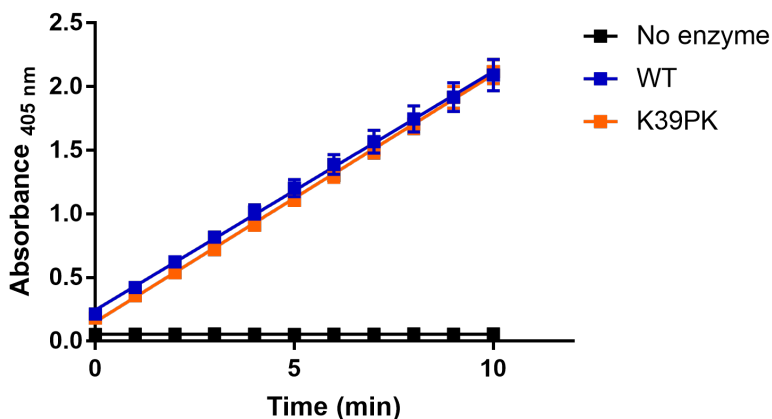
Figure 50. Enzyme activity assay for wild type (WT) and mutant (K39PK) BAP enzymes (10 nM enzyme, 5 mM PNPP substrate) where the absorbance at 405 nm is measured as a function of time.

Click surfaces were prepared by reacting the mutant K39PK enzyme with DT, MN, or MUA mixed monolayers (**Figure 49B**). The density of AZT (which is related to enzyme density) was kept consistent at around 0.05 mol fraction AZT for every alkanethiol backfill. This density was controlled by choosing a ratio of alkanethiols in the SAM formation solution that is estimated to yield a 5 % AZT SAM (0.05 mol fraction DT; 0.02 mol fraction MN; 0.01 mol fraction MUA). Low density surfaces were chosen due to the size of BAP, which has a diameter of ~10 nm. It is expected that BAP will be fairly well packed even at a low AZT density. The assay was then adapted for the surface-bound enzyme, where clicked surfaces were analyzed for K39PK activity. The change in absorbance measured at 405 nm over time was used to calculate the reaction velocity using a literature reported extinction coefficient of 18000 M^{-1} cm^{-1} for PNP and a measured pathlength of 1.8 mm (25 µl in a 384 well plate).[177] The reaction velocity serves as a measure of enzymatic activity. Mixed monolayers were also exposed to the WT enzyme, which should not

react under click conditions and therefore not be bound to the surface. However, some activity was observed on surfaces exposed to the WT protein, presumably from non-specifically adsorbed material. Sonication was used as a method to reduce this adsorption, as well as to remove the copper catalyst and associated ligand. Control experiments in solution show sonication leads to a moderate decrease in enzymatic activity. Thus, we kept sonication times uniform (60 min) to allow reaction velocities to be compared across surfaces while minimizing the amount of non-covalently bound protein (**Figure 51A**).
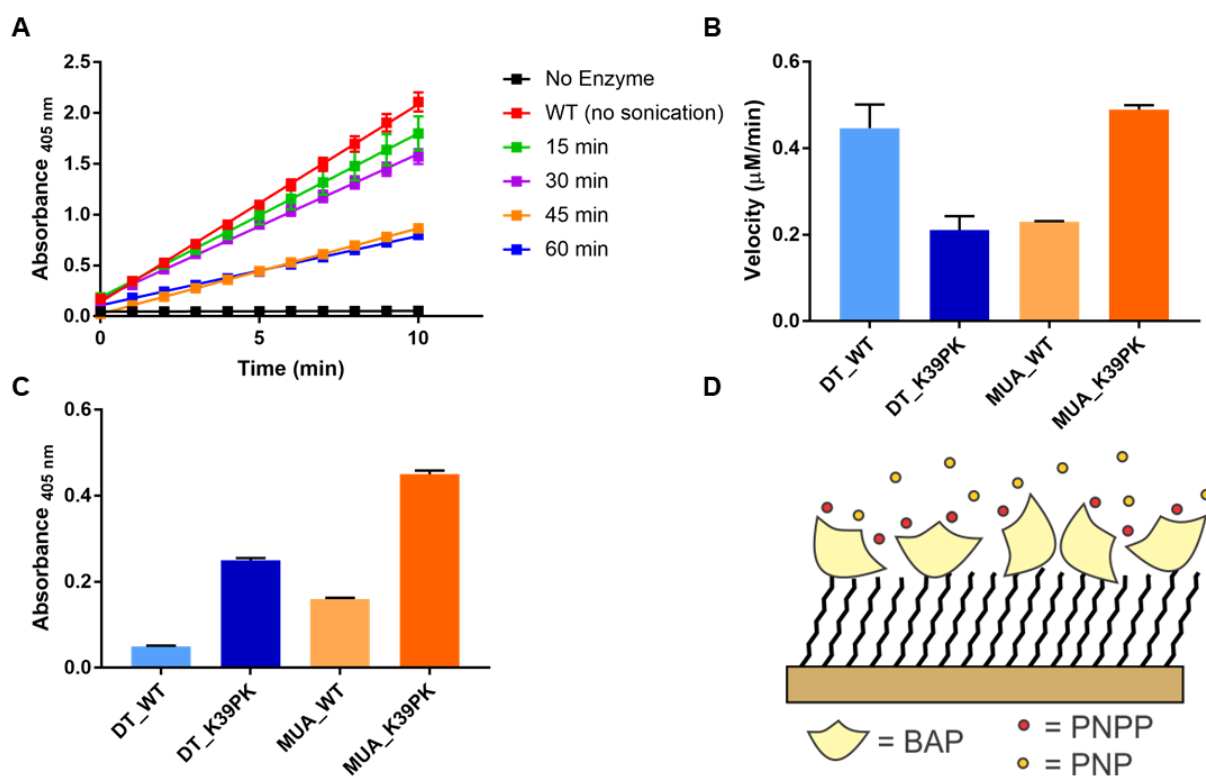
Figure 51. (A) Activity of the WT BAP enzyme in solution after sonicating for indicated duration. (B) Velocity of substrate conversion by DT and MUA surfaces reacted with WT or K39PK protein. Surfaces were sonicated for 60 minutes after functionalization, prior to the assay. (C) Velocity of substrate conversion by DT and MUA surfaces reacted with WT or K39PK protein when 1% v/v PEG 1500 is included in the click reaction. Surfaces were sonicated for 60 minutes after functionalization, prior to the assay. (D) Representation of a K39PK BAP surface; various orientations and conformations of the enzyme are expected to be present based on the surface's properties, which may influence the accessibility of the active sites and therefore enzymatic activity.

Even after a 60-minute sonication time, activity from non-specifically adsorbed WT protein was significant, particularly on hydrophobic surfaces (**Figure 51B**). Higher amounts of protein adsorption on hydrophobic alkanethiol surfaces compared to hydrophilic surfaces has been previously noted in the literature, typically due to strong non-specific interactions.[86] The observed higher activity of the WT exposed DT surface compared to the K39PK surface indicates that a large amount of protein is adsorbed to the hydrophobic DT surface. Covalently-bound K39PK is possibly more ordered than adsorbed WT BAP since the attachment site limits the number of orientations possible (**Figure 51D**). Orientationally disordered WT BAP may allow space for more enzyme to attach to the surface, resulting in high activity. In an effort to reduce the amount of non-specifically adsorbed WT protein, 1% v/v polyethylene glycol (PEG) 1500 was added to the click reaction conditions (**Figure 51C**). PEG has been shown to solvate proteins, specifically interacting with hydrophobic regions, which may prevent BAP adsorption to the hydrophobic DT surface.[178-179] With the addition of PEG, hydrophobic surfaces exposed to WT protein showed a marked decrease in activity indicating non-specific protein adsorption was greatly reduced. The observed activity for DT surfaces with K39PK enzyme remained the same for surface reactions performed with and without the PEG additive, providing strong evidence for the covalent attachment of K39PK. For hydrophilic MUA surfaces the addition of PEG did not greatly affect non-specific protein adsorption of the WT BAP. Likely, BAP is interacting with the MUA surfaces via different types of interactions (i.e salt-bridges or hydrogen-bonding) that are unable to be effectively disrupted by the addition of PEG. Attempts to reduce non-specific interactions of the WT BAP on hydrophilic surfaces using increased salt and buffer concentrations also did not prove to be fruitful (data not shown).

96

Another route for blocking non-specific interactions between a protein of interest and a surface is the addition of bovine serum albumin (BSA) in large excess. The logic here is to ensure the majority of non-specifically bound protein is not the functional biomolecule of interest.[180] The addition of 0.5% wt/v BSA to the surface click reaction conditions led to decreased activity of K39PK BAP, likely because BSA may also block reactive azide moieties. Importantly, the introduction of BSA resulted in a greater proportional decrease in activity for the WT surfaces compared to other conditions tested (**Figure 52**). For this reason, these results can help bear on our central question regarding the effect of surface polarity on protein activity.
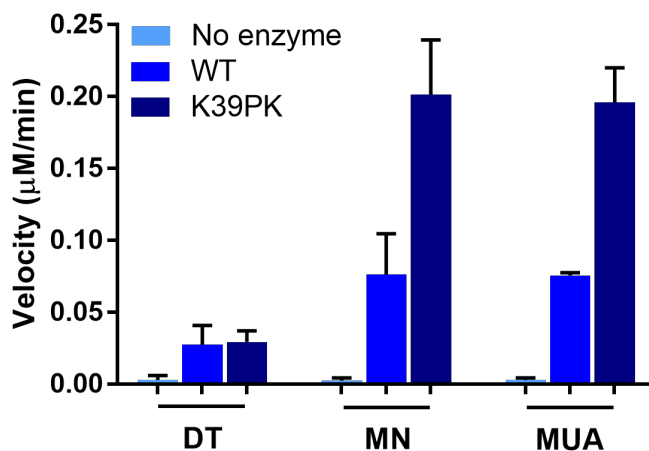
Figure 52. Velocity of subtrate conversion by DT, MN, and MUA surfaces exposed to no enzyme, WT, and K39PK enzyme and 0.5% wt/v BSA. The absorbance at 405 nm was recorded every 30 minutes for 6 hours with an initial concentration of 10 mM PNPP. Error bars are the result of 3 independent experiments.

For the covalently bound K39PK enzyme, hydrophilic surfaces (MN and MUA) had significantly higher activity than hydrophobic surfaces (DT). As discussed in Chapter 1, structural studies on human fibrinogen and albumin adsorbed onto alkanethiol SAMs revealed that protein adsorbed on hydrophobic surfaces had a large amount of conformational rearrangement; secondary structures held together via hydrophobic contacts refold to form hydrophobic interactions between nonpolar functional groups within the protein and terminal methyl moieties on the SAM surface.[86]

These newly formed interactions are proposed to be favorable because they reduce the overall solvent exposed surface area and dehydrate the surface.[86] In our system, covalently tethered K39PK enzyme also likely undergoes a conformational change to favorably interact with the hydrophobic, DT surface. Structural rearrangement results in a clear decrease in activity since the active site may be altered and unable to as effectively interact with the substrate. Hydrophilic surfaces, MN and MUA, should also interact with K39PK, however, structural rearrangement on hydrophilic surfaces occurs to a much smaller extent, causing less structural perturbation of the active site and retained activity. A similar conclusion was reached by the Latour lab for proteins adsorbed on hydrophilic surfaces— structural changes were not as pronounced as on hydrophilic surfaces since charged and polar residues on the outer surface of the proteins interact with the alkane terminal groups resulting in minimal perturbation.[86] In our results, no significant difference in reaction velocity was observed between K39PK enzyme bound to MUA and MN surfaces.

It is important to note that although the addition of the BSA blocking agent did decrease the activity of surfaces exposed to WT enzyme, the residual activity is still non-zero. Interestingly, the activity of the WT enzyme non-specifically adsorbed onto the DT surfaces was also significantly less than WT enzyme adsorbed on MN or MUA surfaces. This observation may arise from varying amounts of structural perturbation similar to those described for the K39PK enzyme or, more likely, these variances may arise from differences in the effectiveness of BSA. BSA has been shown to have, on average, a higher blocking efficiency on hydrophobic versus hydrophilic surfaces.[180] Therefore, more of the surface area on a DT surface may be blocked by BSA compared to MUA or MN surfaces, resulting in decreased levels of WT BAP adsorbed to hydrophobic surfaces and therefore decreased activity. Considering this explanation for the trends seen in WT activity, an alternate explanation for the activity differences seen across K39PK surfaces would be

the effectiveness of BSA. Although we cannot definitively rule out that possibility with the data presented here, the enhanced activity of K39PK MUA surfaces over DT surfaces under all conditions tested, including without blocking agents, makes this explanation less likely.

Since inhibiting adsorption of the WT enzyme proved to be a significant challenge, we aimed to confirm the covalent attachment of K39PK to the surface and to estimate the activity resulting from any adsorbed K39PK. To verify that the K39PK enzyme is covalently bound to the surface, control click reactions excluding the copper catalyst/ ligand complex were performed, which prevents the reaction between K39PK and the azide terminated alkanethiol SAM (**Figure 53**). Greatly reduced activity was noted for surfaces exposed to K39PK without the required catalyst, indicating that the K39PK enzyme is covalently bound to the surface when copper is present in the reaction. Surprisingly, only minimal activity contributions arise from adsorbed K39PK, indicating less K39PK is adsorbed than WT BAP. This would indicate the presence of copper and its ligand enhance adsorption to some extent, though to our knowledge this has not been commented on in previous literature. More investigations are required to better understand this result.
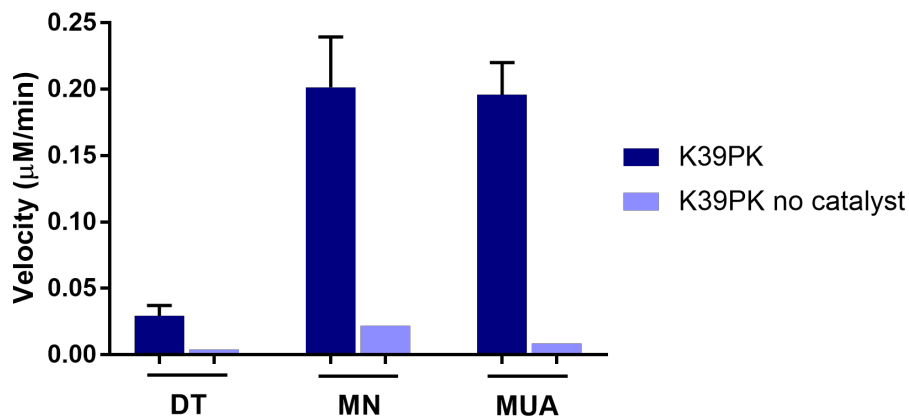
Figure 53. Velocity of substrate conversion by DT, MN, and MUA surfaces exposed to K39PK enzyme with and without the copper catalyst. The absorbance at 405 nm was recorded every 30 minutes for 6 hours with an initial concentration of 10 mM PNPP.

Overall the results obtained for the BAP system indicate that covalent attachment to tailored surfaces is a useful method for modulating protein folding and activity. Covalent attachment allows for control over orientation of the enzyme. Based on the placement of the reactive moiety within the protein, the active sites can be made more accessible than in the random orientations present in non-specifically adsorbed protein surfaces. Molecular crowding, which can also change protein conformation, is also controlled using the click surface modification route. Finally, higher reaction velocities are observed for enzymes covalently bound to hydrophilic surfaces, likely due to differing degrees of structural perturbation upon interacting with the surface. The results indicate surface polarity is another modifiable handle for creating tailored protein surfaces.

3.5 Summary

Through the creation of tailored surfaces, we demonstrated modification of surface properties such as molecular crowding and surface polarity. Mixed monolayers incorporating a functional azide handle can be used to covalently attach small peptides and proteins equipped with a functional alkyne handle using copper catalyzed click chemistry. This methodology proved fairly generalizable. Peptide and protein conformations were investigated on these surfaces; we concluded that covalent attachment to a surface does alter folding as compared to a solution context.

Differences in peptide and coiled-coil surface folding based on changes to surface polarity or peptide density were difficult to distinguish using PM-IRRAS, which highlights the challenges of studying surface folding using even this fairly sensitive method. Open questions still remain regarding how to retain the structural differences of small peptides observed in solution for a surface context. Surface polarity proved to have a significant effect on the activity of a modified BAP enzyme due to differences in the interactions between the protein and the surface. However, a portion of the activity seen may arise from differing amounts of adsorbed protein (BSA or BAP) at the surface.

Finally, the best method to carry out surface structural studies depends on the sensitivity required and the proposed application of the material. PM-IRRAS requires the surface to be very dry, comparable to the context used for PFM experiments (described in Chapter 2), where humidity is minimized. In contrast, the enzymatic assay was performed with the surface in an aqueous context. The presence or absence of water surely has an effect on the conformations present and should be considered in regards to surface folding studies. On-surface CD would be one technique that would allow both solvated and dry surfaces to be compared and is an interesting avenue for

further study. Exploring the changes to both structure and activity of biomolecules upon surface attachment gives insights into considerations for optimizing the design of future biomaterials.

3.6 Experimental

3.6.1 General Information

All Fmoc amino acids and resins used for solid phase synthesis were purchased from Novabiochem. Solvents and other reagents were purchased from Sigma-Aldrich and used without further purification. Reverse phase HPLC was carried out using either Phenomenex Luna or Jupiter C18 columns. Products were eluted using gradients between 0.1% TFA in water (solvent A) and 0.1% TFA in acetonitrile (solvent B), monitored by UV detection at 220 and 280 nm. MALDI-TOF MS experiments were performed on an ultrafleXtreme (Bruker) using α-cyano-4-hydroxycinnamic acid or sinapic acid as the ionization matrix. Wild type and K39PK mutant BAP enzyme were expressed and purified by Alaina McDonnell.

3.6.2 Peptide Synthesis and Reactions

Solid Phase Peptide Synthesis

Peptides **9**, **10,** and **11** were synthesized by microwave-assisted Fmoc solid phase methods on a CEM MARS 5 microwave using NovaPEG rink amide resin (0.1 mmol scale). The resin was swollen in DMF for 15 min prior to the first coupling reaction. In a typical cycle, a 0.1 M solution of HCTU in NMP (for **9** and **10**: 4 equiv relative to resin, 4 mL, 0.40 mmol; for **11**: 5 equiv relative

to resin, 5 mL, 0.50 mmol) was added to Fmoc-protected amino acid (for **9** and **10**: 4 equiv relative to resin, 4 mL, 0.40 mmol; for **11**: 5 equiv relative to resin, 5 mL, 0.50 mmol) followed by DIEA (6 equiv, 0.60 mmol). After a 2 min preactivation, the solution was transferred to resin, and the mixture was heated to 90 °C over 1.5 min, followed by a 2 min hold at that temperature. Fmoc deprotection was carried out with 20% 4-methylpiperidine in DMF (for **9** and **10**: 6 mL; for **11**: 8 mL), and the mixture was heated to 90 °C over 2 min, followed by a 2 min hold at that temperature. The resin was washed three times with DMF after each coupling and deprotection cycle. For peptides **9** and **10**, the N-terminus of each peptide was capped with pentynoic acid after the final deprotection step by stirring the resin for 1 hour at room temperature using the coupling conditions described above. For **11**, Cys36 was double coupled at room temperature for 2 x 30 min and His18 was coupled at room temperature for 45 min. After the final deprotection step, the N-terminus was acetyl capped by stirring a mixture of acetic anhydride (200 ul), DIEA (400 ul), and DMF (1.6 ml) with the resin for 20 minutes at room temperature.

After the final coupling, the resin for all peptides was washed three times each with DMF, DCM, and MeOH, and dried under vacuum for at least 20 min. Peptides were cleaved from resin by treatment with a solution of TFA/EDT/H_2O/TIS (92.5%/3%/3%/1.5% by volume) for 3 hours (**9 & 10**) or 4 hours (**11**) followed by precipitation in cold ether (approx. 35 mL). The suspended peptide was collected by centrifugation and the white pellet was re-dissolved in 4:1 solvent A/solvent B for purification by preparative HPLC. The identity and purity of final products were confirmed by analytical HPLC (**Figure 54**) and MALDI-TOF MS (**Table 4**). Peptide stock solution concentrations were quantified by UV spectroscopy (Hewlett-Packard 8452A diode array spectrometer, $\varepsilon 276 = 1450$ cm^{-1} M^{-1} from the single Tyr in each sequence).

Table 4. MALDI-TOF MS data for peptides **9, 10, 9-SH, 10-SH,** and **11**. ESI MS data for peptides **11-ox** and **12**.

#	*m/z* (monoisotopic)	
	Calculated	**Observed**
9	1568.9	1568.8
10	1740.1	1739.8
9-SH	1576.9	1577.0
10-SH	1748.0	1748.3
11	4234.3	4234.8
11-ox	8466.6	8466.6
12	8624.7	8624.7

9

10

10

10-SH

11

11-ox

12
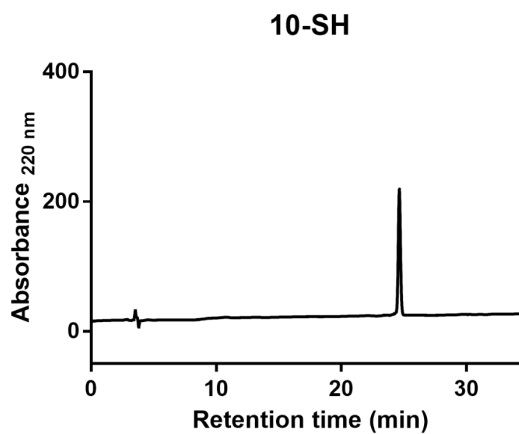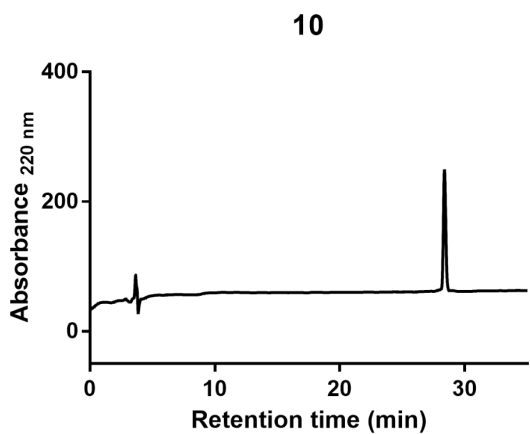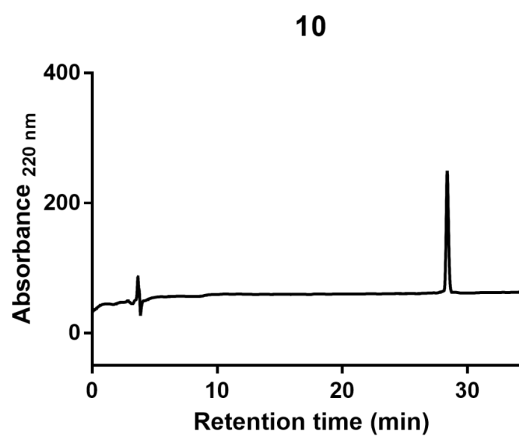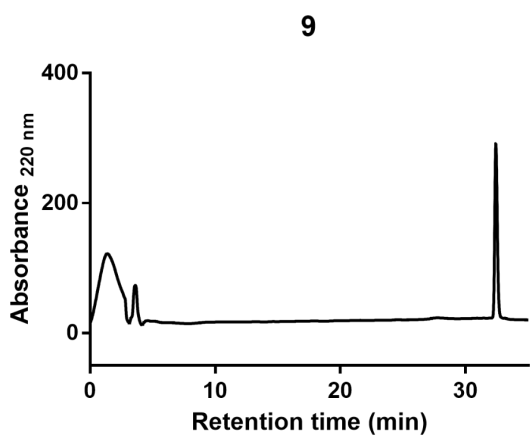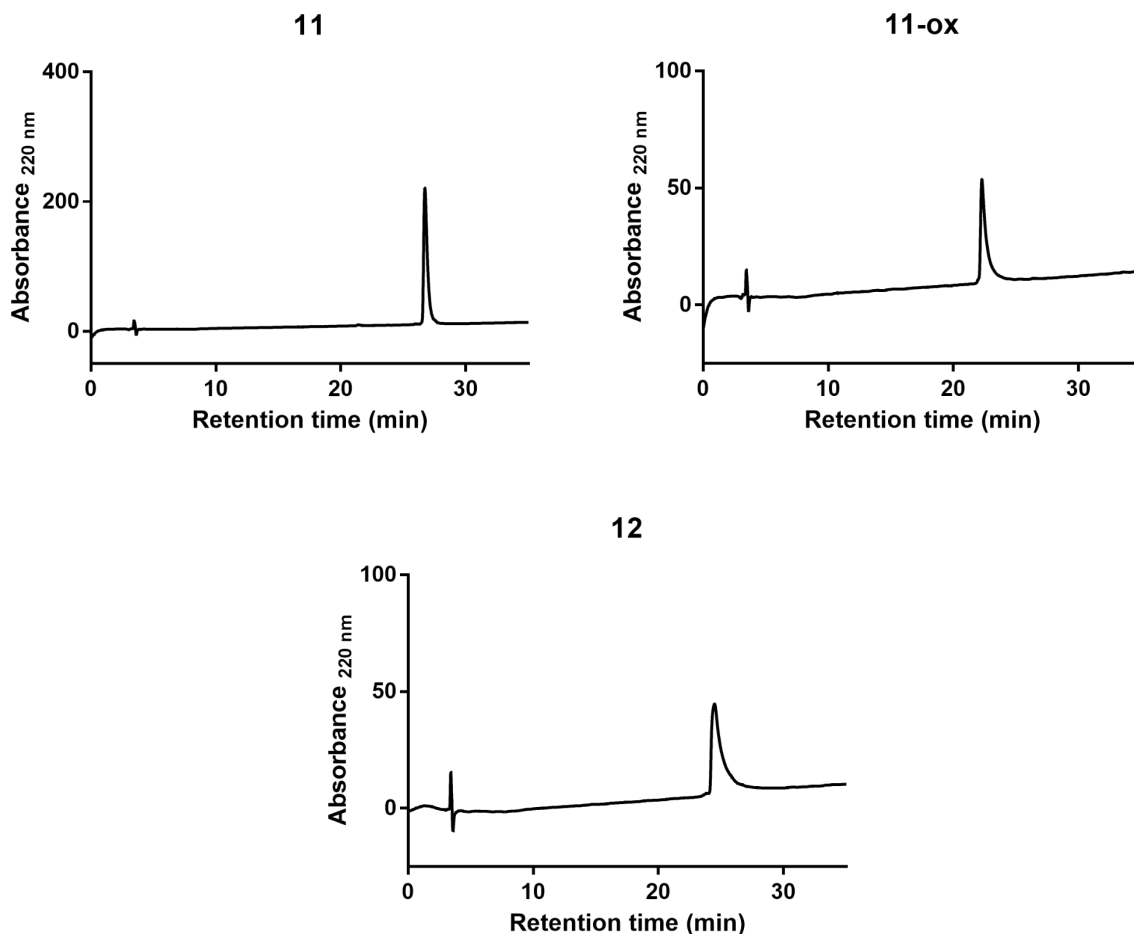
Figure 54. Analytical HPLC chromatograms of purified peptides **9, 9-SH, 10, 10-SH, 11, 11-ox,** and **12**.

Synthesis of Peptide 11-ox

A solution of **11** (200 μM) in ammonium carbonate buffer (10 mM, pH 8.1) was stirred open to the atmosphere at room temperature overnight. The reaction was quenched with a 20 % acetic acid solution to approximately pH 5. The product was purified via reverse phase HPLC (**Figure 54**). Peptide stock solution concentrations were quantified by UV spectroscopy (Hewlett-Packard 8452A diode array spectrometer, $\varepsilon276 = 3045$ cm^{-1} M^{-1} from two Tyr and one disulfide in each dimer).[181]

Synthesis of Peptide 12

Protocol adapted from literature.[171] To solution of **11** in water (final concentration of 150 μM in 24 mL total reaction volume) was added acetonitrile (2.4 mL), Tris HCl buffer (2.4 mL of 250 mM, pH 7.7; final concentration of 25 mM), and DBMPB linker in acetonitrile (1.2 mL of a 1500 μM stock; final concentration of 75 μM). The reaction was stirred under argon at room temperature overnight. The reaction was quenched by addition of 20 % acetic acid solution to approximately pH 5. The product was purified via reverse phase HPLC (**Figure 54**). Peptide stock solution concentrations were quantified by UV spectroscopy (Hewlett-Packard 8452A diode array spectrometer, $\varepsilon 276 = 3204$ cm^{-1} M^{-1} from two Tyr and one DBMPB linker in each dimer). The contribution from the DBMPB linker to the extinction coefficient of peptide **12** was determined through creation of a standard curve of control compound **15**, the slope of which was 304 ± 8 cm^{-1} M^{-1} (**Figure 55**).
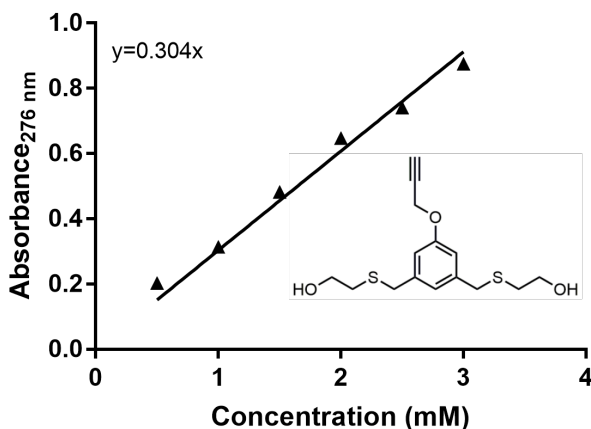
Figure 55. Absorbance at 276 nm of small molecule **15** as a function of concentration.

106

3.6.3 Small Molecule Synthesis
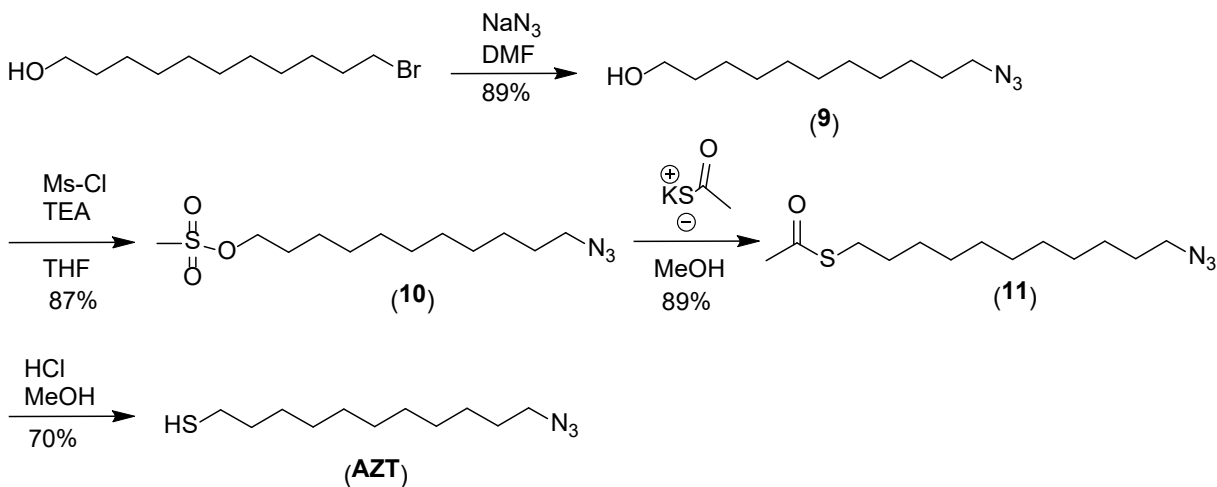
Figure 56. Synthesis of AZT using a previously published protocol.[182]

Synthesis of 11-azidoundecanethiol (AZT)

11-azidoundecanethiol was synthesized in four steps from 1-bromoundecan-11-ol using a previously published protocol.[182]
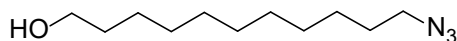
(1) Synthesis of 1-Azidoundecan-11-ol (9). 1-bromoundecanol (3.3 g, 13.1 mmol) and sodium azide (1.1 eq., 0.94 g, 14.4 mmol) were dissolved in DMF (50 ml) while stirring under a nitrogen atmosphere at ambient temperature. Once dissolved the reaction mixture was refluxed for 24 h. Upon completion, the reaction was cooled and quenched with water (50 ml). The reaction mixture was extracted with diethyl ether (3 x 20 ml) and the combined organic layers were washed with water (3 x 20 ml) and dried over MgSO$_4$. The solvent was removed under vacuum to give 2.5 g (89%) of product as a yellow oil. ^{1}H NMR (300MHz, CDCl$_3$) δ1.28 (16H, m), 1.57 (4H, m), 3.25 (2H, t, *J*= 6.9), 3.64 (2H, t, *J*= 6.6).
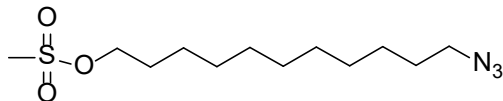
*(2) Synthesis of 1-Azidoundecan-11-methylsulfonate (**10**).* Methanesulfonyl chloride (2.4 ml, 31.6 mmol) was added to a solution of 1-azidoundecan-11-ol (2.5 g, 11.7 mmol) in anhydrous THF (87 ml). A solution of triethylamine (4.4 ml, 31.6 mmol) in anhydrous THF (13 ml) was added dropwise over 5 min. The reaction stirred at room temperature for 2 h before quenching with ice cold water (80 ml). The aqueous portion was washed successively with diethyl ether (2 x 35 ml). The combined organic layers were washed with 1M HCl, distilled water, saturated $NaHCO_3$ and again distilled water. The organic layer was dried over $MgSO_4$ and concentrated to give 3.0 g (87%) product as a yellow oil. ^{1}H NMR (300MHz, $CDCl_3$) δ1.28 (14H, m), 1.59 (2H, m), 1.74 (2H, m), 2.99 (3H, s), 3.24 (2H, t, *J*= 6.9), 4.21 (2H, t, *J*= 6.6).
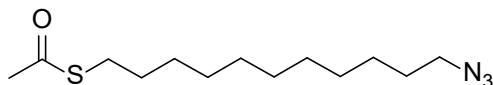
*(3) Synthesis of 1-Azidoundecan-11-thioacetate (**11**).* Potassium thioacetate (2.6 g, 22.8 mmol) and 1-azidoundecan-11-methylsulfonate (3.0 g, 11.4 mmol) were dissolved in methanol (100 ml). The solution was degassed for 15 min at room temperature before allowing to reflux under nitrogen for 3 h. After cooling, excess methanol was removed under vacuum before adding ice cold water (100 ml) to the flask. The mixture was extracted with diethyl ether (3 x 30 ml) and the combined organic layers were washed with water (3 x 30 ml). The organic layers were dried over $MgSO_4$ and concentrated to give 2.5 g (89%) product as a yellow oil. ^{1}H NMR (300MHz, $CDCl_3$) δ1.27 (14H, m), 1.57 (4H, m), 2.32 (3H, s), 2.86 (2H, t, *J*= 7.5), 3.25 (2H, t, *J*= 6.9).
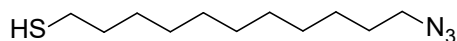
(4) Synthesis of 1-Azidoundecane-11-thiol (AZT). A solution of 1-azidoundecan-11-thioacetate (0.61 g, 2.23 mmol) in methanol (40 ml) was degassed for 15 min before adding concentrated HCl (2 ml, 65.2 mmol) and refluxing under nitrogen for 5 h. After cooling the reaction was quenched with water (10 ml) and extracted with diethyl ether (2 x 10 ml). The combined organic layers were washed twice with water, dried over MgSO$_4$ and concentrated to give 0.36 g (70%) product as a yellow oil. ^{1}H NMR (300MHz, CDCl$_3$) δ1.27 (16H, m), 1.57 (4H, m), 2.52 (2H, q, *J*= 7.2), 3.25 (2H, t, *J*= 6.9).
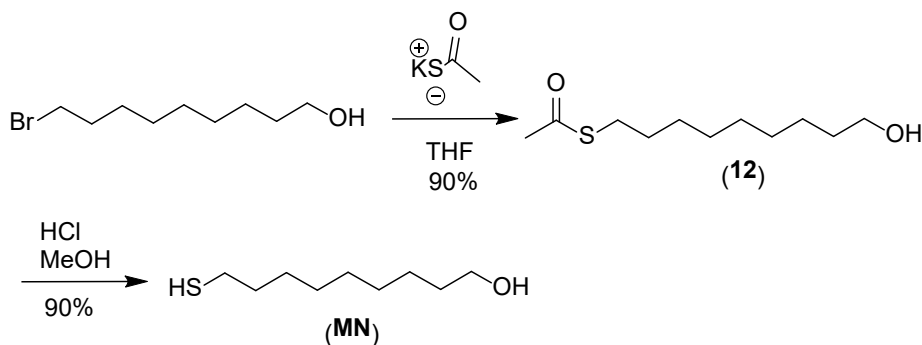
Figure 57. Synthesis of MN from a previously published protocol.[183]

Synthesis of 9-mercaptononanol (MN)

9-mercaptononanol was synthesized in two steps from 1-bromononan-9-ol using a previously published protocol.[183]
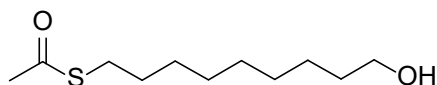
(1) Synthesis of S-(9-hydroxynonyl) ethanethioate (12). Potassium thioacetate (2.2 g, 19.1 mmol) was stirred in THF (35 ml) for 15 min before adding 1-bromononanol (2.4 g, 9.6 mmol). The reaction was stirred at ambient temperature overnight. The reaction was quenched with saturated NaHCO$_3$ (35 ml) and extracted twice with ethyl acetate. The

combined organic layers were washed with water and brine, dried over MgSO$_4$, and concentrated to give 2.1 g (90 %) product as a white powder. ^{1}H NMR (300MHz, CDCl$_3$) δ1.27 (16H, m), 1.56 (4H, m), 2.32 (3H, s), 2.86 (2H, t, J= 7.5), 3.64 (2H, t, J= 6.6).

HS‿‿‿‿‿‿OH
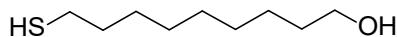
(2) Synthesis of 11-hydroxy-1-nonanethiol (MN). A solution of S-(9-hydroxynonyl) ethanethioate (2.1g, 9.7 mmol) in methanol (76 ml) was degassed for 15 min at 0°C before addition of concentrated HCl (16 ml). The reaction was stirred on ice for 3 h before being warmed to room temperature and stirred overnight. The reaction was quenched with saturated NaHCO$_3$ (35 ml) and extracted twice with ethyl acetate. The combined organic layers were washed with water and brine, dried over MgSO$_4$, and concentrated. The residue was purified via flash chromatography on silica gel, using 20% ethyl acetate in dichloromethane as the eluent, yielding 1.5 g (90%) product as a white solid. ^{1}H NMR (300MHz, CDCl$_3$) δ1.27 (16H, m), 1.56 (4H, m), 2.50 (2H, q, J= 7.5), 3.63 (2H, t, J= 6.6).
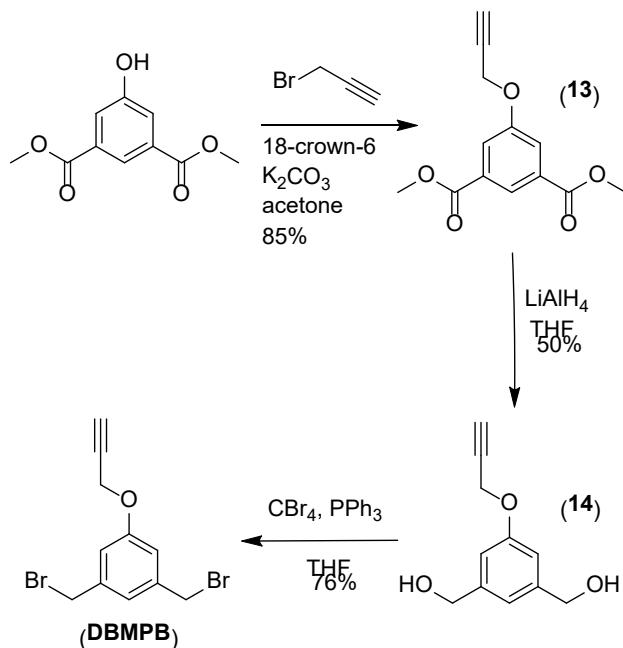
Figure 58. Synthesis of DBMPB linker, adapted from published protocols.[184-185]

Synthesis of 1,3- di(bromomethyl)-5-propargyloxybenzene (DBMPB)

1,3- di(bromomethyl)-5-propargyloxybenzene was synthesized in three steps from dimethyl 5-hydroxyisophthalate modified from previously published protocols.[184-185] A portion of this material was converted to **15** by double S_N2 displacement with β-mercaptoethanol.
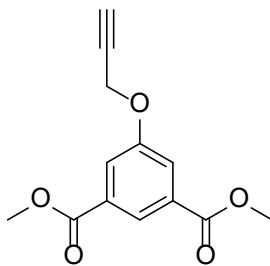
(1) Synthesis of dimethyl 5-proparyloxy isophthalate (13). To a 3-neck flask was added dimethyl 5-hydroxyisophthalate (1.0 g, 4.8 mmol), 18-crown-6 (13 mg, 0.049 mmol), potassium carbonate (0.80 g, 5.8 mmol) and acetone (20 ml). Propargyl bromide (80 wt% in toluene, 0.63 ml, 5.8 mmol) was carefully introduced via syringe through one of the side necks of the flask before bringing the reaction to reflux under a nitrogen atmosphere overnight. Once reaction completion was confirmed via TLC (1:1 ethyl acetate: hexanes), heat was removed, and the reaction was filtered, washing with additional acetone. The filtrate was evaporated to dryness. Purification of the crude product was achieved via recrystallization from ethanol which yielded 1.0 g (85%) of product as a white crystalline solid. ^{1}H NMR (300MHz, CDCl$_3$) δ2.53 (1H, t, J= 2.4), 3.93 (6H, s), 4.77 (2H, d, J= 2.4), 7.82 (2H, d, J= 1.5), 8.31 (1H, s).
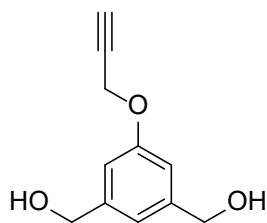
*(2) Synthesis of 1,3- dihydromethyl-5-proparyloxybenzene (**14**). <u>NOTE:</u> All glassware, including stir bar, was thoroughly dried in an oven and cooled in a desiccator prior to reaction set-up.* To a 3-neck flask lithium aluminum hydride (0.57 g, 15.0 mmol) was added and immediately placed under nitrogen. Anhydrous THF (40 ml) was added via syringe and the flask was cooled on an ice bath. In a separate flask, anhydrous THF (10 ml) was used to dissolve **13** (1.0 g, 4.0 mmol). This mixture was then added via syringe to the stirring 3-neck flask on ice. The reaction was stirred for approximately 20 minutes before replacing the ice bath with an oil bath and allowing the reaction to reflux overnight. The reaction cooled completely once no starting material remained according to TLC (1:1 ethyl acetate: hexanes). The reaction was quenched by addition of a saturated ammonium hydroxide solution until H_2 evolution ceased. HCl solution (1.0 M) was added until the pH reached 7. The reaction was then filtered, washing with THF, and the filtrate was evaporated to dryness. The crude product was recrystallized from 1:1 ethyl acetate: hexanes resulting in 384 mg (50%) of a white crystalline solid. ^{1}H NMR (300MHz, CDCl$_3$) δ2.51 (1H, t, *J*= 2.4), 4.68 (4H, s), 4.71 (2H, d, *J*= 2.4), 6.92 (2H, s), 7.00 (1H, s).

112
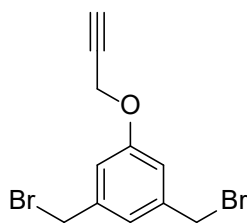
(3) Synthesis of 1,3- di(bromomethyl)-5-propargyloxybenzene (DBMPB). A solution of triphenylphosphine (1.34 g, 5.1 mmol) dissolved in anhydrous THF (2 ml) was added via syringe to a solution of 1,3- dihydromethyl-5-proparyloxybenzene (384 mg, 2.0 mmol) and tetrabromomethane (1.69 g, 5.1 mmol) in anhydrous THF (8 ml). The reaction was stirred under nitrogen at ambient temperature for 30 minutes before evaporating to dryness. Flash chromatography on silica gel using dichloromethane as the eluent was performed followed by a second column to remove remaining triphenylphosphine oxide. The second purification employed a gradient of 0 - 4 % ethyl acetate in hexanes as the eluent. This produced 479 mg (76%) pure product as a white powder. ^{1}H NMR (300MHz, CDCl$_3$) δ2.54 (1H, t, *J*= 2.4), 4.44 (4H, s), 4.71 (2H, d, *J*= 2.4), 6.94 (2H, d, *J*= 1.2), 7.05 (1H, s).
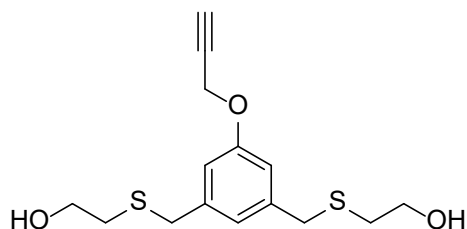
Synthesis of 2,2'-(((5-(prop-2-yn-1-yloxy)-1,3-phenylene)bis(methylene))bis (sulfanediyl))bis(ethan-1-ol) (15)

2-mercaptoethanol (73.2 μl, 1.04 mmol, 2.2 equiv.) was added to a solution of DBMPB (150 mg, 0.472 mmol) and potassium carbonate (287 mg, 2.08 mmol, 4.4 equiv.) in anhydrous dichloromethane (2.0 ml) and stirred for 2 days at room temperature. The reaction was filtered, washing with dichloromethane, and the filtrate was evaporated. The crude product was purified

via column chromatography on silica using 10% hexanes in ethyl acetate as the eluent. The pure product was dried under vacuum to give an off-white pellet (66 mg, 45%). ^{1}H NMR (300MHz, CDCl$_3$) δ2.53 (1H, t, J= 2.4), 2.63 (4H, t, J= 6.0), 3.64 (4H, t, J= 6.0), 3.68 (4H, s), 4.70 (2H, d, J= 2.4), 6.84 (2H, d, J= 1.2), 6.92 (1H, s). ^{13}C NMR (400MHz, CDCl$_3$) δ34.35, 35.79, 55.84, 60.42, 75.77, 78.35, 114.22, 122.60, 140.21, 157.91. HRMS (m/z): calculated: 312.0854; found: 312.0823.
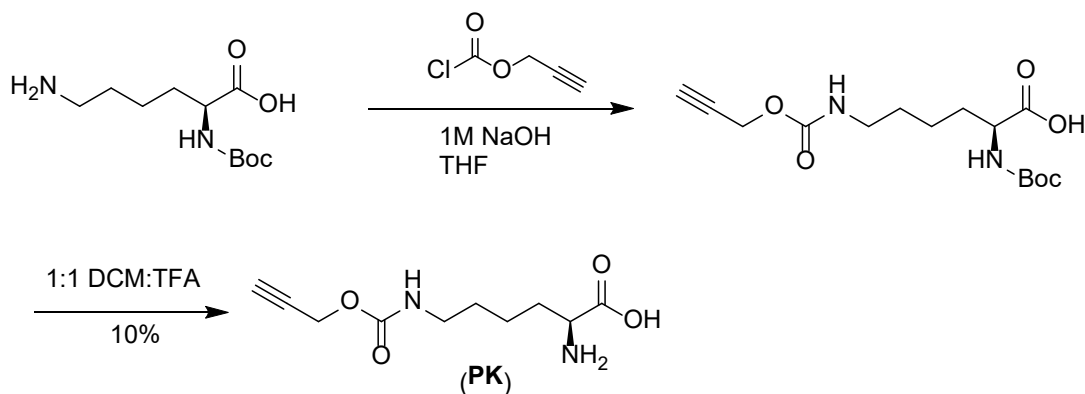
Figure 59. Synthesis of PK adapted from a previously published protocol.[186]

Synthesis of propargyl lysine (PK) monomer

Propargyl lysine was synthesized in two steps from Boc-(L)-Lys-OH adapted from a previously published protocol.[186]
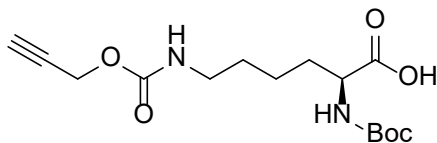
(1) Synthesis of Boc-propargyl–(L)-lysine (16). A solution of Boc-(L)-lysine-OH (6.0 g, 24.4 mmol) was dissolved in NaOH (1.0 M, 60 ml) and THF (60 ml) and cooled to 0˚C on an ice bath. Propargyl chloroformate (1.9 ml, 19.5 mmol) was added dropwise via syringe over 5 minutes. The ice bath was removed and the reaction was allowed to warm to room temperature and stir overnight. After cooling back down to 0˚C, diethyl ether (200 ml) and

HCl (1.0 M, 200 ml) were added. The organic layer was extracted with ethyl acetate (3 x 50 ml). The combined organic layers were dried over anhydrous sodium sulfate followed by evaporation of the solvent. This yielded a sticky, foamy residue that was immediately taken forward into the deprotection step.
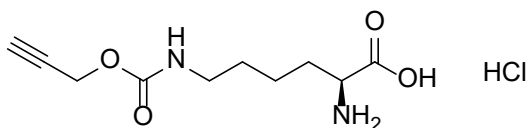
(2) Synthesis of propargyl-(L)- lysine (PK). Boc propargyl-(L)-lysine (5.33 g, 16.2 mmol) was dissolved in dry dichloromethane (50 ml) and trifluoroacetic acid (50 ml). The reaction was allowed to stir at ambient temperature for 1 hour before evaporation of the solvents resulting in a crude brown oil. Cold diethyl ether (150 ml) was poured over the product portion wise. The ether was then decanted into falcon tubes and centrifuged to collect the suspended white precipitate. The ether was decanted and the remaining white solid was dissolved in 1:1 water: acetonitrile and lyophilized. The lyophilized powder was re-suspended in a 5 mM HCl solution (10 ml), frozen and lyophilized again to exchange remaining TFA salt with HCl. This process was repeated three times giving the product (370 mg, 10%) as a white flaky solid. ^{1}H NMR (300MHz, D$_2$O) δ1.50 (4H, m), 2.91 (1H, m), 3.16 (2H, t, *J*= 6.6), 3.82 (1H, t, *J*= 6.0), 4.67 (2H, s). HRMS (*m/z*): calculated: 229.11828; found: 229.11877.

3.6.4 Mixed Self-Assembled Monolayer Formation

Mixed alkanethiol self-assembled monolayers were prepared from a 1.0 mM total thiol concentration solution in ethanol that contained the desired ratio of individual alkanethiols (either

decanethiol, 9-mercaptononanol, or 11-mercaptoundecanoic acid and 11-azidoundecanethiol). Substrates consisted of gold metal deposited on glass (Thermo Scientific BioGold substrates produced by Electron Microscopy Sciences), typically cut to size 1.9 cm x 1.3 cm for PM-IRRAS measurements and 0.5 cm x 0.5 cm for BAP bioactivity assays. Prior to SAM formation, substrates were cleaned via a 10 min sonication in ethanol followed by substantial washing with ethanol. After cleaning, the substrates were submerged into the mixed alkanethiol solution for 24 h at room temperature protected from light. The substrates were then taken out of the solution, rinsed thoroughly with ethanol, DCM, and water. Substrates for PM-IRRAS or contact angle analysis were dried under N_2, covered with aluminum foil, and placed in a desiccator for at least 30 min prior to analysis. Samples not measured immediately were stored in a desiccator, protected from light exposure.

3.6.5 Surface Copper Catalyzed Click Reactions with Small Peptides

A gold substrate bearing a mixed alkanethiol SAM was placed in a septa sealed scintillation vial under a bed of argon gas. To an epitube containing an aqueous solution of peptide alkyne (1.0 μmol), was added a bright blue solution of copper (II) sulfate (2.0 μmol, 2 equiv.; 12.5 μl of a 160 mM stock in water) and tris-hydroxypropyltriazolylmethylamine (THPTA) (2.0 μmol, 2 equiv.; 54.3 μl of a 36.8 mM stock in water). This solution was vortexed and added via syringe into the argon purged vial. Fresh sodium ascorbate (4.0 μmol, 4 equiv.; 39.6 μl of a 100 mM stock in water) was added via syringe to the vial and swirled (total reaction volume 1200 μl). The reaction was allowed to sit at room temperature, covered from light overnight. The reacted monolayers were rinsed with water and sonicated for 10 min in a 1.0 M solution of EDTA in water (10 ml). The gold slides were rinsed with water again, then sonicated in water for 30 min. The

slides were then rinsed with water and ethanol followed by a final sonication for 10 min in ethanol. Finally, the SAMs were washed with water and dried with a stream of N_2. Samples were stored in a vacuum desiccator, protected from light exposure until measurements were completed.

3.6.6 Surface Copper Catalyzed Click Reactions with BAP Enzymes

K39PK BAP surfaces were prepared by placing a mixed alkanethiol SAM into an eptiube containing the following reaction mixture (500 μl) added in the indicated order: 0.5% wt/v BSA solution, BAP enzyme (0.5 nmol), then copper sulfate (0.8 μmol,; 5.2 μl of a 160 mM stock in water) and THPTA (0.8 μmol,; 22.6 μl of a 36.8 mM stock in water). Sodium ascorbate (1.7 μmol,; 16.5 μl of a 100 mM stock in water) was added last and argon gas was blown over the epitube before sealing. The reaction was allowed to sit at room temperature, covered from light, overnight. The reacted monolayers were rinsed with water and sonicated for 30 min in 0.4 M Tris HCl buffer with 10 mM $MgCl_2$ (pH 8.2, 1 ml). This buffer was then exchanged for fresh buffer and the surfaces were sonicated for another 30 min.

3.6.7 Contact Angle Goniometry

Substrates for contact angle measurements were made by Nathaniel Miller. Silicon oxide substrates were purchased from Fisher Scientific and used after UV ozone cleaning. A 10 nm titanium adhesion layer with a 100 nm gold surface were deposited *via* evaporation from 0.9999 pure ingots using a Plassys electron beam evaporator model MEB550S. Evaporation conditions used were a chamber pressure of 1×10^{-7} mBarr and an evaporation rate within 10 percent of the desired deposition rate set point, 0.02 nm/s for titanium and 0.05 nm/s for gold. Additionally,

substrates were rotated at 1 rpm to enhance film uniformity. Once completed substrates were stored under vacuum to limit contamination until use.

Self-assembled monolayers were formed on these silicon-gold substrates using the same procedure for forming mixed SAMs, detailed above. Water contact angles were determined on a VCA Optima from AST Products, Inc. at room temperature. Contact angles were measured from sessile drops of 18 Ω water by lowering 2 μl drops suspended from a blunt tip syringe onto the surface. Error bars represent the average of three drops measured on each substrate.

3.6.8 Circular Dichroism

CD measurements were performed on an Olis DSM17 circular dichroism spectrophotometer. Scans were performed at 20 °C from 200 to 260 nm with 1 nm increments, a bandwidth of 2 nm, and a 5 s integration time. Cells with a 2 mm path length were used. Peptide solutions (50 μM as determined by UV absorbance) were prepared in 10 mM phosphate buffer (pH 7.0).

Thermal melts of peptides **11-ox** and **12** were collected with 1 increment from 220 to 260 nm with a 3 s integration time. Data was recorded every 2 °C from 4-98 °C after a 2 min equilibration time at each temperature. Cells with a 2 mm path length were used. Peptide solutions (50 μM as determined by UV absorbance) were prepared in 10 mM phosphate buffer (pH 7.0).

3.6.9 Solution Fourier Transform Infrared Spectroscopy

Spectra were collected on a Bruker Vertex-70LS FTIR that was purged with N_2 gas for at least 30 min prior to taking measurements. A liquid cell with CaF_2 windows and a 50 μm spacer was assembled. The empty cell was used as the reference. The cell was thoroughly cleaned with methanol and dried with N_2 before each measurement. Lyophilized peptide powder was exchanged three times by adding 5 mM HCl solution in water (1 mL × 3) and lyophilizing to remove interfering TFA salts. Peptide solutions (~5 mg/mL in D2O) were measured with 1000 scans, a 3 mm aperture, and a resolution of 4 cm^{-1} collected over a range of 500−4000 cm^{-1}. Raw data for each sample were collected as a transmission spectrum, corrected by subtraction of a blank (D_2O) transmission spectrum, converted to absorption, and smoothed.

3.6.10 Polarization-Modulated Infrared Reflection−Absorption Spectroscopy

PM-IRRAS spectra were collected on a Thermo Fisher Nicolet iS50 FTIR spectrometer equipped with a liquid nitrogen cooled MCT-A detector. The interferogram was automatically aligned using the "align" function prior to collection. The physical sample alignment was found to be highly important for collection of high quality and reproducible spectra. Gold substrates were attached to a glass microscope slide using double-sided copper tape and the slide was aligned using the rotation, tilt, and mirror adjustment levers so that the interferogram intensity was maximized in "sum" mode (rough max of 5.0-6.5). (_NOTE:_ This max value may be hard to reach until the box is fully purged with nitrogen). The gain is chosen by looking at the "dual channel polarization modulation window"; the input gain should be maximized at 10 and the output gain (typically 1

or 2) was chosen by picking a gain value that maximizes channel B, without overtaking the maximum of channel A.

PM-IRRAS spectra were collected with a 30 min acquisition time (3000 scans) and a resolution of 4 cm^{-1} at an incidence angle of 80°. The PEM wavelength was centered at either 2100 cm^{-1} or 1600 cm^{-1} to get enhanced signal in the azide and amide region, respectively. The step size was 0.5 λ. Atmospheric correction was applied to all spectra. Baseline correction was carried out using the previously reported arPLS method.[172] A lambda smoothness parameter of 10^6 and a polynomial order of 3 was used. Regions of interest, where the baseline is expected to have no signal, were defined as [960, 1031], [1248, 1256], [1285, 1295], and [1750, 2800].

3.6.11 Bacterial Alkaline Phosphatase (BAP) Activity Assay

BAP exposed surfaces were placed in a 24-well plate containing 0.2 M Tris HCl buffer with 5 mM $MgCl_2$ (pH 8.2) and 10 mM PNPP substrate (1.5 mL per well). The plate was covered with foil to limit light exposure and lightly swirled for 6 hours. Aliquots of 25 μl from each well were removed every 30 min and placed in a 384 well plate (Corning, flat white with clear bottom). After a 5 second shake, the absorbance at 405 nm of each well was recorded on a Tecan infinite M1000Pro plate reader. The pathlength of the well was determined by measuring the absorbance of the assay buffer with 10 mM PNP in a plastic cuvette with a 10 mm pathlengh at 975 nm and 900 nm and performing a subtraction of $A_{975cuvette}$ - $A_{900cuvette}$ to yield a K-factor reference value of 0.1773. Assay buffer with 10 mM PNP (25 μl) was then added to 3 wells and the average absorbance at 975 nm and 900 nm was obtained. Well pathlength was then calculated via the equation: pathlength = [$A_{975well}$ - $A_{900well}$/K-factor]*10 mm, following a known protocol.[187]

Reaction velocity was calculated by dividing the slope of the Absorbance$_{405\text{ nm}}$ vs. time by the extinction coefficient of PNP (18000 M^{-1} cm^{-1}) multiplied by the pathlength (1.8 mm).
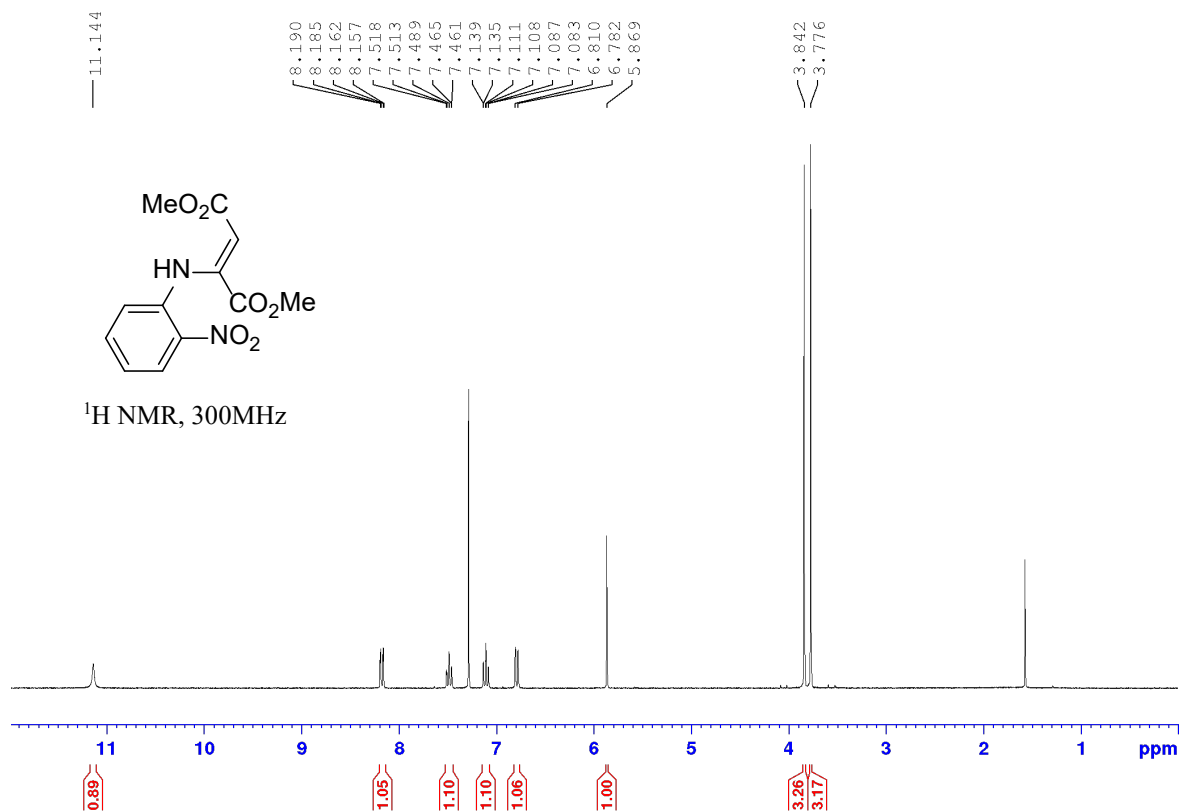
Figure 60. ^{1}H NMR spectrum of compound **1**.
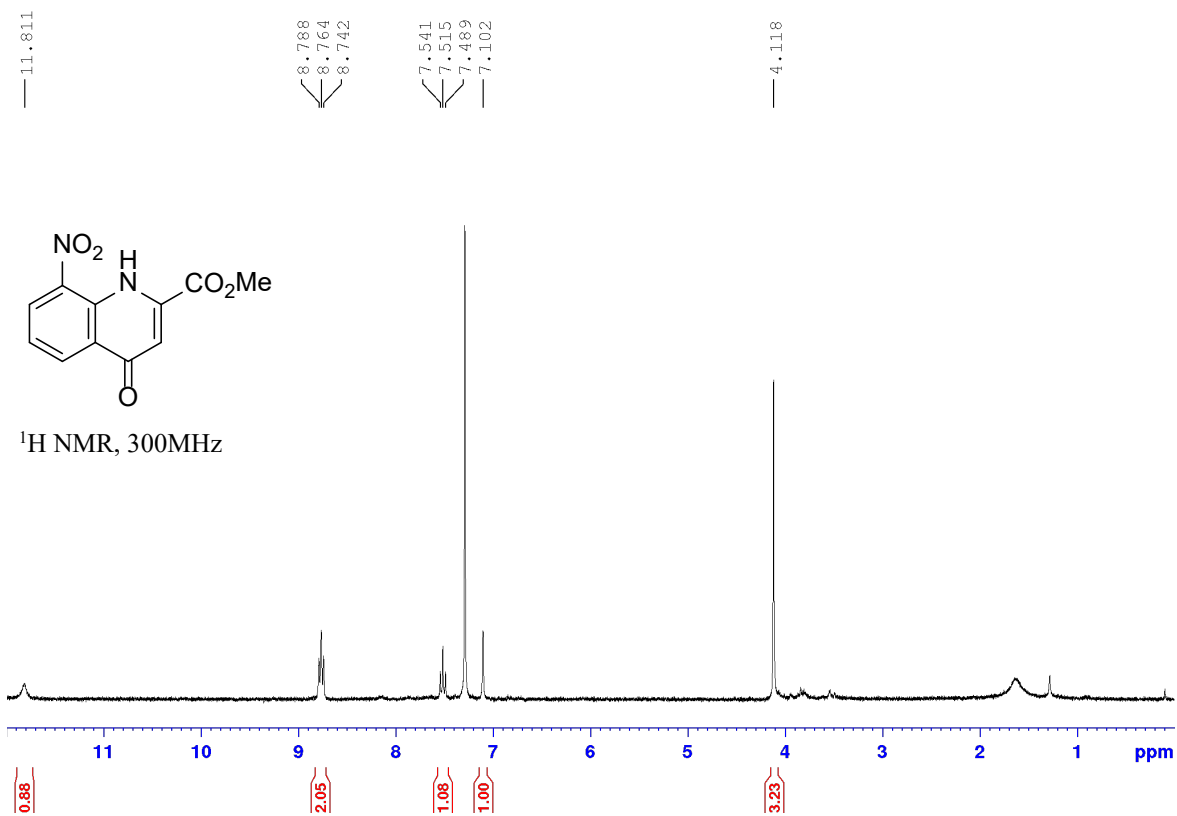
Figure 61. ^{1}H NMR spectrum of compound **2**.

NO$_2$

N

CO$_2$Me

OiBu

^{1}H NMR, 300MHz
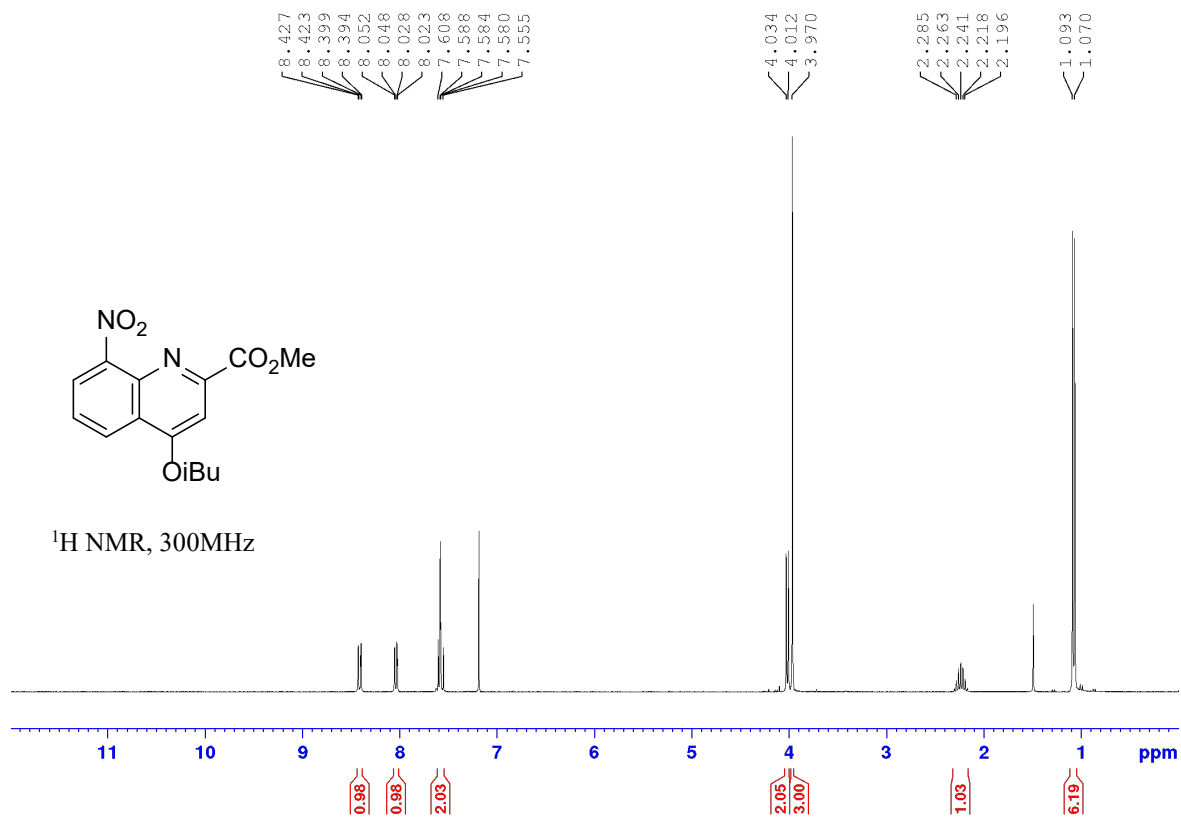
Figure 62. ^{1}H NMR spectrum of compound **3a**.
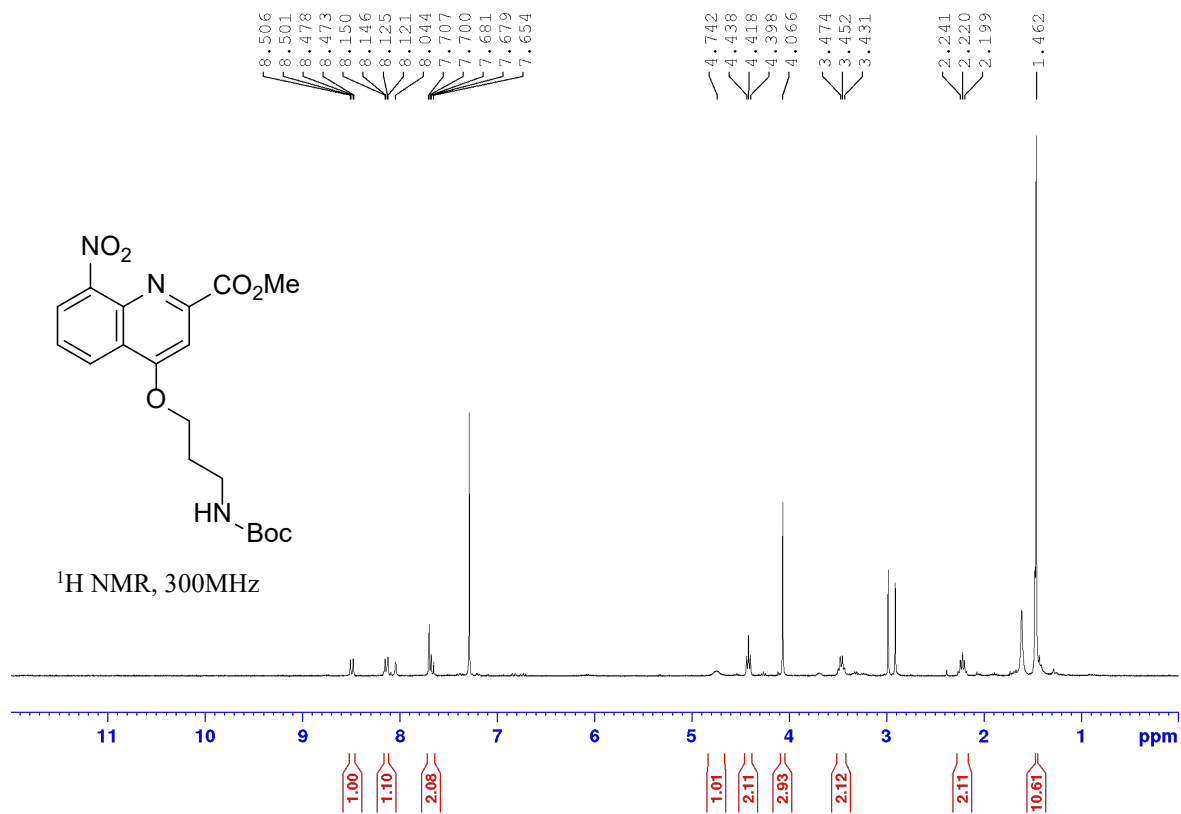
Figure 63. ^{1}H NMR spectrum of compound **3b**.
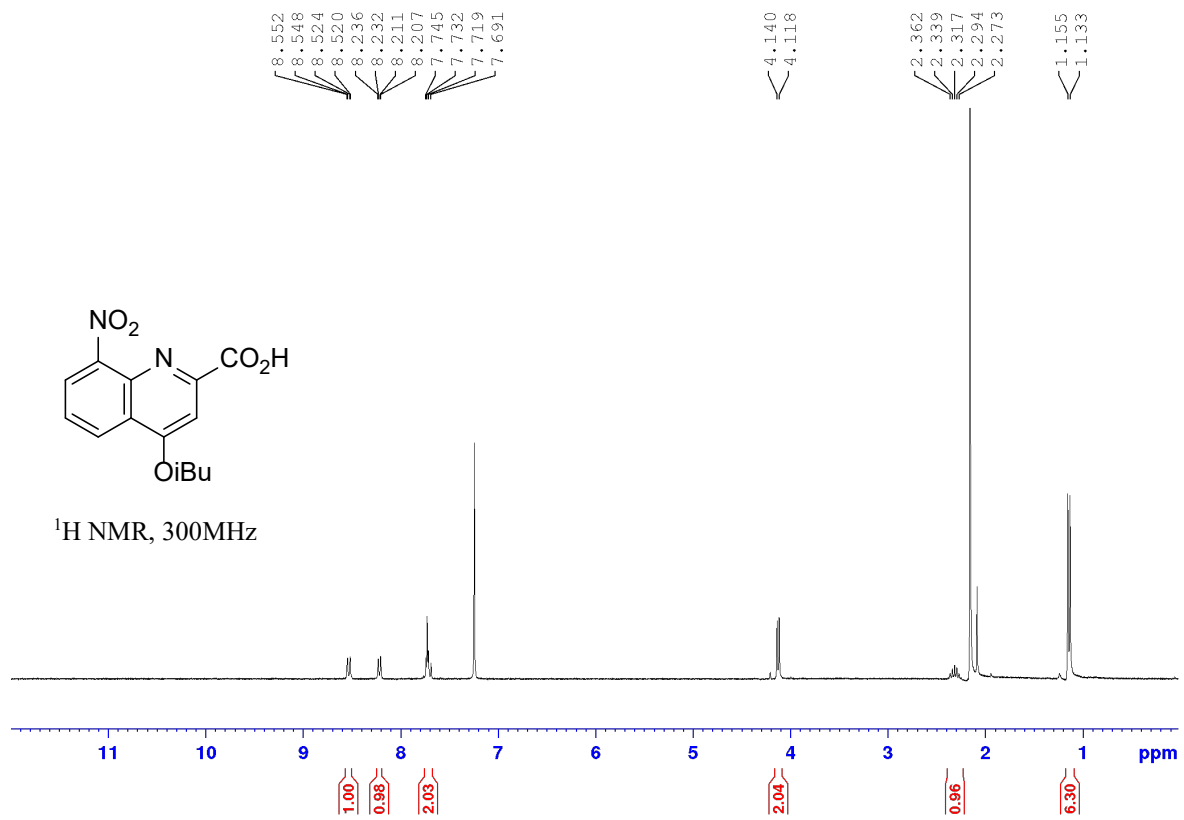
Figure 64. ^{1}H NMR spectrum of compound **4a**.
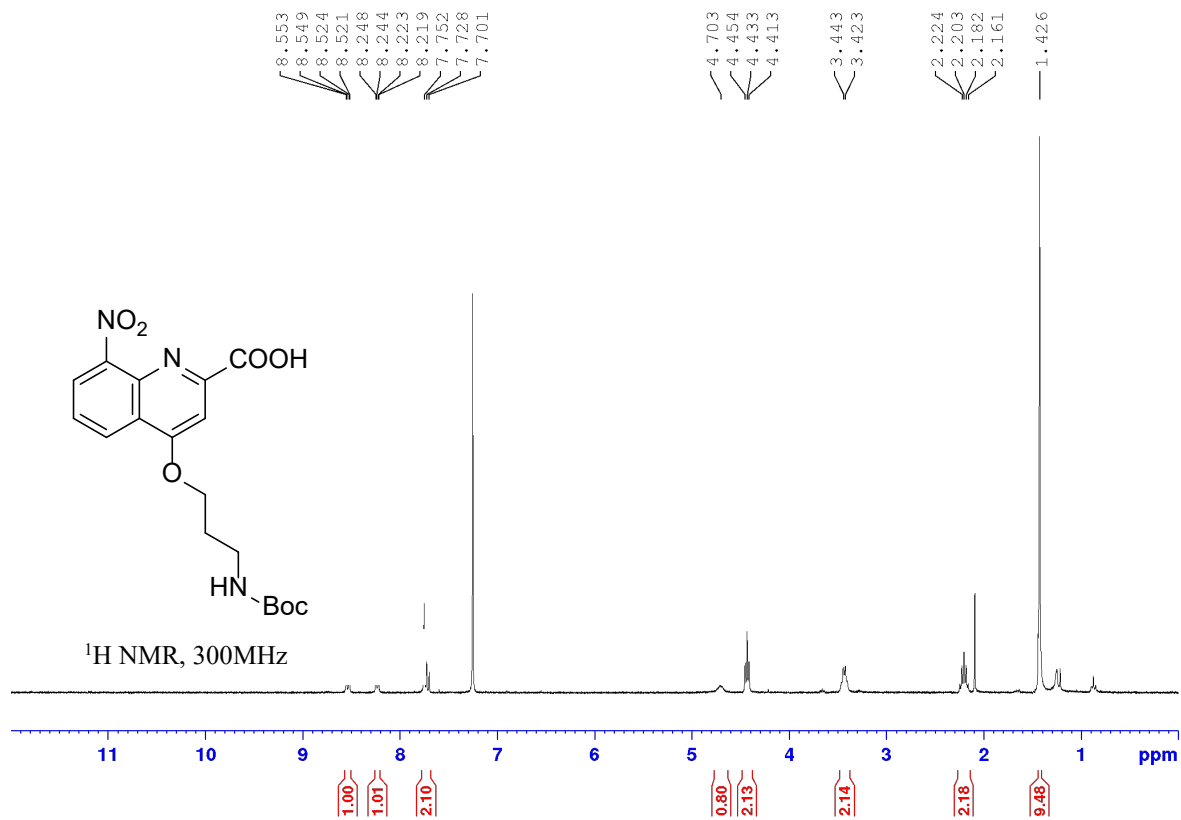
Figure 65. ^{1}H NMR spectrum of compound **4b**.
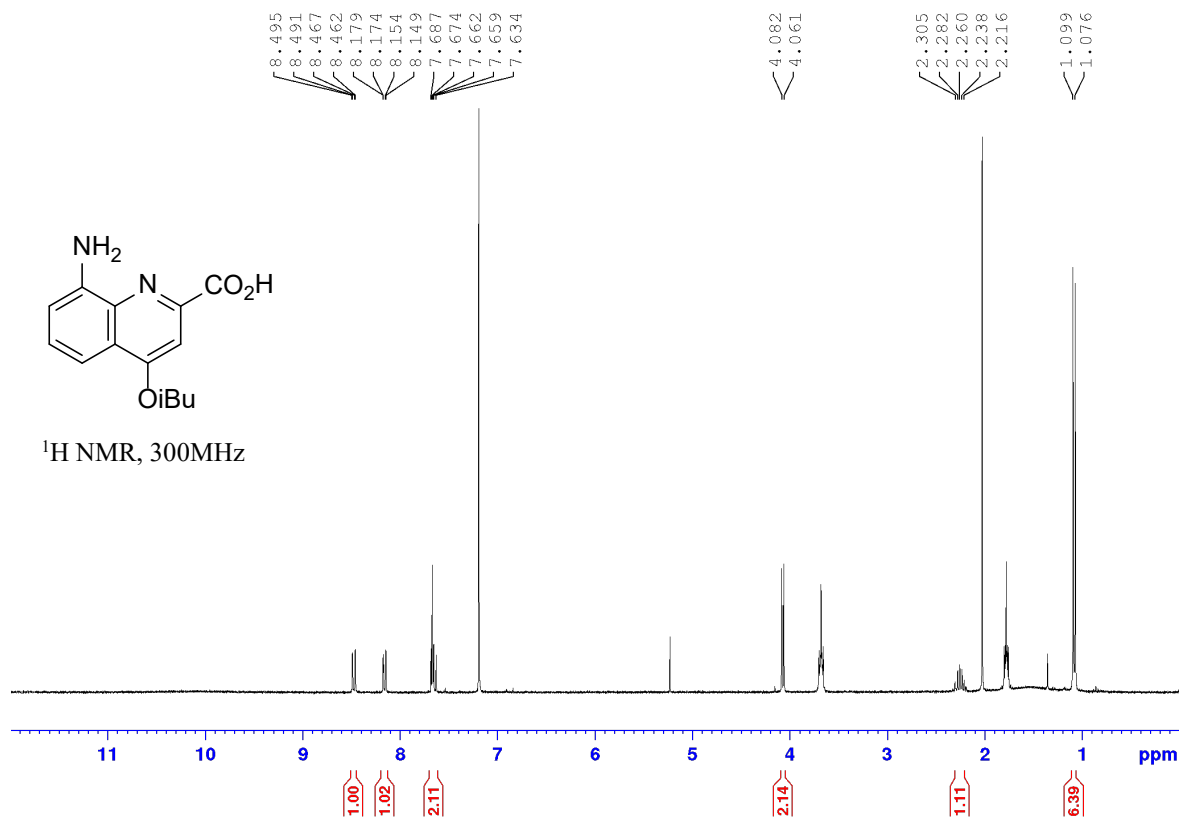
Figure 66. ^{1}H NMR spectrum of compound **5a**.
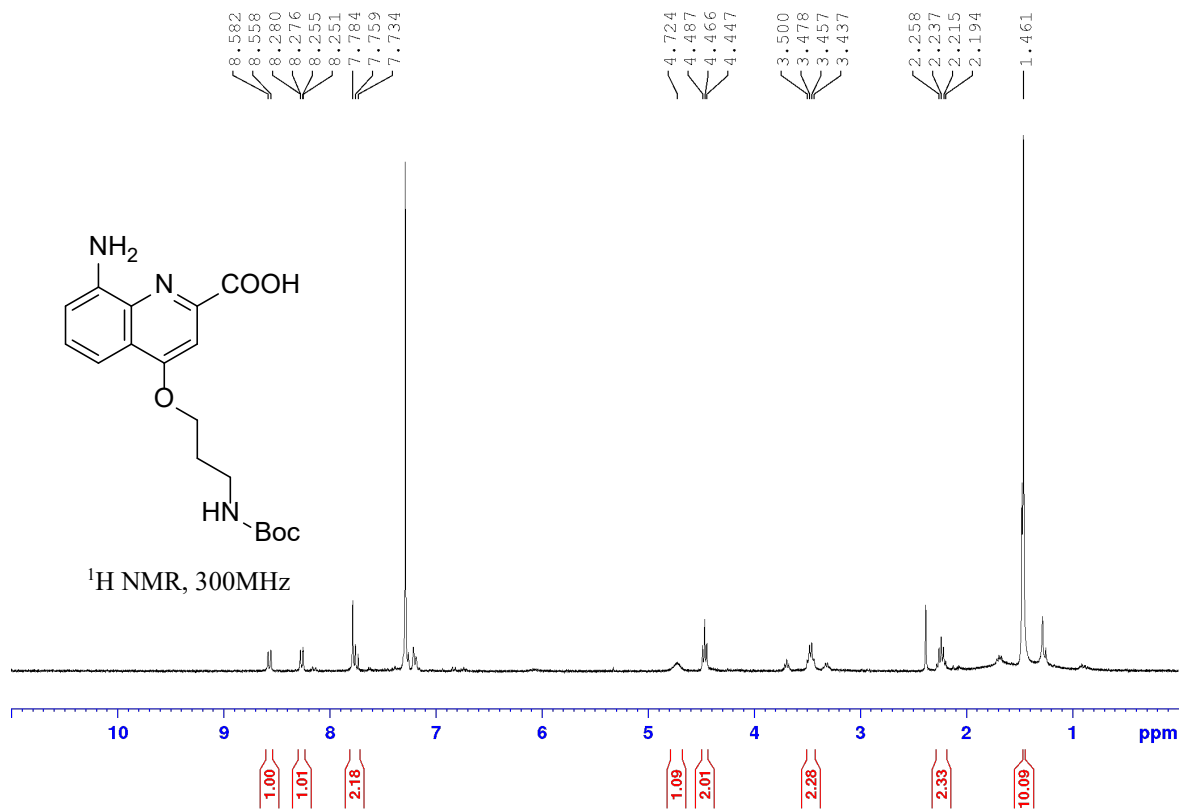
Figure 67. ^{1}H NMR spectrum of compound **5b**.
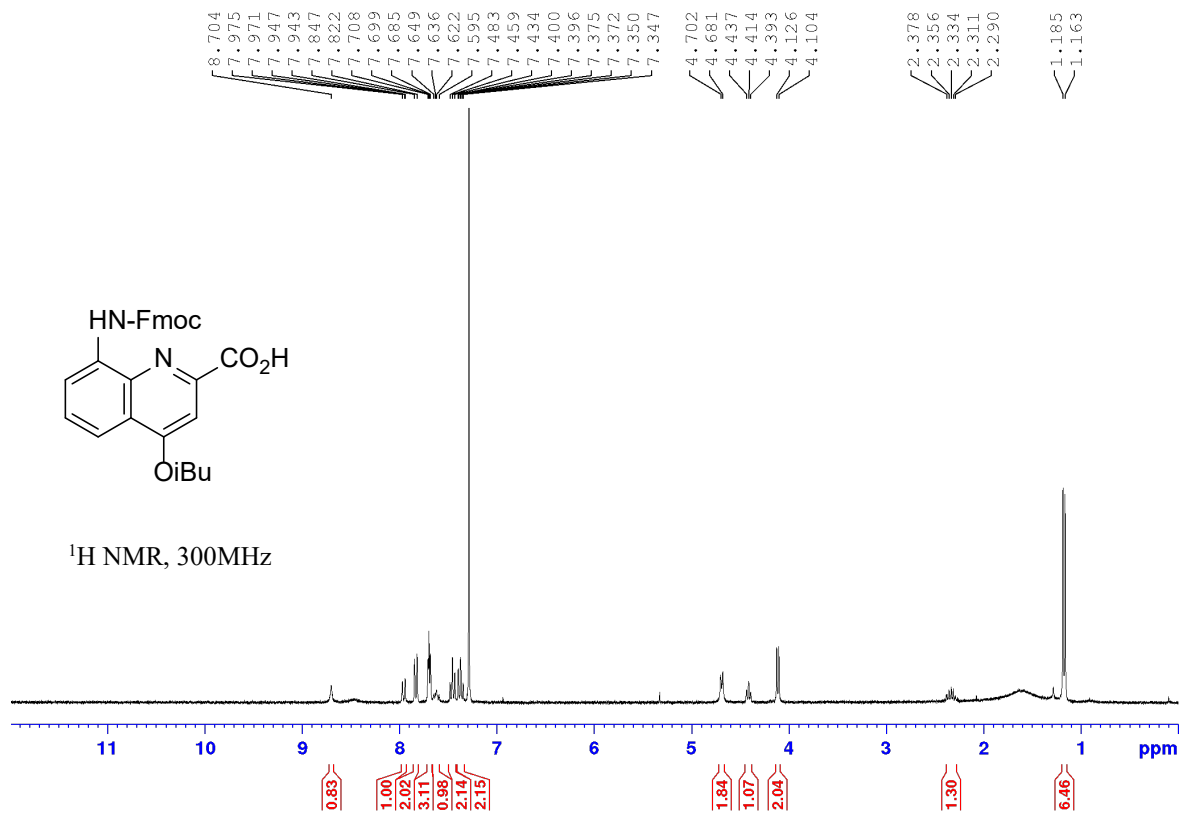
Figure 68. ^{1}H NMR spectrum of compound **6a**.
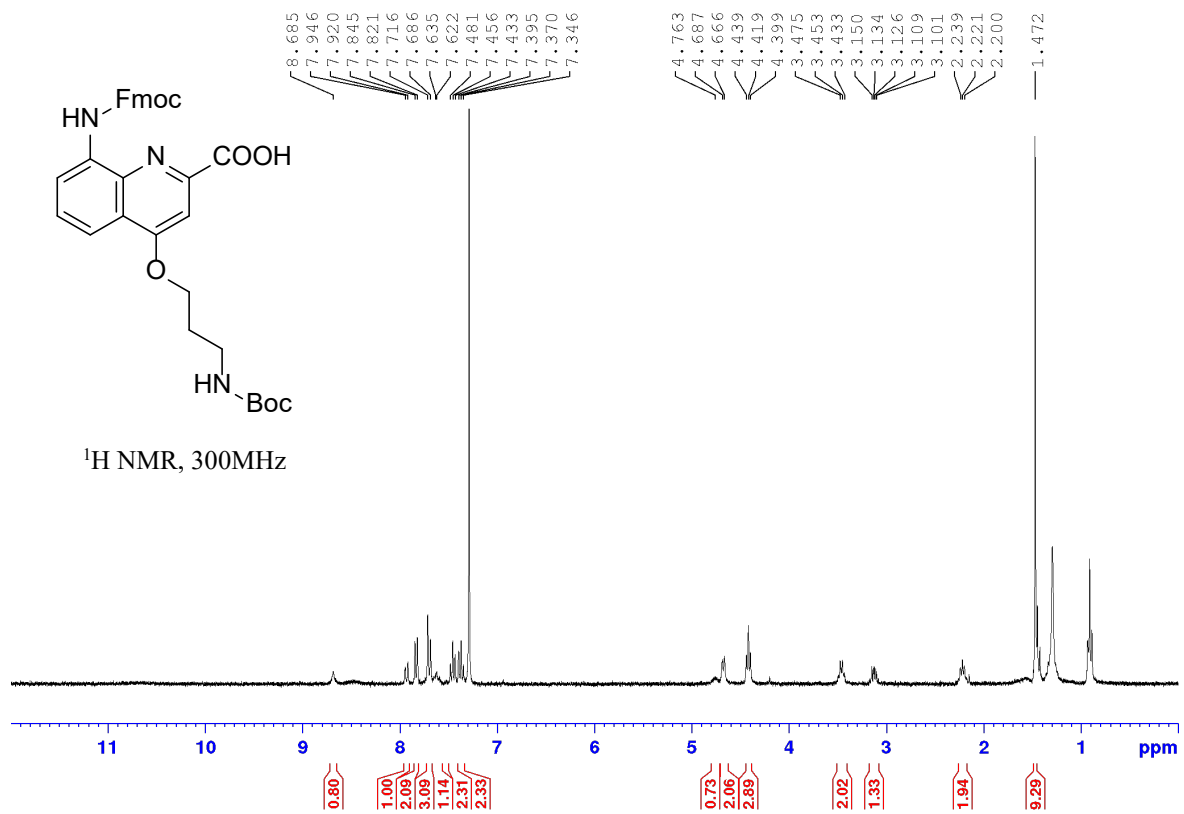
Figure 69. ^{1}H NMR spectrum of compound **6b**.
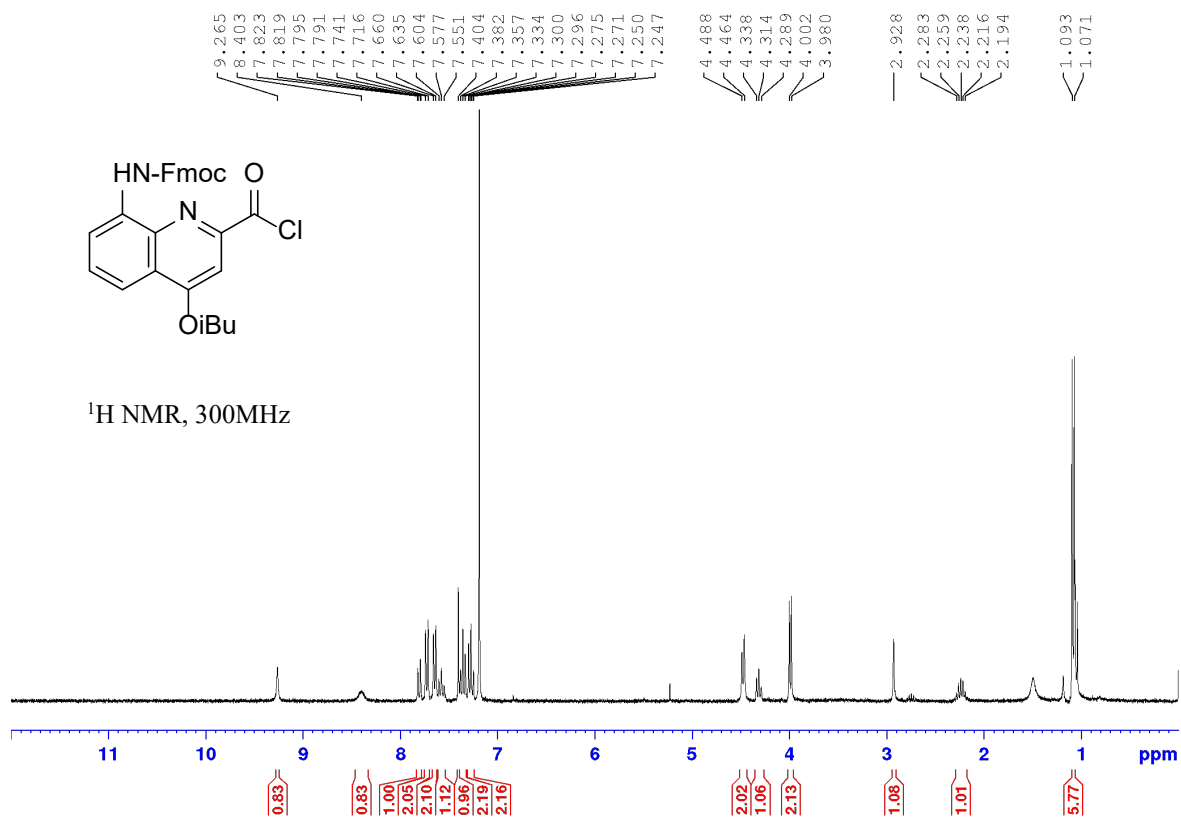
Figure 70. ^{1}H NMR spectrum of compound **7a**.

^{1}H NMR, 300MHz
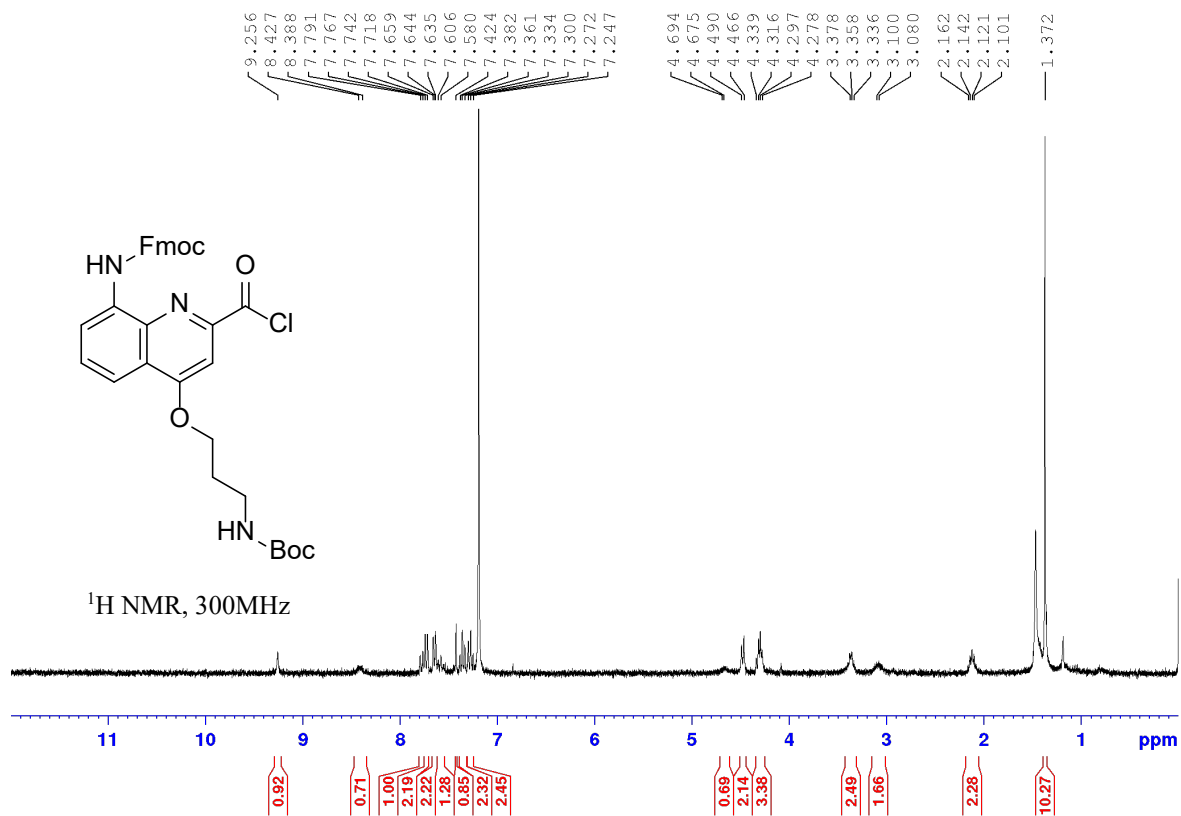
Figure 71. ^{1}H NMR spectrum of compound **7b**.
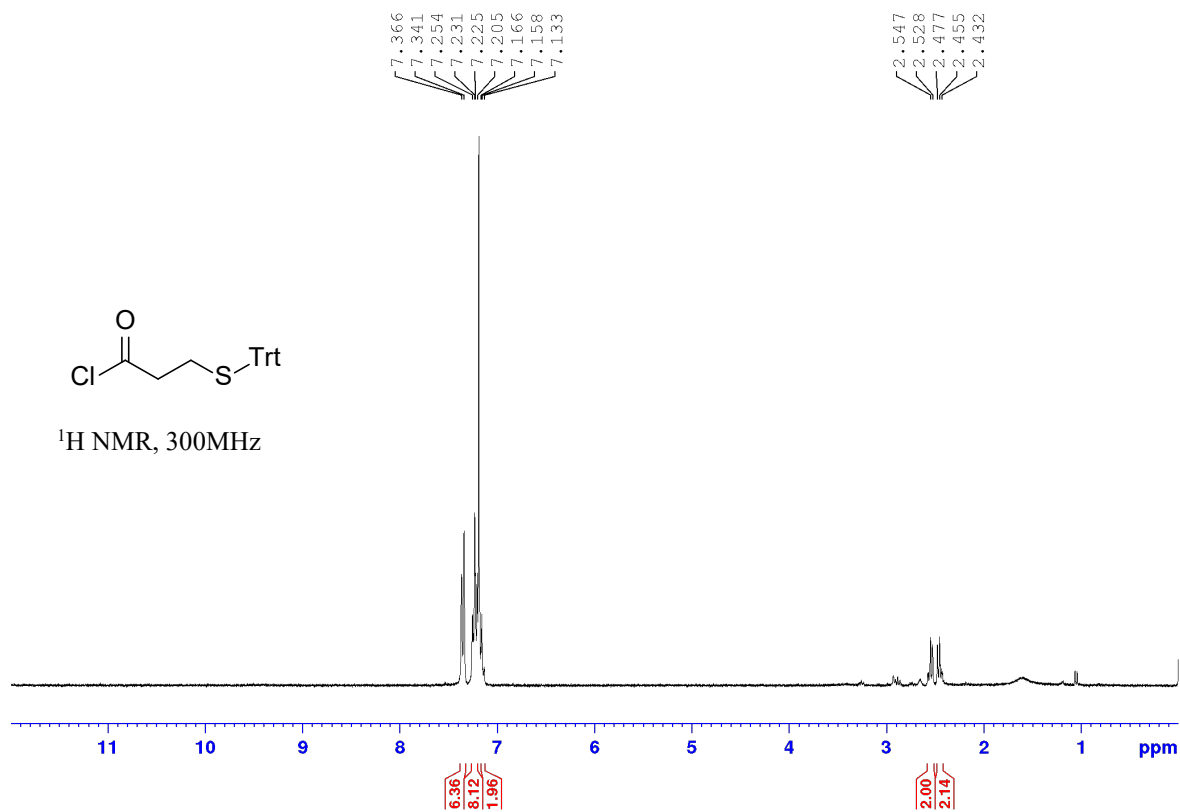
Figure 72. ^{1}H NMR spectrum of compound **8**.
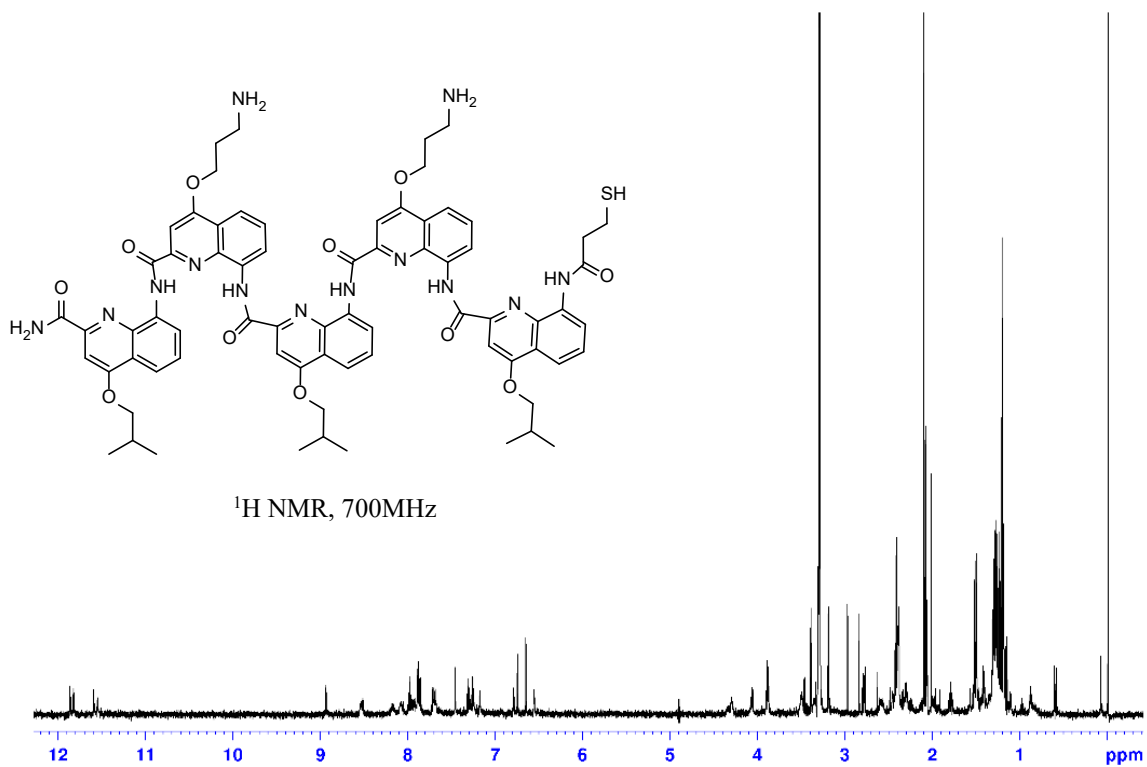
Figure 73. ¹H NMR spectrum of foldamer **8**.
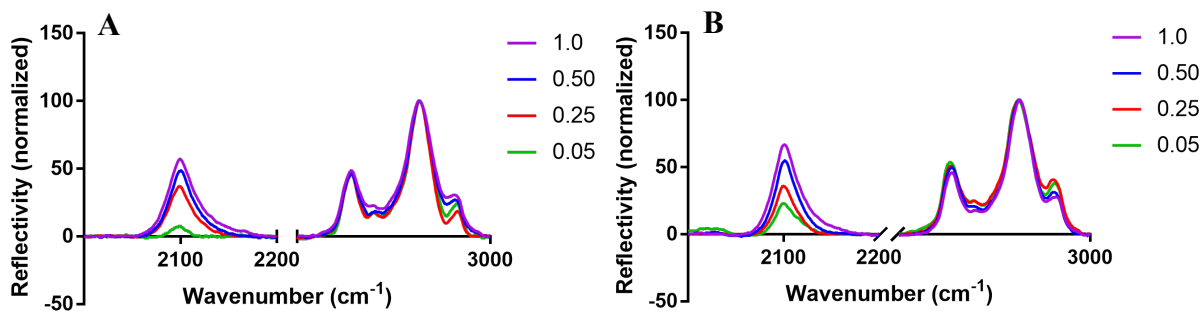
Figure 74. Representative PM-IRRAS spectra of mixed monolayers resulting from various deposition solution fractions of AZT with background alkanethiol (A) MN and (B) MUA.
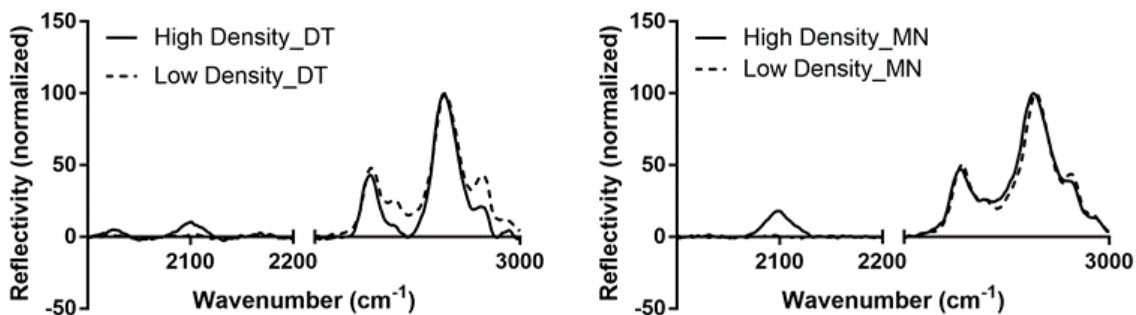
Figure 75. Representative PM-IRRAS spectra for mixed DT:AZT and MN:AZT surfaces displaying the CH$_2$ and azide regions after copper-catalyzed click reactions were performed. High density surfaces are those with a surface AZT fraction above the steric limit (0.70 mole fraction) and low density surfaces are those below 0.20 surface mole fraction AZT.
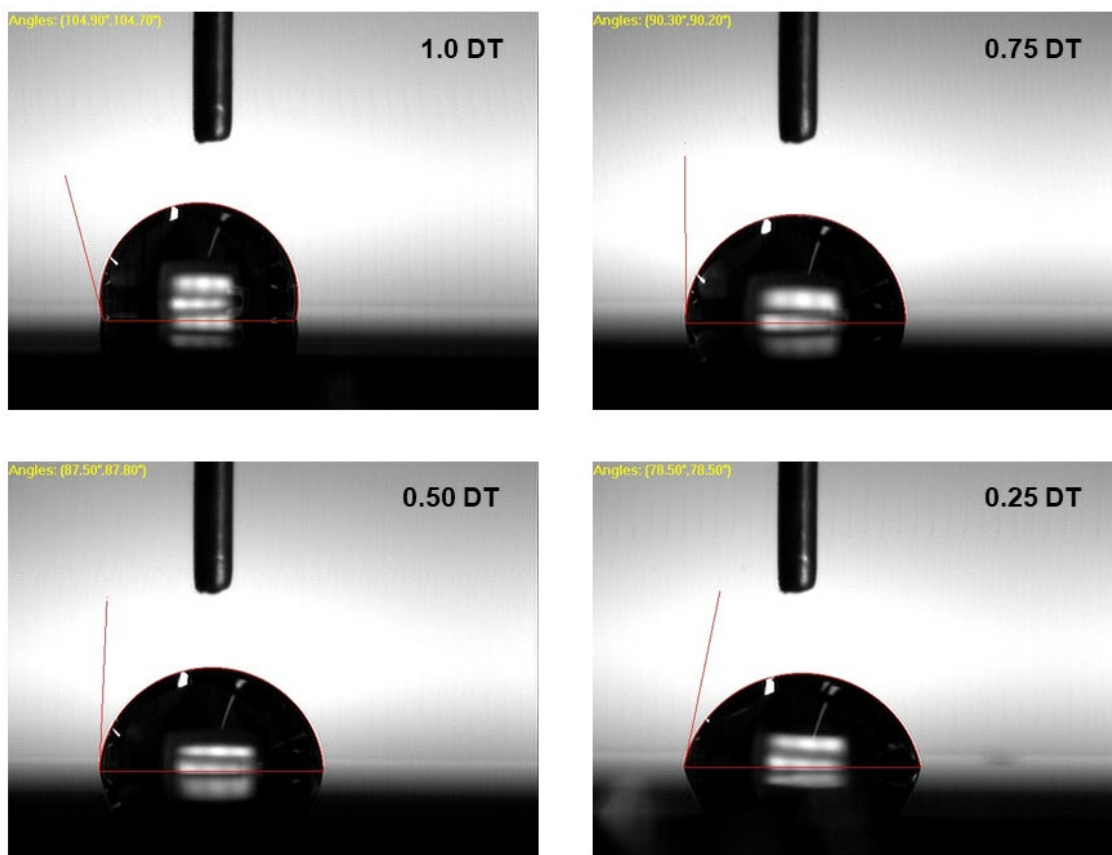
Figure 76. Representative images of 2 µl water droplet used to determine contact angles on mixed SAMs containing AZT and DT. The mole fraction of DT used in the deposition solution for each SAM is indicated in the top right corner of the image.
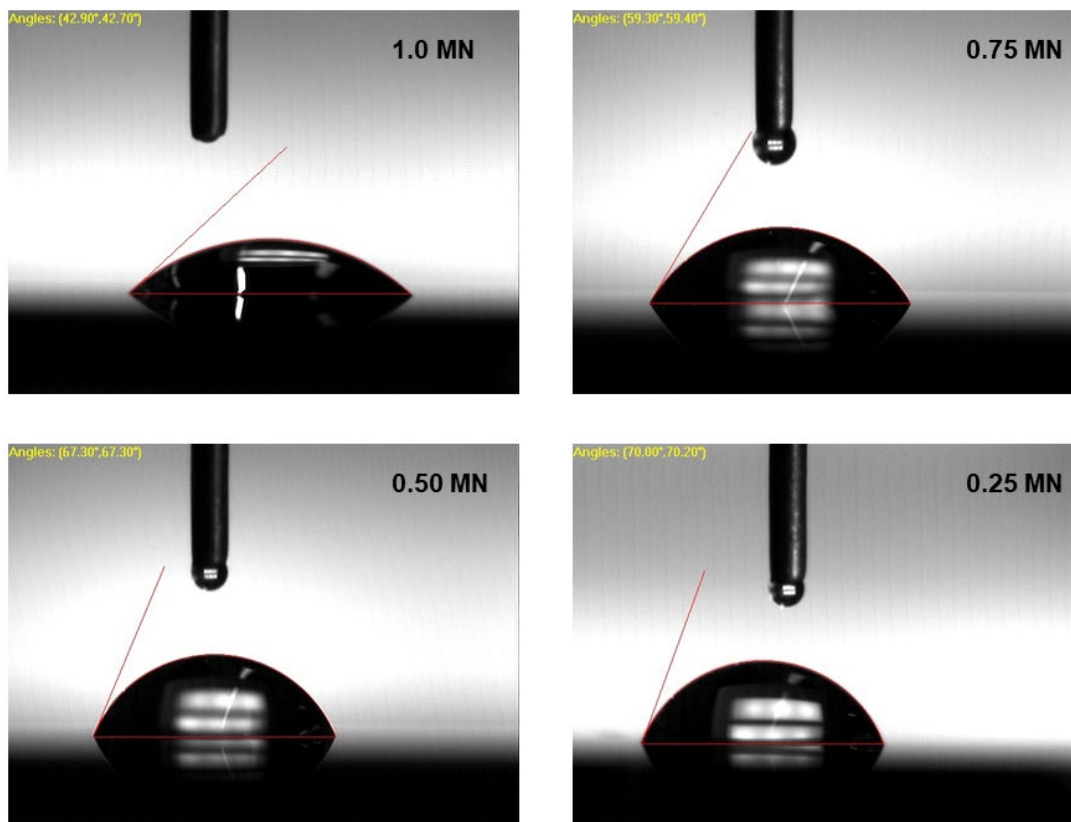
Figure 77. Representative images of 2 µl water droplet used to determine contact angles on mixed SAMs containing AZT and MN. The mole fraction of MN used in the deposition solution for each SAM is indicated in the top right corner of the image.
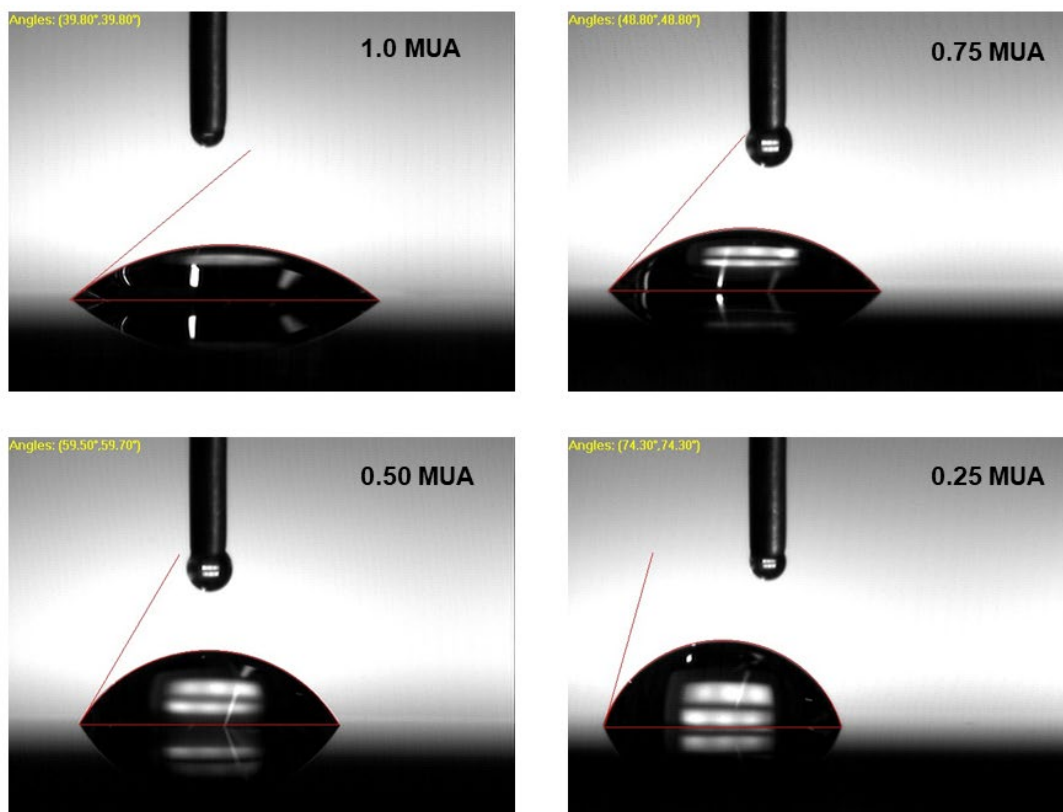
Figure 78. Representative images of 2 µl water droplet used to determine contact angles on mixed SAMs containing AZT and MUA. The mole fraction of MUA used in the deposition solution for each SAM is indicated in the top right corner of the image.
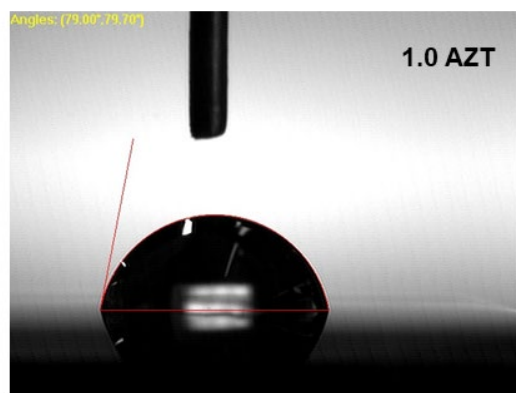
Figure 79. Representative image of 2 µl water droplet used to determine the contact angles on an AZT SAM. The mole fraction of AZT used in the deposition solution is indicated in the top right corner of the image.

HO〜〜〜〜〜〜〜N$_3$

^{1}H NMR, 300MHz

3.656
3.634
3.612
3.271
3.248
3.225

1.613
1.588
1.565
1.541
1.514
1.371
1.279

| 11 | 10 | 9 | 8 | 7 | 6 | 5 | 4 | 3 | 2 | 1 | ppm |

2.00 2.01   4.13 15.40
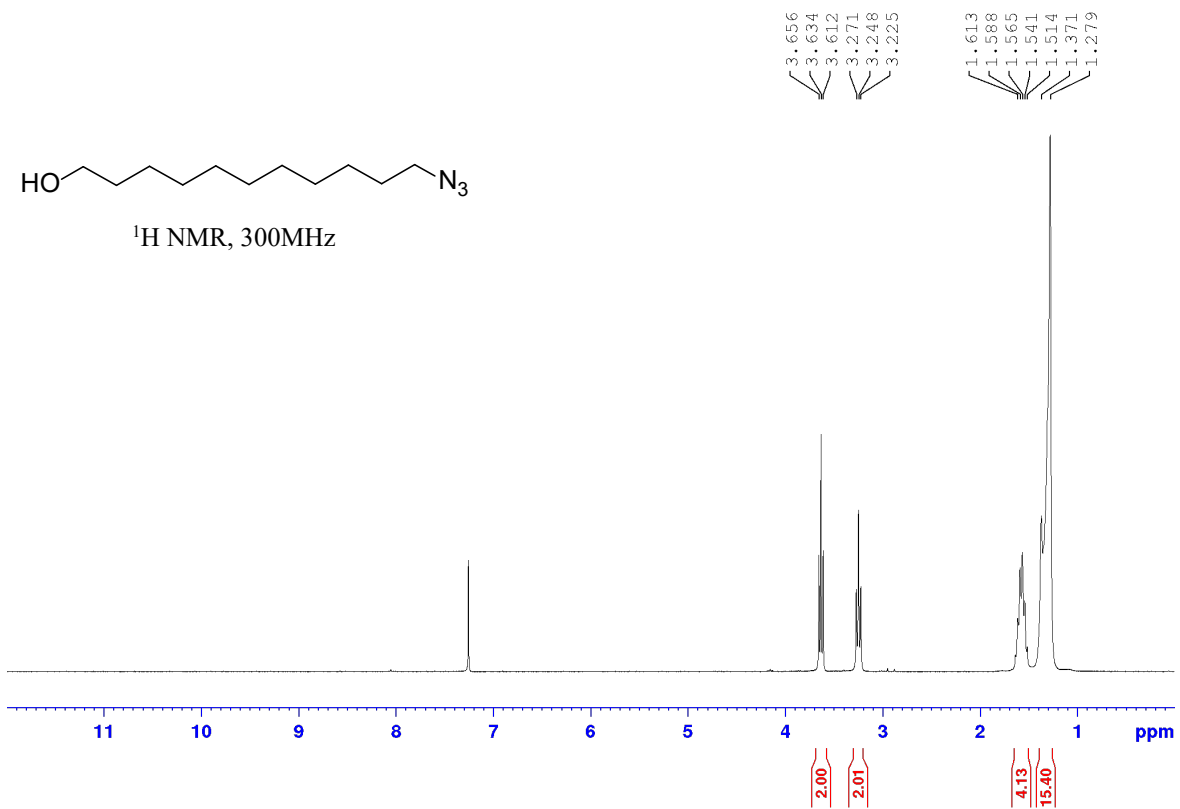
Figure 80. ^{1}H NMR spectrum of compound **9**.
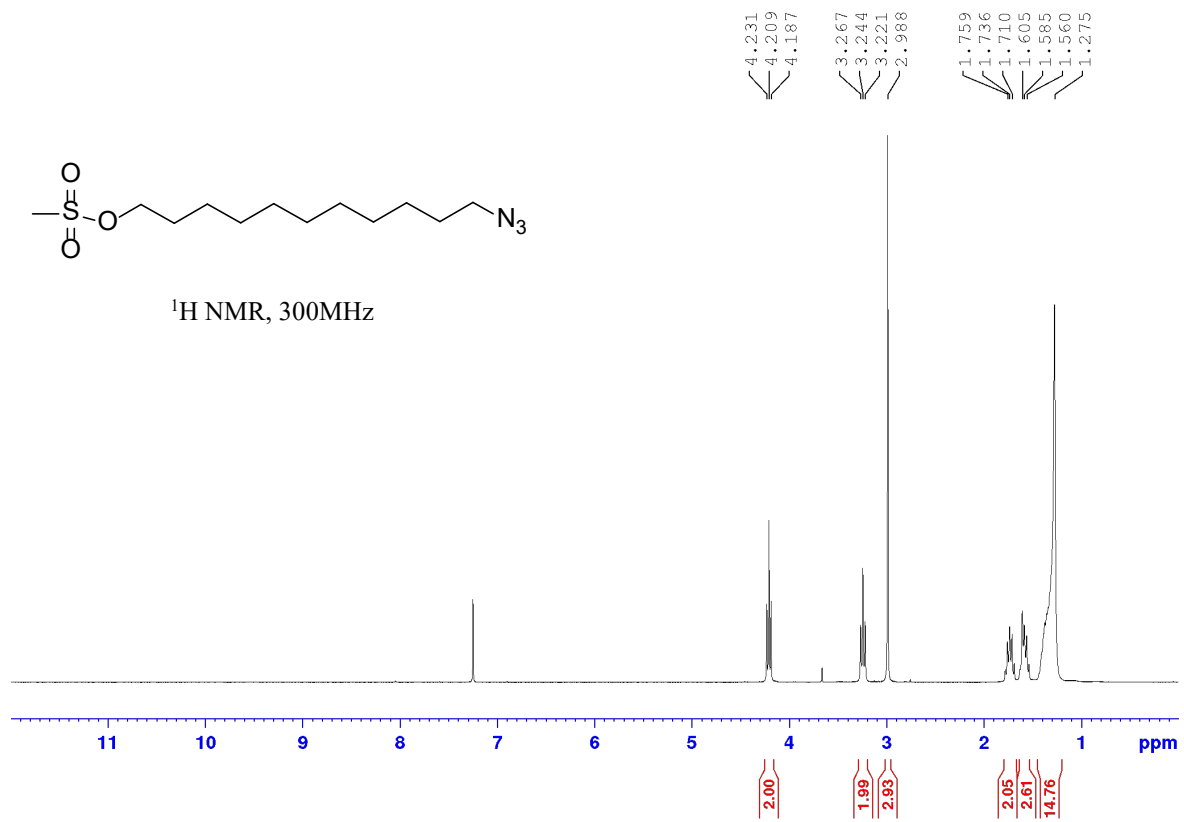
Figure 81. ^{1}H NMR spectrum of compound **10**.
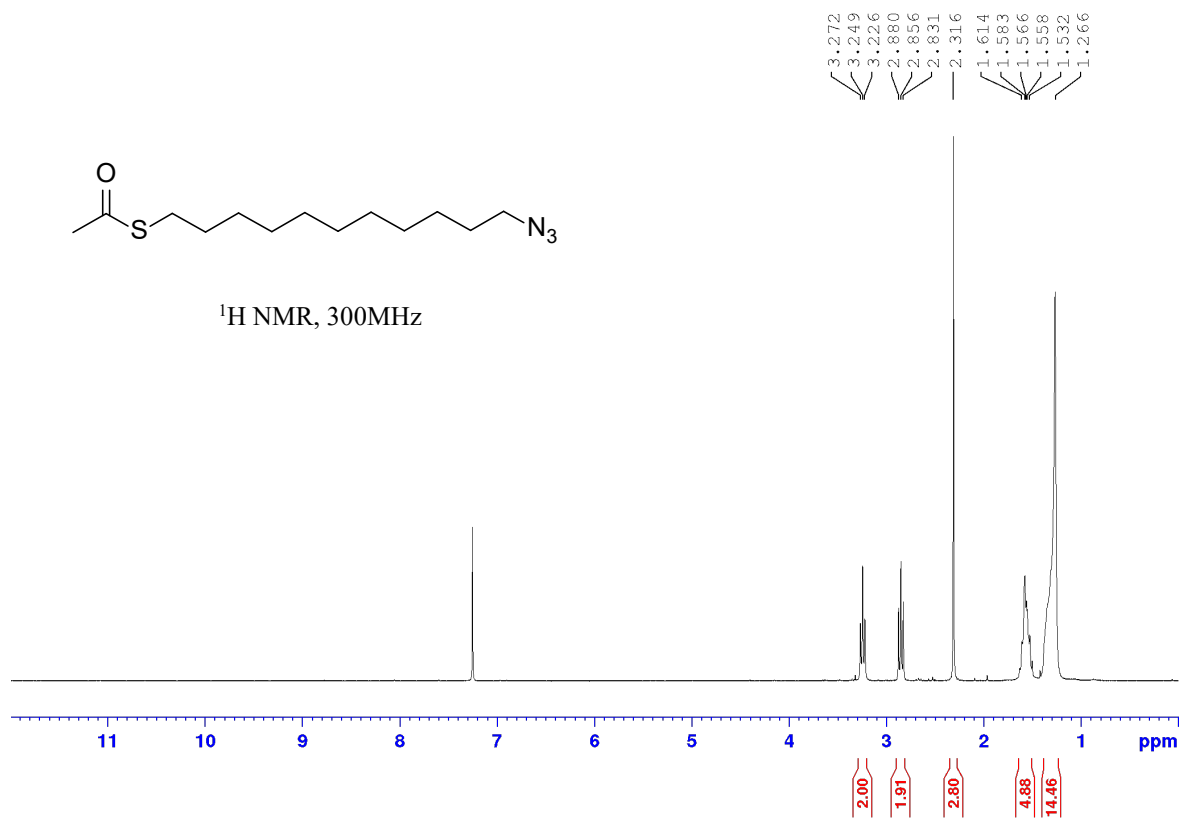
Figure 82. ^{1}H NMR spectrum of compound **11**.
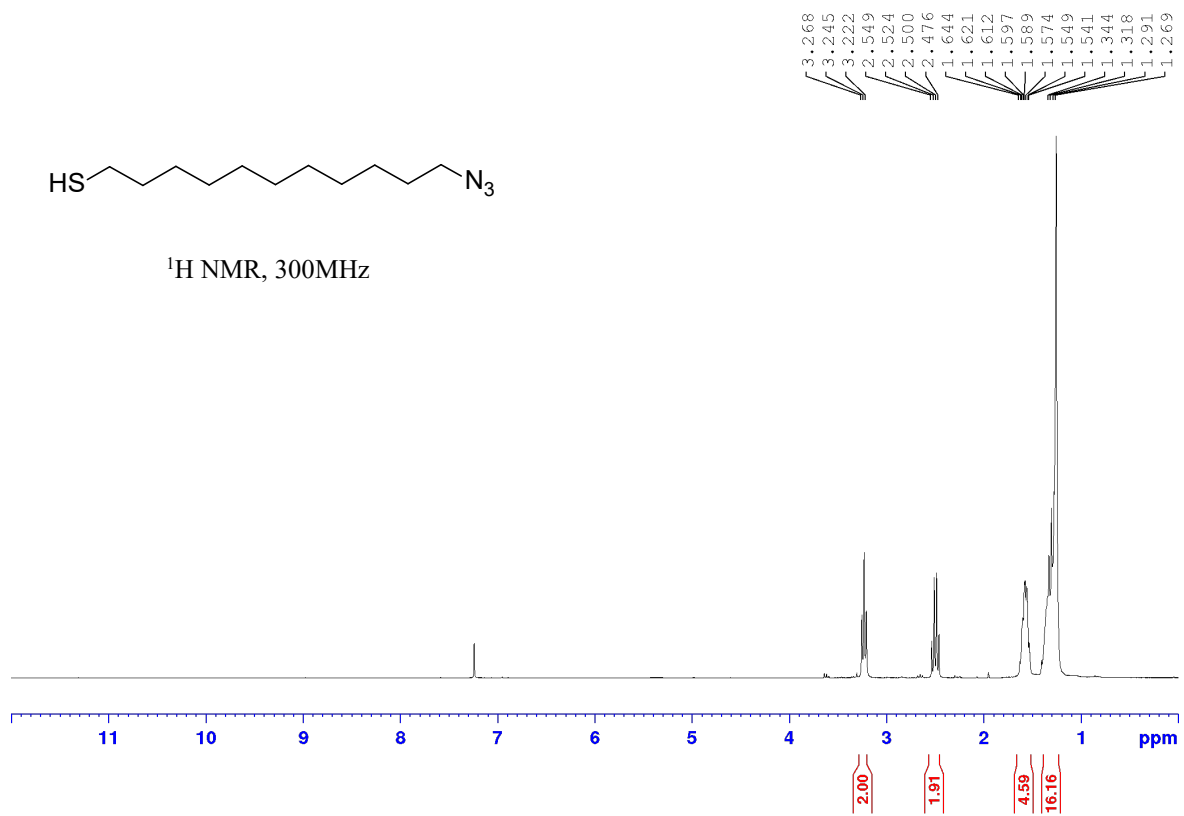
Figure 83. ^{1}H NMR spectrum of **AZT**.
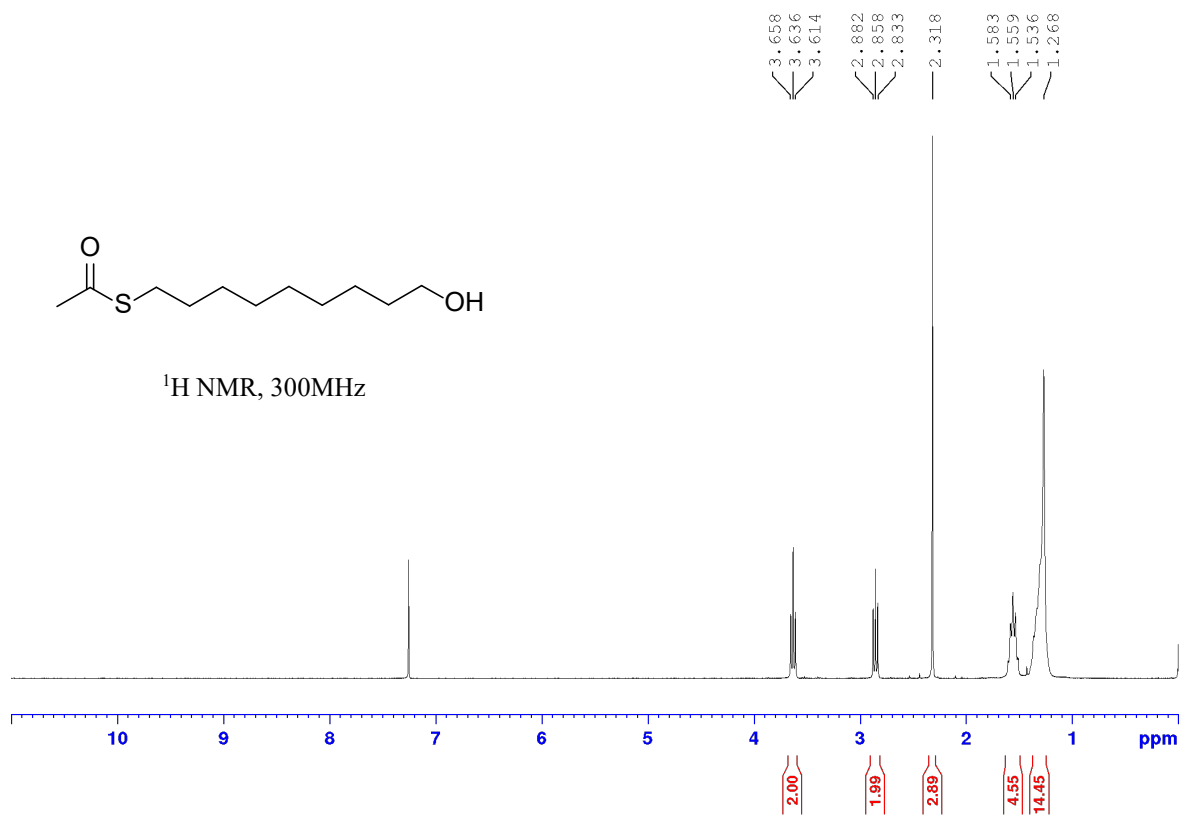
Figure 84. ^{1}H NMR spectrum of compound **12**.

HS~~~~~OH

^{1}H NMR, 300MHz
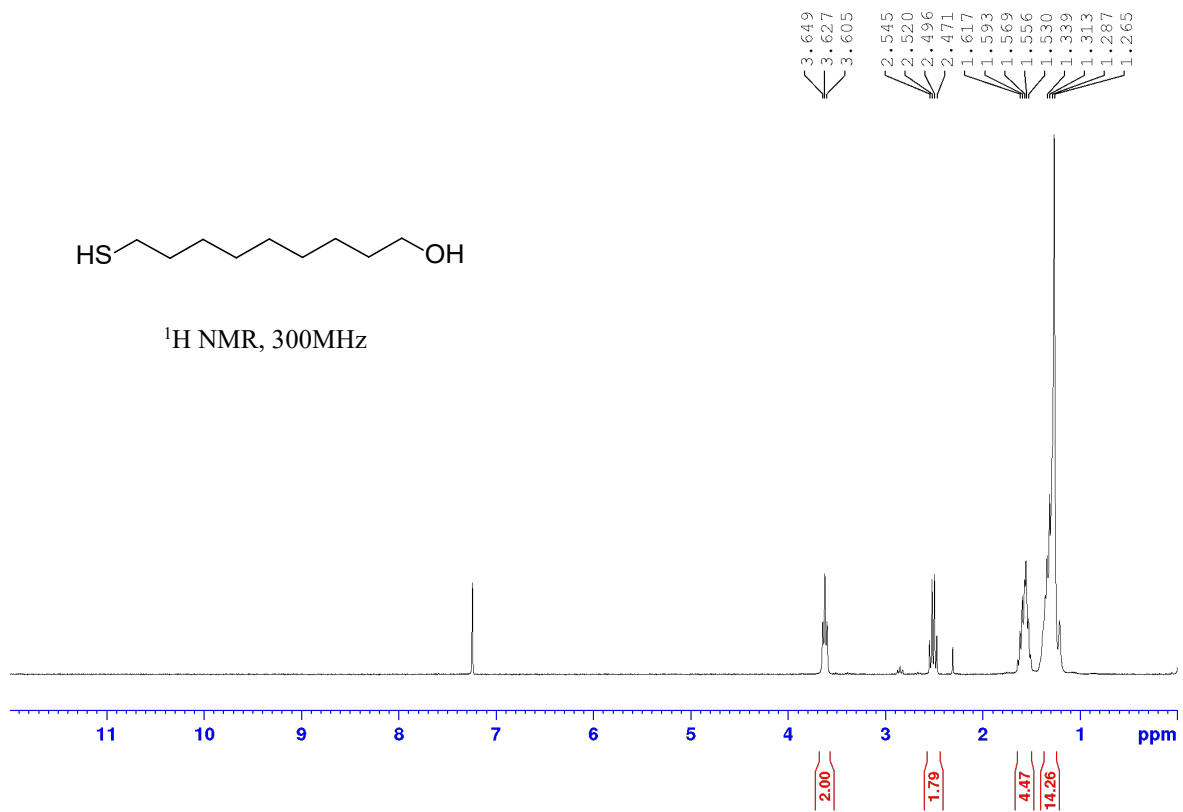
Figure 85. ^{1}H NMR spectrum of **MN**.
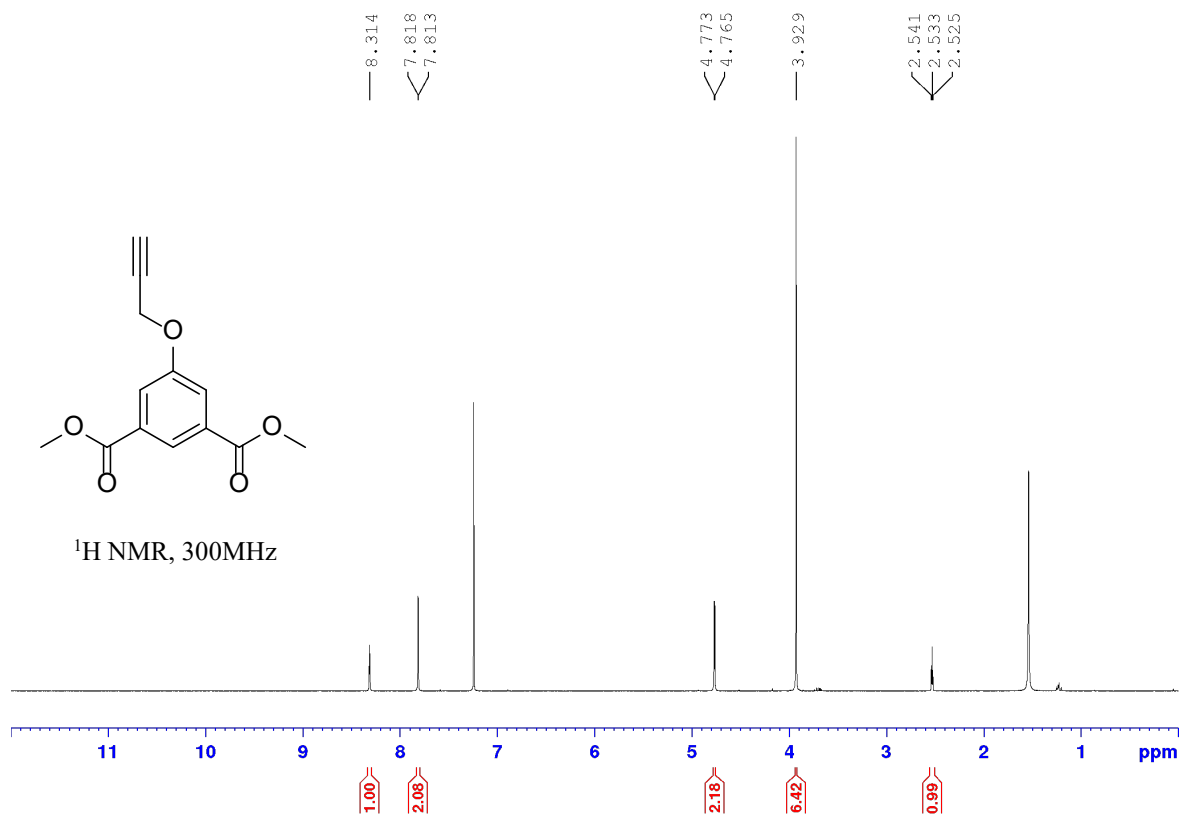
Figure 86. ^{1}H NMR spectrum of compound **13**.
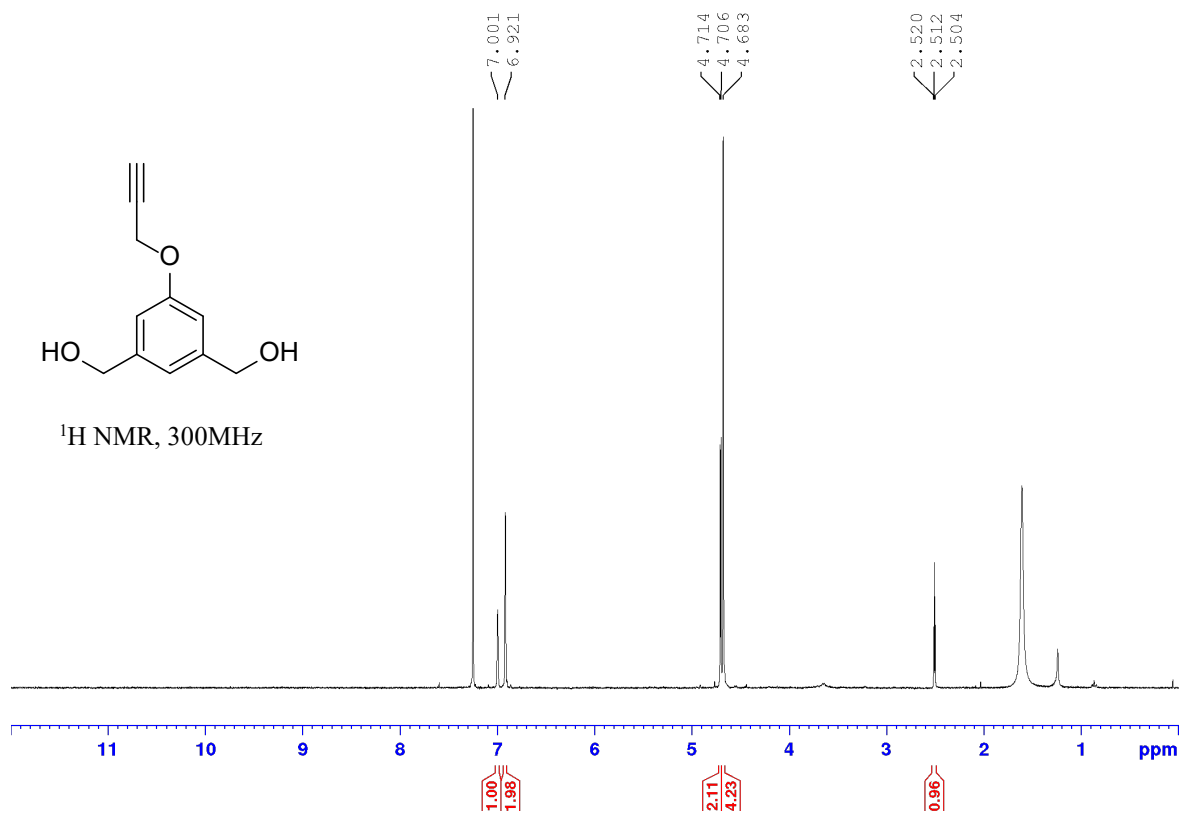
Figure 87. ^{1}H NMR spectrum of compound **14**.
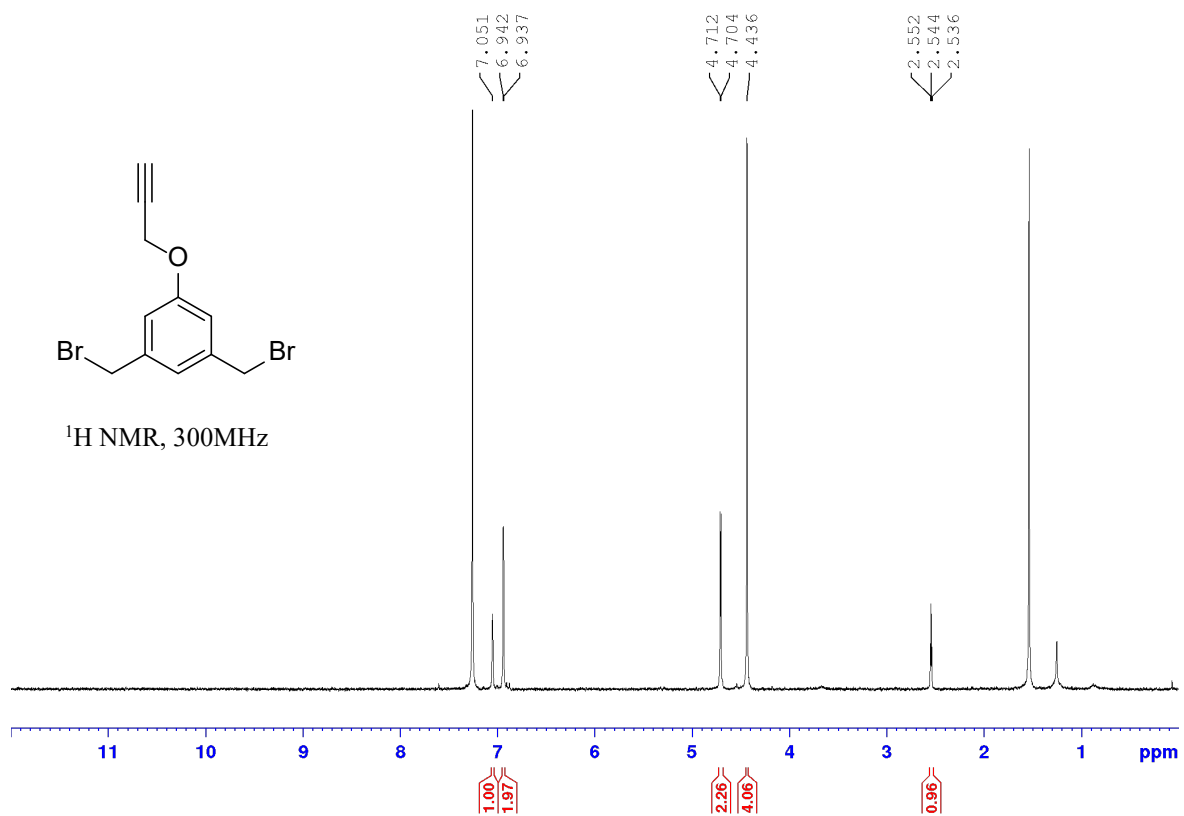
Figure 88. ^{1}H NMR spectrum of **DBMPB**.
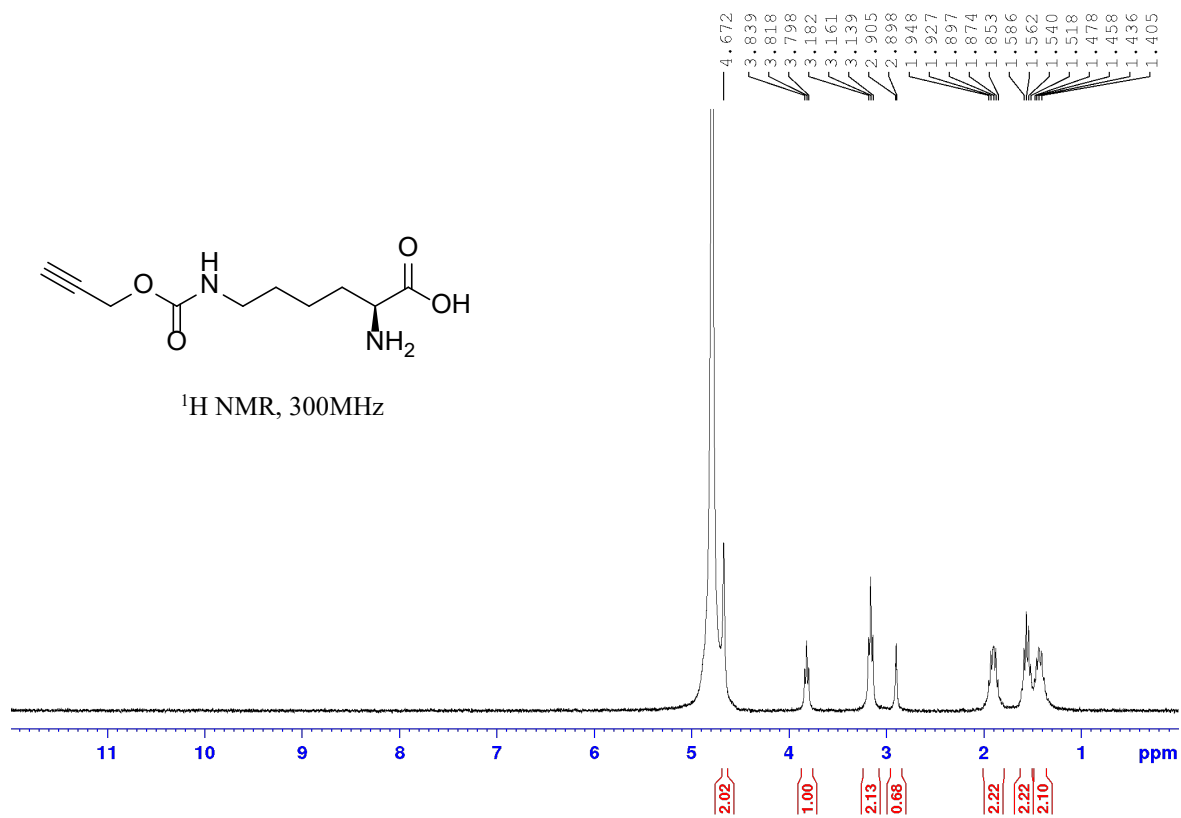
Figure 89. ^{1}H NMR spectrum of **PK**.

6.920
6.841
6.837

4.700
4.692

3.681
3.657
3.637
3.617

2.649
2.629
2.609
2.541
2.533
2.525

^{1}H NMR, 300MHz

1.00
1.96

2.08

4.06
4.34

4.20
0.99

11 10 9 8 7 6 5 4 3 2 1 ppm
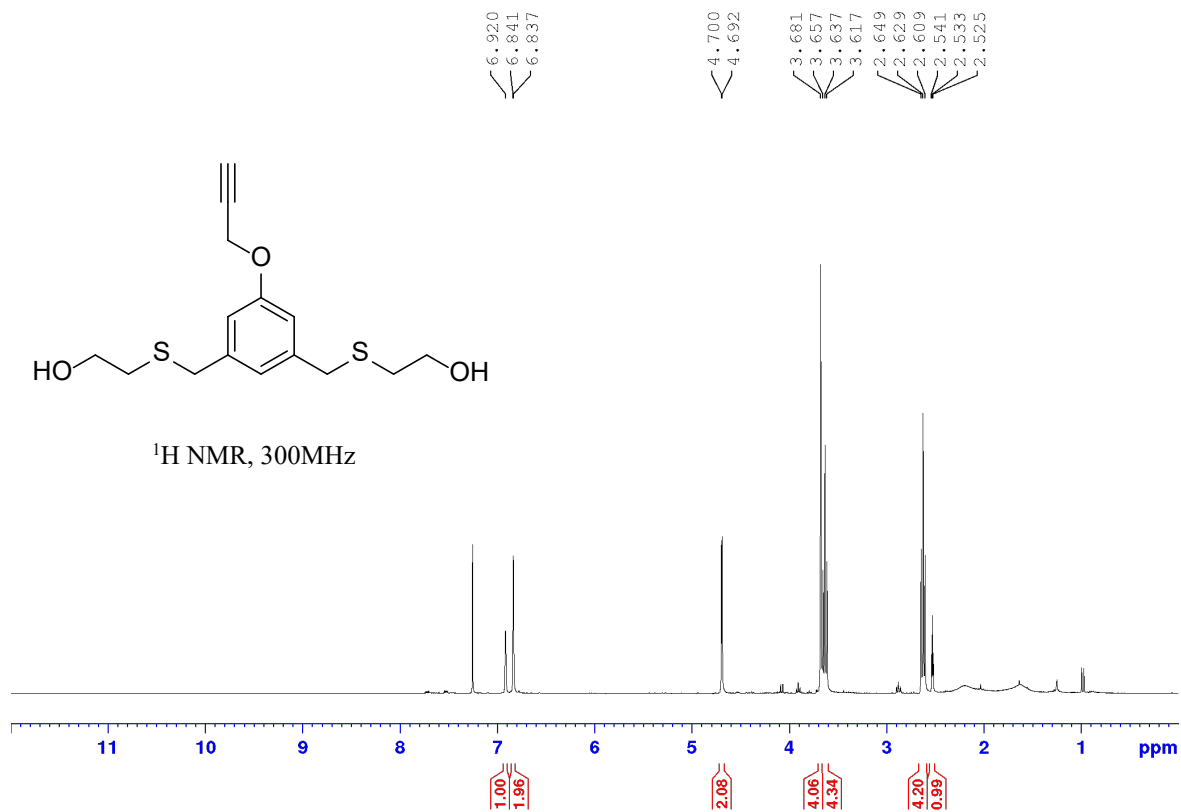
Figure 90. ^{1}H NMR spectrum of compound **15**.

^{13}C NMR, 400MHz
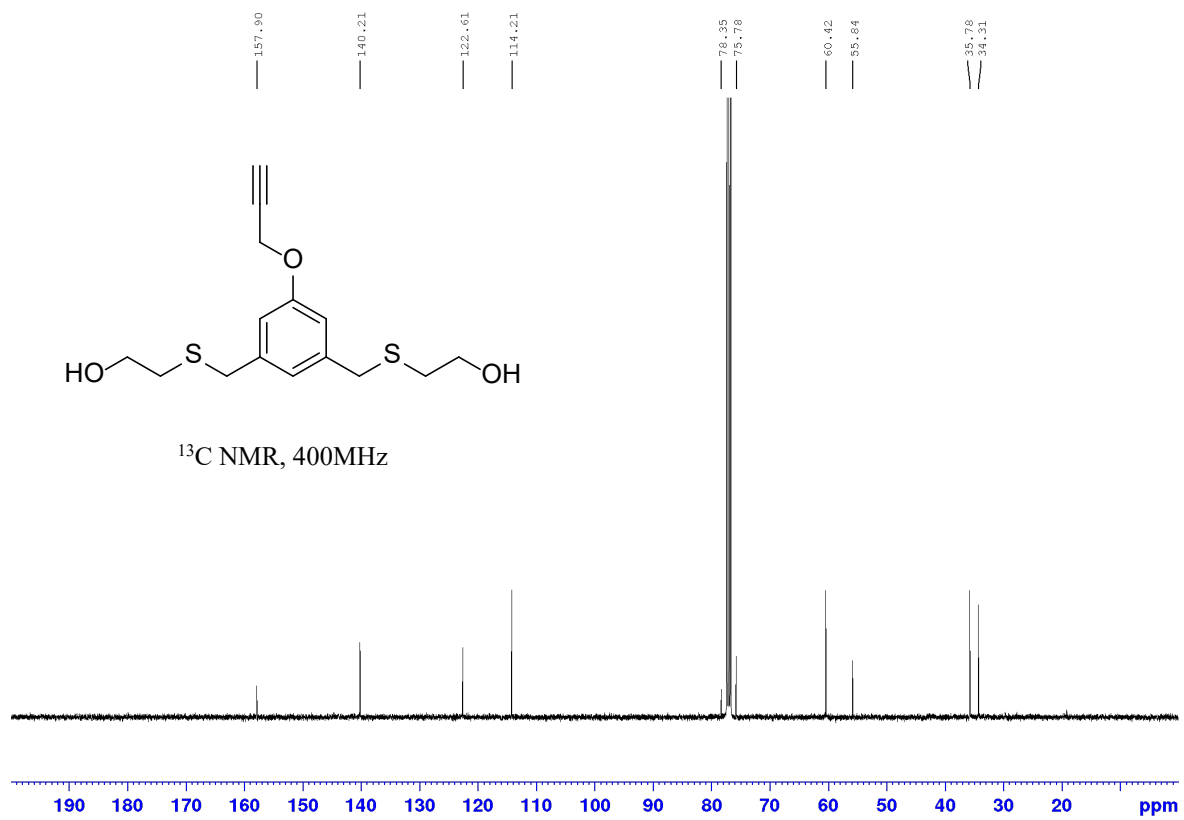
Figure 91. ^{13}C NMR spectrum of compound **15**.

Appendix C : Python Code for PM-IRRAS Baseline Correction

```python
# import needed Python modules
import os
import glob
import pandas as pd
import numpy as np
import matplotlib.pyplot as plt
import seaborn as sns
sns.set_style("whitegrid")
%matplotlib inline

# ignore "future" warnings (i.e., code that will need to be updated)
import warnings
warnings.simplefilter(action='ignore', category=FutureWarning)
warnings.simplefilter(action='ignore', category=UserWarning)


# Install a pip package in the current Jupyter kernel
try:
    import rampy
except:
    import sys
    !{sys.executable} -m pip install --user rampy
    # now import it
    import rampy


# set some features of interest for the fitting - less crucial for arPLS
roi = np.array([[960,1031],[1248,1256],[1285,1295],[1750,2800]])

# Let's import the raw data - every CSV file in this directory:
for filename in glob.iglob('*.CSV'):
    # track what we're processing
    print('processing: ' + filename)


df = pd.read_csv(filename, names=['Wavenumbers','Trans'])
wavenumbers = np.array(df.Wavenumbers)
# use arPLS baseline correction: asymmetrically reweighted penalized least squares fitting
# Analyst, 2015,140, 250-257
#  doi: 10.1039/C4AN01061B
# use arPLS baseline correction: asymmetrically reweighted penalized least squares fitting
# Analyst, 2015,140, 250-257
#  doi: 10.1039/C4AN01061B
#ycalc_arpls, base_arpls = rampy.baseline(df.Wavenumbers.values, df.Trans.values, roi,'poly', polynomial_order=3)
ycalc_arpls, base_arpls = rampy.baseline(df.Wavenumbers.values, df.Trans.values, roi,'arPLS', lam=10**6)


# now we save it to a new file under the 'corrected' subdirectory
#   remove 'csv' extension
new_name = filename[:-4]
if ' atm supp' in new_name:
    new_name = new_name[:-9]
new_name += ' corrected.csv'
```

Bibliography

1. Pepe-Mooney, B. J.; Fairman, R. *Curr. Opin. Struc. Biol.* **2009,** *19* (4), 483-494.

2. Heinzmann, C.; Weder, C.; de Espinosa, L. M. *Chem. Soc. Rev.* **2016,** *45* (2), 342-358.

3. Cui, H.; Webber, M. J.; Stupp, S. I. *Peptide Science* **2010,** *94* (1), 1-18.

4. Banwell, E. F.; Abelardo, E. S.; Adams, D. J.; Birchall, M. A.; Corrigan, A.; Donald, A. M.; Kirkland, M.; Serpell, L. C.; Butler, M. F.; Woolfson, D. N. *Nature Materials* **2009,** *8*, 596.

5. Behrendt, R.; White, P.; Offer, J. *J. Pept. Sci.* **2016,** *22* (1), 4-27.

6. Almhjell, P. J.; Boville, C. E.; Arnold, F. H. *Chem. Soc. Rev.* **2018,** *47* (24), 8980-8997.

7. Lang, K.; Chin, J. W. *ACS Chemical Biology* **2014,** *9* (1), 16-20.

8. Stella, L.; Bocchinfuso, G.; Gatto, E.; Mazzuca, C.; Venanzi, M.; Formaggio, F.; Toniolo, C.; Palleschi, A.; Pispisa, B. In *Reviews in Fluorescence 2008*, Geddes, C. D., Ed. Springer New York: New York, NY, 2010; pp 405-424.

9. Gatto, E.; Venanzi, M. *Polymer Journal* **2013,** *45*, 468.

10. Chen, Z.; Lv, Z.; Qing, G.; Sun, T. *J. Mater. Chem. B* **2017,** *5* (17), 3163-3171.

11. Lv, Z.; Zhou, Y.; Han, S.-T.; Roy, V. A. L. *Materials Today* **2018,** *21* (5), 537-552.

12. Shtreimer Kandiyote, N.; Mohanraj, G.; Mao, C.; Kasher, R.; Arnusch, C. J. *Langmuir* **2018,** *34* (37), 11147-11155.

13. Bodner, E. J.; Kandiyote, N. S.; Lutskiy, M.-Y.; Albada, H. B.; Metzler-Nolte, N.; Uhl, W.; Kasher, R.; Arnusch, C. J. *RSC Advances* **2016,** *6* (94), 91815-91823.

14. Costa, F.; Carvalho, I. F.; Montelaro, R. C.; Gomes, P.; Martins, M. C. L. *Acta Biomaterialia* **2011,** *7* (4), 1431-1440.

15. Mishra, B.; Lushnikova, T.; Golla, R. M.; Wang, X.; Wang, G. *Acta Biomaterialia* **2017,** *49*, 316-328.

16. Sakala, G. P.; Reches, M. *Adv. Mater. Inter.* **2018,** *5* (18), 1800073.

17. Nowinski, A. K.; Sun, F.; White, A. D.; Keefe, A. J.; Jiang, S. *J. Am. Chem. Soc.* **2012,** *134* (13), 6000-6005.

18. Lapenta, F.; Aupič, J.; Strmšek, Ž.; Jerala, R. *Chem. Soc. Rev.* **2018,** *47* (10), 3530-3542.

19. Tavenor, N. A.; Murnin, M. J.; Horne, W. S. *J. Am. Chem. Soc.* **2017,** *139* (6), 2212-2215.

20. Dong, H.; Paramonov, S. E.; Hartgerink, J. D. *J. Am. Chem. Soc.* **2008,** *130* (41), 13691-13695.

21. Pandya, M. J.; Spooner, G. M.; Sunde, M.; Thorpe, J. R.; Rodger, A.; Woolfson, D. N. *Biochemistry* **2000,** *39* (30), 8728-8734.

22. Egelman, E. H.; Xu, C.; DiMaio, F.; Magnotti, E.; Modlin, C.; Yu, X.; Wright, E.; Baker, D.; Conticello, V. P. *Structure* **2015,** *23* (2), 280-289.

23. Fletcher, J. M.; Harniman, R. L.; Barnes, F. R. H.; Boyle, A. L.; Collins, A.; Mantell, J.; Sharp, T. H.; Antognozzi, M.; Booth, P. J.; Linden, N.; Miles, M. J.; Sessions, R. B.; Verkade, P.; Woolfson, D. N. *Science* **2013,** *340* (6132), 595.

24. Wu, Y.; Collier, J. H. *Wiley Interdiscip Rev Nanomed Nanobiotechnol* **2017,** *9* (2), 10.1002/wnan.1424.

25. Gellman, S. H. *Acc. Chem. Res.* **1998,** *31* (4), 173-180.

26. Hein, R.; Borissov, A.; Smith, M. D.; Beer, P. D.; Davis, J. J. *Chem. Commun.* **2019,** *55* (33), 4849-4852.

27. Gobbo, C.; Li, M.; Mali, K. S.; van Esch, J. H.; De Feyter, S. *ACS Nano* **2012,** *6* (12), 10684-10698.

28. Matmor, M.; Lengyel, G. A.; Horne, W. S.; Ashkenasy, N. *Phys. Chem. Chem. Phys.* **2017,** *19* (8), 5709-5714.

29. Khan, A.; Kaiser, C.; Hecht, S. *Angew. Chem. Inter. Ed.* **2006,** *45* (12), 1878-1881.

30. Lau, K. H. A.; Sileika, T. S.; Park, S. H.; Sousa, A. M. L.; Burch, P.; Szleifer, I.; Messersmith, P. B. *Adv. Mater. Inter.* **2015,** *2* (1), 1400225.

31. Sun, J.; Zuckermann, R. N. *ACS Nano* **2013,** *7* (6), 4715-4732.

32. Zuckermann, R. N.; Kerr, J. M.; Kent, S. B.; Moos, W. H. *J. Am. Chem. Soc.* **1992,** *114* (26), 10646-10647.

33. Gorske, B. C.; Jewell, S. A.; Guerard, E. J.; Blackwell, H. E. *Organic Letters* **2005,** *7* (8), 1521-1524.

34. Kirshenbaum, K.; Barron, A. E.; Goldsmith, R. A.; Armand, P.; Bradley, E. K.; Kiet, T. V. T.; Dill, K. A.; Cohen, F. E.; Zuckermann, R. N. *Proc. Natl. Acad. Sci. of the United States of America* **1998,** *95* (8), 4303-4308.

35. Nam, K. T.; Shelby, S. A.; Choi, P. H.; Marciel, A. B.; Chen, R.; Tan, L.; Chu, T. K.; Mesch, R. A.; Lee, B.-C.; Connolly, M. D.; Kisielowski, C.; Zuckermann, R. N. *Nature Materials* **2010,** *9*, 454.

36. Murnen, H. K.; Rosales, A. M.; Jaworski, J. N.; Segalman, R. A.; Zuckermann, R. N. *J. Am. Chem. Soc.* **2010,** *132* (45), 16112-16119.

37. Chen, C.-L.; Qi, J.; Zuckermann, R. N.; DeYoreo, J. J. *J. Am. Chem. Soc.* **2011,** *133* (14), 5214-5217.

38. Kang, B.; Chung, S.; Ahn, Y. D.; Lee, J.; Seo, J. *Organic Letters* **2013,** *15* (7), 1670-1673.

39. Goodman, M.; Bhumralkar, M.; Jefferson, E. A.; Kwak, J.; Locardi, E. *Peptide Science* **1998,** *47* (2), 127-142.

40. Sun, J.; Stone, G. M.; Balsara, N. P.; Zuckermann, R. N. *Macromolecules* **2012,** *45* (12), 5151-5156.

41. Izzo, I.; Ianniello, G.; De Cola, C.; Nardone, B.; Erra, L.; Vaughan, G.; Tedesco, C.; De Riccardis, F. *Organic Letters* **2013,** *15* (3), 598-601.

42. Love, J. C.; Estroff, L. A.; Kriebel, J. K.; Nuzzo, R. G.; Whitesides, G. M. *Chemical Reviews* **2005,** *105* (4), 1103-1170.

43. Christman, K. L.; Broyer, R. M.; Tolstyka, Z. P.; Maynard, H. D. *J. Mater. Chem.* **2007,** *17* (19), 2021-2027.

44. Jonkheijm, P.; Weinrich, D.; Köhn, M.; Engelkamp, H.; Christianen, P. C. M.; Kuhlmann, J.; Maan, J. C.; Nüsse, D.; Schroeder, H.; Wacker, R.; Breinbauer, R.; Niemeyer, C. M.; Waldmann, H. *Angew. Chem. Inter. Ed.* **2008,** *47* (23), 4421-4424.

45. Shamsi, F.; Coster, H.; Jolliffe, K. A. *Surface Science* **2011,** *605* (19), 1763-1770.

46. Sakamoto, H.; Ikeno, S.; Kato, T.; Nishino, N.; Haruyama, T. *Analytica Chimica Acta* **2007,** *604* (1), 76-80.

47. Rogero, C.; Chaffey, B. T.; Mateo-Martí, E.; Sobrado, J. M.; Horrocks, B. R.; Houlton, A.; Lakey, J. H.; Briones, C.; Martín-Gago, J. A. *J. Phys. Chem. C* **2008,** *112* (25), 9308-9314.

48. Laibinis, P. E.; Whitesides, G. M.; Allara, D. L.; Tao, Y. T.; Parikh, A. N.; Nuzzo, R. G. *J. Am. Chem. Soc.* **1991,** *113* (19), 7152-7167.

49. Chidsey, C. E. D.; Bertozzi, C. R.; Putvinski, T. M.; Mujsce, A. M. *J. Am. Chem. Soc.* **1990,** *112* (11), 4301-4306.

50. Ulman, A.; Eilers, J. E.; Tillman, N. *Langmuir* **1989,** *5* (5), 1147-1152.

51. Ulman, A.; Evans, S. D.; Shnidman, Y.; Sharma, R.; Eilers, J. E.; Chang, J. C. *J. Am. Chem. Soc.* **1991,** *113* (5), 1499-1506.

52.   Venanzi, M.; Pace, G.; Palleschi, A.; Stella, L.; Castrucci, P.; Scarselli, M.; De Crescenzi, M.; Formaggio, F.; Toniolo, C.; Marletta, G. *Surface Science* **2006,** *600* (2), 409-416.

53.   Mendez-Ardoy, A.; Markandeya, N.; Li, X.; Tsai, Y.-T.; Pecastaings, G.; Buffeteau, T.; Maurizot, V.; Muccioli, L.; Castet, F.; Huc, I.; Bassani, D. M. *Chemical Science* **2017**.

54.   Pomerantz, W. C.; Cadwell, K. D.; Hsu, Y.-J.; Gellman, S. H.; Abbott, N. L. *Chem. Mater.* **2007,** *19* (18), 4436-4441.

55.   Sek, S.; Swiatek, K.; Misicka, A. *J. Phys. Chem. B* **2005,** *109* (49), 23121-23124.

56.   Morita, T.; Kimura, S. *J. Am. Chem. Soc.* **2003,** *125* (29), 8732-8733.

57.   Shlizerman, C.; Atanassov, A.; Berkovich, I.; Ashkenasy, G.; Ashkenasy, N. *J. Am. Chem. Soc.* **2010,** *132* (14), 5070-5076.

58.   Naaman, R.; Fontanesi, C.; Waldeck, D. H. *Curr. Opin. Electrochem.* **2019,** *14*, 138-142.

59.   Steven, R. A.; Henry, A. S. *Smart Materials and Structures* **2007,** *16* (3), R1.

60.   Ando, Y.; Fukada, E. *J. Polym. Sci.: Polym. Phys. Ed.* **1976,** *14* (1), 63-79.

61.   Eiichi, F.; Iwao, Y. *Jap. J. Appl. Phys.* **1964,** *3* (2), 117.

62.   Fukada, E. *IEEE Transactions on Ultrasonics, Ferroelectrics, and Frequency Control* **2000,** *47* (6), 1277-1290.

63.   Quan, X.; Marvin, C. W.; Seebald, L.; Hutchison, G. R. *J. Phys. Chem. C* **2013,** *117* (33), 16783-16790.

64.   Lefki, K.; Dormans, G. J. M. *J. Appl. Phys.* **1994,** *76* (3), 1764-1767.

65.   Crisler, D. F.; Cupal, J. J.; Moore, A. R. *Proc. IEEE* **1968,** *56* (2), 225-226.

66.   Bottom, V. E. *J. Appl. Phys.* **1970,** *41* (10), 3941-3944.

67.   Kholkin, A.; Amdursky, N.; Bdikin, I.; Gazit, E.; Rosenman, G. *ACS Nano* **2010,** *4* (2), 610-614.

68.   Yuan, M. Z.; Zhang, J. R.; Yang, L. Z.; Fang, E. Q.; Li, Z. J.; Ren, H. *Materials Research Innovations* **2015,** *19* (sup1), S1-134-S1-138.

69.   Panda, P. K. *J. Mater. Sci.* **2009,** *44* (19), 5049-5062.

70.   Guerin, S.; Syed, T. A. M.; Thompson, D. *Nanoscale* **2018,** *10* (20), 9653-9663.

71.   Guerin, S.; O'Donnell, J.; Haq, E. U.; McKeown, C.; Silien, C.; Rhen, F. M. F.; Soulimane, T.; Tofail, S. A. M.; Thompson, D. *Phys. Rev. Lett.* **2019,** *122* (4), 047701.

72. Lee, B. Y.; Zhang, J.; Zueger, C.; Chung, W.-J.; Yoo, S. Y.; Wang, E.; Meyer, J.; Ramesh, R.; Lee, S.-W. *Nat Nano* **2012,** *7* (6), 351-356.

73. Nguyen, V.; Zhu, R.; Jenkins, K.; Yang, R. *Nature Commun.* **2016,** *7*, 13566.

74. Sessler, G. M. *J. Acoust. Soc. Am.* **1981,** *70* (6), 1596-1608.

75. Kalinin, S. V.; Rodriguez, B. J.; Kholkin, A. L. In *Encyclopedia of Nanotechnology*, Bhushan, B., Ed. Springer Netherlands: Dordrecht, 2012; pp 2117-2125.

76. Werling, K. A.; Hutchison, G. R.; Lambrecht, D. S. *J. Phys. Chem. Lett.* **2013,** *4* (9), 1365-1370.

77. Moody, M. J.; Marvin, C. W.; Hutchison, G. R. *J. Mater. Chem. C* **2016,** *4* (20), 4387-4392.

78. Gruverman, A.; Rodriguez, B. J.; Kalinin, S. V. In *Scanning probe microscopy*, Springer: 2007; pp 615-633.

79. Nguyen, V.; Jenkins, K.; Yang, R. *Nano Energy* **2015,** *17*, 323-329.

80. Farrar, D.; West, J. E.; Busch-Vishniac, I. J.; Yu, S. M. *Scripta Materialia* **2008,** *59* (10), 1051-1054.

81. Dagdeviren, C.; Yang, B. D.; Su, Y.; Tran, P. L.; Joe, P.; Anderson, E.; Xia, J.; Doraiswamy, V.; Dehdashti, B.; Feng, X.; Lu, B.; Poston, R.; Khalpey, Z.; Ghaffari, R.; Huang, Y.; Slepian, M. J.; Rogers, J. A. *Proc. Natl. Acad. Sci.* **2014,** *111* (5), 1927.

82. Quan, X. M., J. D.; Hutchison, G. R. *arXiv: 1706.08993, https://arxiv.org/abs/1706.08993* **2017,** *Accessed August 12 2019*.

83. Morsbach, S.; Gonella, G.; Mailänder, V.; Wegner, S.; Wu, S.; Weidner, T.; Berger, R.; Koynov, K.; Vollmer, D.; Encinas, N.; Kuan, S. L.; Bereau, T.; Kremer, K.; Weil, T.; Bonn, M.; Butt, H.-J.; Landfester, K. *Angew. Chem. Inter. Ed.* **2018,** *57* (39), 12626-12648.

84. White, S. J.; Johnson, S. D.; Sellick, M. A.; Bronowska, A.; Stockley, P. G.; Wälti, C. *Angew. Chem. Inter. Ed.* **2015,** *54* (3), 974-978.

85. Norde, W.; Horbett, T. A.; Brash, J. L. In *Proteins at Interfaces III State of the Art*, American Chemical Society: 2012; Vol. 1120, pp 1-34.

86. Sivaraman, B.; Fears, K. P.; Latour, R. A. *Langmuir* **2009,** *25* (5), 3050-3056.

87. Lassen, B.; Malmsten, M. *Journal of Colloid and Interface Science* **1997,** *186* (1), 9-16.

88. Bilek, M. M., McKenzie, D.R.. *Biophys. Rev.* **2010,** *2* (2), 55-65.

89. Zelzer, M., Majani, R., Bradley, J. W. Felicity, R.A.J. Martyn, R., Davies, C., Alexander, M., R. *Biomaterials* **2008,** *29* (2), 172-184.

90. Ferrari, M. C., F.; Morán, M.C. *Colloids Interfaces* **2019,** *3* (2), 48-64.

91. Kurnik, M.; Ortega, G.; Dauphin-Ducharme, P.; Li, H.; Caceres, A.; Plaxco, K. W. *Proc. Natl. Acad. Sci.* **2018,** *115* (33), 8352-8357.

92. Ortega, G.; Kurnik, M.; Dauphin-Ducharme, P.; Li, H.; Arroyo-Currás, N.; Caceres, A.; Plaxco, K. W. *Angew. Chem. Inter. Ed.* **2019,** *58* (6), 1714-1718.

93. Haeussling, L.; Ringsdorf, H.; Schmitt, F. J.; Knoll, W. *Langmuir* **1991,** *7* (9), 1837-1840.

94. Baker, B. R.; Lai, R. Y.; Wood, M. S.; Doctor, E. H.; Heeger, A. J.; Plaxco, K. W. *J. Am. Chem. Soc.* **2006,** *128* (10), 3138-3139.

95. Xiao, Y.; Piorek, B. D.; Plaxco, K. W.; Heeger, A. J. *J. Am. Chem. Soc.* **2005,** *127* (51), 17990-17991.

96. White, R. J.; Phares, N.; Lubin, A. A.; Xiao, Y.; Plaxco, K. W. *Langmuir* **2008,** *24* (18), 10513-10518.

97. Wei, J.; Liu, H.; Dick, A. R.; Yamamoto, H.; He, Y.; Waldeck, D. H. *J. Am. Chem. Soc.* **2002,** *124* (32), 9591-9599.

98. Beissenhirtz, M. K.; Scheller, F. W.; Lisdat, F.. *Analytical Chemistry* **2004,** *76* (16), 4665-4671.

99. Guo, X. *J. Biophotonics* **2012,** *5* (7), 483-501.

100. Cole, M. A., Voelcker, N. H., Thissen, H., Griesser, H. J. *Biomaterials* **2009,** *30* (9), 1827-1850.

101. Banerjee, R.; Chattopadhyay, S.; Basu, G. *Proteins: Struct., Funct., Bioinf.* **2009,** *76* (1), 184-200.

102. Bautista, A. D.; Craig, C. J.; Harker, E. A.; Schepartz, A. *Curr. Opin. Chem. Biol.* **2007,** *11* (6), 685-692.

103. Goodman, C. M.; Choi, S.; Shandler, S.; DeGrado, W. F. *Nat. Chem. Biol.* **2007,** *3* (5), 252-262.

104. Guichard, G.; Huc, I. *Chem. Commun.* **2011,** *47* (21), 5933-5941.

105. Kirshenbaum, K.; Barron, A. E.; Goldsmith, R. A.; Armand, P.; Bradley, E. K.; Truong, K. T. V.; Dill, K. A.; Cohen, F. E.; Zuckermann, R. N. *Proc. Natl. Acad. Sci. USA* **1998,** *95* (8), 4303-4308.

106. Wu, C. W.; Sanborn, T. J.; Zuckermann, R. N.; Barron, A. E. *J. Am. Chem. Soc.* **2001,** *123* (13), 2958-2963.

107. Burkoth, T. S.; Beausoleil, E.; Kaur, S.; Tang, D.; Cohen, F. E.; Zuckermann, R. N.. *Chemistry & Biology* **2002,** *9* (5), 647-654.

108. Wu, C. W.; Kirshenbaum, K.; Sanborn, T. J.; Patch, J. A.; Huang, K.; Dill, K. A.; Zuckermann, R. N.; Barron, A. E. *J. Am. Chem. Soc.* **2003,** *125* (44), 13525-13530.

109. Wu, C. W.; Sanborn, T. J.; Huang, K.; Zuckermann, R. N.; Barron, A. E. *J. Am. Chem. Soc.* **2001,** *123* (28), 6778-6784.

110. Shin, H.-M.; Kang, C.-M.; Yoon, M.-H.; Seo, J. *Chem. Commun.* **2014,** *50* (34), 4465-4468.

111. Zhang, M.-H.; Thong, H. C.; Lu, Y. X.; Sun,W.; Li, J.-F.; Wang, K. *J. Korean Ceramic Soc.* **2017,** *4* (54), 261-271.

112. Rodriguez, B. J.; Callahan, C.; Kalinin, S. V.; Proksch, R. *Nanotechnology* **2007,** *18* (47), 475504.

113. Marino, A. A.; Becker, R. O.; Soderholm, S. C. *Calc. Tis. Res.* **1971,** *8* (1), 177-180.

114. Fukada, E. *J. Phys. Soc. Jpn.* **1955,** *10* (2), 149-154.

115. Bowen, C. R.; Kim, H. A.; Weaver, P. M.; Dunn, S. *Energy Environ. Sci.* **2014,** *7* (1), 25-44.

116. Lu, H.; Hood, M. A.; Mauri, S.; Baio, J. E.; Bonn, M.; Munoz-Espi, R.; Weidner, T. *Chem Commun (Camb)* **2015,** *51* (88), 15902-5.

117. Kong, J.; Yu, S. *Acta Biochimica et Biophysica Sinica* **2007,** *39* (8), 549-559.

118. Jackson, M.; M., Henry. *Crit. Rev. Biochem. Molec. Biol.* **1995,** *30* (2), 95-120.

119. Martinez, G.; Millhauser, G. *J. Struc. Biol.* **1995,** *114* (1), 23-27.

120. Yang, H.; Yang, S.; Kong, J.; Dong, A.; Yu, S. *Nat. Protocols* **2015,** *10* (3), 382-396.

121. Andrushchenko, V. V.; Vogel, H. J.; Prenner, E. J. *J. Pept. Sci.* **2007,** *13* (1), 37-43.

122. Boncheva, M.; Vogel, H. *Biophysical Journal* **1997,** *73* (2), 1056-1072.

123. Wen, X.; Linton, R. W.; Formaggio, F.; Toniolo, C.; Samulski, E. T. *J. Phys. Chem. A* **2004,** *108* (45), 9673-9681.

124. Jiang, H.; Léger, J.-M.; Dolain, C.; Guionneau, P.; Huc, I. *Tetrahedron* **2003,** *59* (42), 8365-8374.

125. Zhang, D.-W.; Zhao, X.; Hou, J.-L.; Li, Z.-T. *Chemical Reviews* **2012,** *112* (10), 5271-5316.

126. Baptiste, B.; Douat-Casassus, C.; Laxmi-Reddy, K.; Godde, F.; Huc, I. *J. Org. Chem.* **2010,** *75* (21), 7175-85.

127. Dawson, S. J.; Hu, X.; Claerhout, S.; Huc, I. *Methods in Enzymology* **2016,** *580*, 279-301.

128. Dolain, C., Grélard, A., Laguerre, M., Jiang, H., Maurizot, V. and Huc, I., Solution Structure of Quinoline- and Pyridine-Derived Oligoamide Foldamers. *Chem. Eur. J.* **2005,** *11*, 6135-6144.

129. Gillies, E. R.; Dolain, C.; Léger, J.-M.; Huc, I. *J. Org. Chem.* **2006,** *71* (21), 7931-7939.

130. Qi, T.; Maurizot, V.; Noguchi, H.; Charoenraks, T.; Kauffmann, B.; Takafuji, M.; Ihara, H.; Huc, I. *Chem. Commun.* **2012,** *48* (51), 6337-6339.

131. Delsuc, N.; Godde, F.; Kauffmann, B.; Léger, J.-M.; Huc, I. *J. Am. Chem. Soc.* **2007,** *129* (37), 11348-11349.

132. Miller, N. C.; Grimm, H. M.; Horne, W. S.; Hutchison, G. R. *Nanoscale Adv.* **2019**. Just accepted.

133. Kim, S.; Seol, D.; Lu, X.; Alexe, M.; Kim, Y. *Scientific Reports* **2017,** *7*, 41657.

134. Katsouras, I.; Asadi, K.; Li, M.; van Driel, T. B.; Kjær, K. S.; Zhao, D.; Lenz, T.; Gu, Y.; Blom, P. W. M.; Damjanovic, D.; Nielsen, M. M.; de Leeuw, D. M. *Nature Materials* **2015,** *15*, 78.

135. Liu, S.; Cohen, R. E. *Phys. Rev. Lett.* **2017,** *119* (20), 207601.

136. Peet, N. P.; Baugh, L. E.; Sunder, S.; Lewis, J. E. *J. Med. Chem.* **1985,** *28*, 298-302.

137. Frisch, M. J.; Trucks, G. W.; Schlegel, H. B.; Scuseria, G. E.; Robb, M. A.; Cheeseman, J. R.; Scalmani, G.; Barone, V.; Mennucci, B.; Petersson, G. A. Gaussian 09, Revision A.02, Gaussian, Inc. Wallingford, CT, USA, **2009.**

138. Chai, J.-D.; Head-Gordon, M. *PCCP* **2008,** *10* (44), 6615-6620.

139. Schrodinger, LLC, The PyMOL Molecular Graphics System, Version 1.8. **2015**.

140. Hickey, A. L.; Rowley, C. N. *J. Phys. Chem. A* **2014,** *118* (20), 3678-3687.

141. Marvin, C. W.; Grimm, H. M.; Miller, N. C.; Horne, W. S.; Hutchison, G. R. *J. Phys. Chem. B* **2017,** *121* (44), 10269-10275.

142. Jaworek, T.; Neher, D.; Wegner, G.; Wieringa, R. H.; Schouten, A. J.. *Science* **1998,** *279* (5347), 57.

143. Prime, K. L.; Whitesides, G. M. *Science* **1991,** *252*, 1164+.

144. Furst, A. L.; Hill, M. G.; Barton, J. K. *Langmuir* **2013,** *29* (52), 16141-16149.

145. Devaraj, N. K.; Miller, G. P.; Ebina, W.; Kakaradov, B.; Collman, J. P.; Kool, E. T.; Chidsey, C. E. D. *J. Am. Chem. Soc.* **2005,** *127* (24), 8600-8601.

146. Gouget-Laemmel, A. C.; Yang, J.; Lodhi, M. A.; Siriwardena, A.; Aureau, D.; Boukherroub, R.; Chazalviel, J. N.; Ozanam, F.; Szunerits, S. *J. Phys. Chem. C* **2013,** *117* (1), 368-375.

147. Chelmowski, R.; Käfer, D.; Köster, S. D.; Klasen, T.; Winkler, T.; Terfort, A.; Metzler-Nolte, N.; Wöll, C. *Langmuir* **2009,** *25* (19), 11480-11485.

148. Collman, J. P.; Devaraj, N. K.; Chidsey, C. E. D. *Langmuir* **2004,** *20* (4), 1051-1053.

149. Collman, J. P.; Devaraj, N. K.; Eberspacher, T. P. A.; Chidsey, C. E. D. *Langmuir* **2006,** *22* (6), 2457-2464.

150. Nasrallah, H.; Rabah, J.; Bui-Thi-Tuyet, V.; Baczko, K.; Fensterbank, H.; Bourdreux, F.; Goncalves, A.-M.; Declerck, V.; Boujday, S.; Humblot, V.; Wright, K.; Vallée, A.; Allard, E. *New J. Chem.* **2018,** *42* (24), 19423-19432.

151. Hudalla, G. A.; Murphy, W. L. *Langmuir* **2009,** *25* (10), 5737-5746.

152. Guo, J.; Xie, Z.; Tran, R. T.; Xie, D.; Jin, D.; Bai, X.; Yang, J. *Adv. Mater.* **2014,** *26* (12), 1906-1911.

153. Shakiba, A.; Jamison, A. C.; Lee, T. R. *Langmuir* **2015,** *31* (22), 6154-6163.

154. Gallardo, I. F.; Webb, L. J. *Langmuir* **2012,** *28* (7), 3510-3515.

155. Raigoza, A. F.; Onyirioha, K.; Webb, L. J. *Applied Surface Science* **2017,** *396*, 1831-1839.

156. Leo, N.; Liu, J.; Archbold, I.; Tang, Y.; Zeng, X. *Langmuir* **2017,** *33* (8), 2050-2058.

157. Prime, K. L.; Whitesides, G. M. *J. Am. Chem. Soc.* **1993,** *115* (23), 10714-10721.

158. Friedel, M.; Baumketner, A.; Shea, J.-E. *Proc. Natl. Acad. Sci.* **2006,** *103* (22), 8396.

159. Ostuni, E.; Grzybowski, B. A.; Mrksich, M.; Roberts, C. S.; Whitesides, G. M. *Langmuir* **2003,** *19* (5), 1861-1872.

160. Stranick, S. J.; Parikh, A. N.; Tao, Y. T.; Allara, D. L.; Weiss, P. S. *J. Phys. Chem.* **1994,** *98* (31), 7636-7646.

161. Bertilsson, L.; Liedberg, B. *Langmuir* **1993,** *9* (1), 141-149.

162. Bain, C. D.; Whitesides, G. M. *Science* **1988,** *240* (4848), 62.

163. Siepmann, J. I.; McDonald, I. R. *Molecular Physics* **1992,** *75* (2), 255-259.

164. Marqusee, S.; Robbins, V. H.; Baldwin, R. L. *Proc. Natl. Acad. Sci.* **1989,** *86* (14), 5286.

165.   Schweitzer-Stenner, R.; Pecht, I.; Guo, C. *J. Phys. Chem. B* **2019,** *123* (4), 860-868.

166.   Kennedy, D. F.; Crisma, M.; Toniolo, C.; Chapman, D. *Biochemistry* **1991,** *30* (26), 6541-6548.

167.   Henchey, L. K.; Jochim, A. L.; Arora, P. S. *Curr. Op. Chem. Biol.* **2008,** *12* (6), 692-697.

168.Shea, E. K.; Rutkowski, R.; Kim, P. S., Evidence that the leucine zipper is a coiled coil. *Science* **1989,** *243* (4890), 538.

169.   Shea, E. K.; Klemm, J. D.; Kim, P. S.; Alber, T. *Science* **1991,** *254* (5031), 539.

170.   Oshaben, K. M.; Salari, R.; McCaslin, D. R.; Chong, L. T.; Horne, W. S. *Biochemistry* **2012,** *51* (47), 9581-9591.

171.   Nishihara, T.; Kitada, H.; Fujiwara, D.; Fujii, I. *Peptide Science* **2016,** *106* (4), 415-421.

172.   Baek, S.-J.; Park, A.; Ahn, Y.-J.; Choo, J. *Analyst* **2015,** *140* (1), 250-257.

173.   Abramyan, T.; Collier, G.; Kucukkal, T. G.; Li, X.; Snyder, J. A.; Thyparambil, A. A.; Vellore, N. A.; Wei, Y.; Yancey, J. A.; Stuart, S. J.; Latour, R. A. In *Proteins at Interfaces III State of the Art*, American Chemical Society: **2012**; Vol. 1120, pp 197-228.

174.   Witherow, D. S. *Biochem. Molec. Biol. Ed.* **2016,** *44* (6), 555-564.

175.   Stec, B.; Holtz, K. M.; Kantrowitz, E. R. *J. Molec. Biol.* **2000,** *299* (5), 1303-1311.

176.   Millán, J. L. *Purinergic Signal* **2006,** *2* (2), 335-341.

177.   Zhang, Z. Y.; VanEtten, R. L. *J. Biol. Chem.* **1991,** *266* (3), 1516-1525.

178.   Wu, J.; Zhao, C.; Lin, W.; Hu, R.; Wang, Q.; Chen, H.; Li, L.; Chen, S.; Zheng, J. *J. Mater. Chem. B* **2014,** *2* (20), 2983-2992.

179.   Hamada, H.; Arakawa, T.; Shiraki, K. *Current Pharmaceutical Biotechnology* **2009,** *10* (4), 400-407.

180.   Jeyachandran, Y. L.; Mielczarski, J. A.; Mielczarski, E.; Rai, B. *J. Colloid and Interface Science* **2010,** *341* (1), 136-142.

181.   Gill, S. C.; von Hippel, P. H. *Analytical Biochemistry* **1989,** *182* (2), 319-326.

182.   Oyelere, A. K.; Chen, P. C.; Huang, X.; El-Sayed, I. H.; El-Sayed, M. A. *Bioconjugate Chemistry* **2007,** *18* (5), 1490-1497.

183.   Alizadeh, A.; Khodaei, M. M.; Hamidi, Z.; Shamsuddin, M. B. *Sensors and Actuators B: Chemical* **2014,** *190* (Supplement C), 782-791.

184.   He, C.; Li, L.-W.; He, W.-D.; Jiang, W.-X.; Wu, C. *Macromolecules* **2011,** *44* (16), 6233-6236.

185.   Yang, J.; Ye, T.; Ma, D.; Zhang, Q. *Synthetic Metals* **2011,** *161* (3), 330-334.

186.   Dadová, J.; Vrábel, M.; Adámik, M.; Brázdová, M.; Pohl, R.; Fojta, M.; Hocek, M. *Chemistry – A European Journal* **2015,** *21* (45), 16091-16102.

187.   Lampinen, J., Raitio, M., Perala, A., Oranen, H., Harinen, R. R. *Application Note Retrived from Thermo Scientific: https://static.thermoscientific.com/images/D20827~.pdf* **2012**.